

UC San Diego

UC San Diego Electronic Theses and Dissertations

Title

Biomechanics of articular cartilage defects

Permalink

<https://escholarship.org/uc/item/4qj4v7jp>

Author

Gratz, Kenneth R.

Publication Date

2007

Peer reviewed|Thesis/dissertation

UNIVERSITY OF CALIFORNIA, SAN DIEGO

**BIOMECHANICS OF
ARTICULAR CARTILAGE DEFECTS**

A dissertation submitted in partial satisfaction of the
requirements for the degree Doctor of Philosophy

in

Bioengineering

by

Kenneth R. Gratz

Committee in charge:

Professor Robert L. Sah, Chair
Professor Wayne H. Akeson
Professor David Amiel
Professor Deidre A. MacKenna
Professor Andrew D. McCulloch

2007

Copyright

Kenneth R. Gratz, 2007

All rights reserved.

The dissertation of Kenneth R. Gratz is approved, and it is acceptable in quality and form for publication on microfilm:

Chair

University of California, San Diego

2007

TABLE OF CONTENTS

Signature Page	iii
Table of Contents.....	iv
List of Figures	ix
Acknowledgments.....	xii
Vita	xv
Abstract	xvii
Chapter 1: Introduction.....	1
1.1 General Introduction to the Dissertation	1
1.2 Cartilage Composition, Structure, and Function	3
1.3 Focal Defect Prevalence, Progression, and Intrinsic Repair	5
1.4 Mechanical Effects of Focal Defects.....	6
1.5 Articular Cartilage Repair and Integration	7
1.7 References	9

Chapter 2: The Effects of Focal Articular Defects on Intra-tissue Strains in the Surrounding and Opposing Cartilage 13

2.1 Abstract.....	13
2.2 Introduction	15
2.3 Materials and Methods	18
2.4 Results	32
2.5 Discussion.....	42
2.6 Acknowledgments	48
2.7 References	49

Chapter 3: Experimental Measurement and Quantification of Frictional Contact between Biological Surfaces Experiencing Large Deformation and Slip 53

3.1 Abstract.....	53
3.2 Introduction	55
3.3 Methods	58
3.4 Results	80
3.5 Discussion.....	84
3.6 List of Variables	86
3.7 Acknowledgments	87

3.8 References	89
Chapter 4: The Effects of Focal Articular Defects on Cartilage Contact Mechanics.....	92
4.1 Abstract.....	92
4.2 Introduction	94
4.3 Materials and Methods	97
4.4 Results	110
4.5 Discussion.....	122
4.6 Acknowledgments	128
4.7 References	129
Chapter 5: Biomechanical Assessment of Retrieved Tissue After In Vivo Cartilage Defect Repair: Tensile Modulus of Repair Tissue and Integration with Host Cartilage	133
5.1 Abstract.....	133
5.2 Introduction	135
5.3 Materials and Methods	138
5.4 Results	146
5.5 Discussion.....	150

5.6 Acknowledgments	155
5.7 References	156
Chapter 6: Conclusions.....	160
6.1 Summary and Significance of Findings	160
6.2 Discussion and Future Directions.....	164
6.4 References	181
Appendix A: Supplemental Material for Chapter 2	186
A.1 Introduction	186
A.2 Materials and Methods	187
A.3 Results	190
A.4 Acknowledgments	192
A.5 References	204
Appendix B: Supplemental Material for Chapter 4.....	205
B.1 Introduction.....	205
B.2 Materials and Methods	206
B.3 Results.....	210

B.6 Acknowledgments	212
B.7 References.....	219

LIST OF FIGURES

Figure 2.1: Sample preparation and micro-mechanical testing of opposing osteochondral blocks.	20
Figure 2.2: Locations of sub-regions used for statistical analysis of strain distributions in intact control and defect-containing samples.	23
Figure 2.3: Representative defect sample before and after loading, with superimposed strain maps.	33
Figure 2.4: Strain measurements at selected sub-regions in opposing cartilage surfaces.	35
Figure 2.5: Composite strain maps of contacting surfaces in defect samples.	37
Figure 2.6: Area and volume changes at selected sub-regions in opposing cartilage surfaces.	38
Figure 2.7: Adjusted relative lateral displacement (RLD) profiles and average normalized RLD.	40
Figure 2.8: Summary of the effects of defects on cartilage mechanics.	41
Figure 3.1: Diagram of contact definitions in 2 and 3 dimensions.	63
Figure 3.2: Diagram of the theoretical dataset used for validation of 3-D contact definitions.	70
Figure 3.3: Sample preparation and mechanical testing setup of opposing cartilage blocks.	72
Figure 3.4: Flowchart of image processing routine.	77
Figure 3.5: Deformation and sliding between cartilage surfaces with matched (PFG-PFG) or mismatched (PFG-UTP) mechanical properties.	83
Figure 4.1: Sample preparation and micro-mechanical testing of opposing osteochondral blocks.	100
Figure 4.2: Locations of sub-regions used for statistical analysis of strain distributions.	102

Figure 4.3: Representative images depicting the time-course of axial strain development in intact samples.....	112
Figure 4.4: Strain measurements at selected sub-regions of samples.	114
Figure 4.5: Representative images depicting the time-course of axial strain development in defect-containing samples.	115
Figure 4.6: Composite principal strain maps in bovine samples directly following loading or after stress relaxation.	116
Figure 4.7: Area and volume changes at selected sub-regions in bovine samples directly following loading or after stress relaxation.....	118
Figure 4.8: Sliding distance profiles over surfaces of open defect and closed defect samples compared to the average sliding over intact surfaces at several levels of applied compression.	120
Figure 4.9: Average normalized sliding distance over intact, closed defect, and open defect samples.	121
Figure 4.10: Summary of the effects of defects on cartilage mechanics.....	123
Figure 5.1: Diagram of harvest locations and specimen geometry.	139
Figure 5.2: Sequential images of representative intact control and integration samples during tensile testing.	141
Figure 5.3: Correlation analysis of digital strain images.....	144
Figure 5.4: Properties of intact control and integration samples.....	147
Figure 5.5: Analysis of strain distribution and tensile moduli for intact control and integration samples.....	148
Figure 6.1: Potential size thresholds of defect mechanical behavior.	174
Figure 6.2: Hypothesized mechanisms of defect progression.	180
Figure A.1: Strain measurements at selected sub-regions in bovine samples.....	193
Figure A.2: Composite strain maps of bovine and human defect samples.	194
Figure A.3: Principal strain measurements at selected sub-regions in bovine and human samples.	195
Figure A.4: Composite principal strain maps of bovine and human defect samples.	196

Figure A.5: Area and volume changes at selected sub-regions in bovine and human samples.	197
Figure A.6: Composite maps of area and volume changes in bovine and human defect samples.	198
Figure A.7: Schematic of the sliding calculations.....	199
Figure A.8: Relative lateral displacement (RLD) between contacting human cartilage surfaces.	200
Figure A.9: Normalized Relative Lateral Displacements (RLD) between contacting human intact cartilage surfaces or cartilage surfaces adjacent to focal defects.....	201
Figure A.10: Relative lateral displacement (RLD) between contacting bovine cartilage surfaces.	202
Figure A.11: Normalized Relative Lateral Displacements (RLD) between contacting bovine intact cartilage surfaces or cartilage surfaces adjacent to focal defects.....	203
Figure B.1: Schematic of the sliding calculations.....	213
Figure B.2: Sliding distances of surfaces adjacent to defects with open or closed orientations compared to the sliding between intact controls.	214
Figure B.3: Normalized sliding distance between contacting intact cartilage surfaces, or cartilage surfaces adjacent to focal defects with.....	215
Figure B.6: Principal strain measurements at selected sub-regions in bovine samples directly following loading or after stress relaxation.....	216
Figure B.7: Composite principal strain maps in bovine samples directly following loading or after stress relaxation.	217
Figure B.8: Composite maps of area and volume changes in bovine samples directly following loading or after stress relaxation.	218

ACKNOWLEDGMENTS

I owe thanks to many people for their help and support during my time in the UCSD graduate program. First, I would like to thank my advisor, Dr. Robert Sah, for allowing me to join his lab and teaching me a great deal about how to conduct quality research. I would also like to thank the numerous contributors to the studies comprising the chapters of this dissertation.

Chapter 2 was submitted, in full, for publication in *Biorheology*. The dissertation author is the primary investigator and thanks co-authors Ben Wong and Drs. Won Bae, and Robert Sah. I would further like to acknowledge Drs. William Bugbee, Martin Lotz, and Richard Coutts for supplying human tissue samples. This work was supported in part by the National Institutes of Health and the National Science Foundation, and by a grant to the University of California, San Diego, in support of Dr. Robert Sah, from the Howard Hughes Medical Institute through the HHMI Professors Program.

Chapter 3 has been submitted, in part, for publication in *Journal of Biomechanics*. The dissertation author is the primary investigator and thanks co-author Dr. Robert Sah. This work was supported in part by the National Institutes of Health and the National Science Foundation, and by a grant to the University of California, San Diego, in support of Dr. Robert Sah, from the Howard Hughes Medical Institute through the HHMI Professors Program.

Chapter 4 will be submitted, in part, for publication in the *Journal of Orthopaedic Research*. The dissertation author is the primary investigator and would like to thank co-authors Ben Wong and Drs. Won Bae and Robert Sah for their contributions to this chapter. This work was supported in part by the National Institutes of Health and the National Science Foundation, and by a grant to the University of California, San Diego, in support of Dr. Robert Sah, from the Howard Hughes Medical Institute through the HHMI Professors Program.

Chapter 5 is reprinted, in full, in the *Journal of Biomechanics*, volume 39, issue 1, January 2006 with permission from Elsevier. The dissertation author is the primary investigator and thanks co-authors Van Wong and Drs. Albert Chen, Lisa Fortier, Alan Nixon, and Robert Sah. Additionally, I would like to thank my collaborators Drs. Lisa Fortier and Alan Nixon, who provided valuable samples from their previously-published *in vivo* study. This work was supported by the Arthritis Foundation, Harry M Zweig Foundation, Institute for Sports Medicine Research, NASA, NIH, NSF, and the Office for Naval Research (NDSEG Fellowship to KRG).

I would also like to thank my thesis committee: Drs. David Amiel, Wayne Akeson, Deidre MacKenna, and Andrew McCulloch, for providing sound critiques and advice on my proposed research. Their time spent preparing and participating in this process is greatly appreciated.

Additionally, I would like to thank the other members, past and present, of the CTE lab: Barb Schumacher, Albert Chen, and Michael Voegtline, staff members who taught me a great deal during my time in the lab; Van Wong, now the lab manager, who has seen his role and responsibilities in the lab grow significantly in my time at

UCSD, but has maintained his willingness to help out with any problem; the old guard of graduate students: Won Bae, Michele Temple, Travis Klein, Tannin Schmidt, and Kyle Jadin who helped me learn the ropes in the lab; the other members of my incoming class, Gayle Nugent and Anya Asanbaeva, who entered the lab with me and were always a good source of advice and support; and finally the “kids” in the lab, Megan Blewis, Greg Williams, Nancy Hsieh, Ben Wong, Jen Hwang, and Jen Antonacci - it is clear that the future of the lab is in good hands.

Finally, I would like to thank my good friends Katie Medders, Ben Sullivan, Tom DiCicco, Tannin Schmidt, Greg Williams, Megan Blewis, and Gayle Nugent who made my time in San Diego so enjoyable. I wish them all the best in their own academic and career pursuits. I respect them all enormously as scientists and engineers, but even more as people. I am lucky to have known and worked with such a great group of people.

I would especially like to thank my girlfriend, Jennie Reed, for her support and patience during this long process. She is a great person and a great friend. She was always there for me when I needed her.

Finally, I would like to thank my parents, David and Linda. They have always been my biggest supporters and have contributed significantly to any success that I’ve experienced.

VITA

- 2001 B.S., Aerospace Engineering
Syracuse University, Syracuse, New York
- 2002-2007 Graduate Student Researcher
Cartilage Tissue Engineering Laboratory
University of California, San Diego, La Jolla, California
- 2003 M.S., Bioengineering
University of California, San Diego, La Jolla, California
- 2007 Ph.D., Bioengineering
University of California, San Diego, La Jolla, California

Book Chapter

Chen AC, Klisch SM, Bae WC, Temple MM, McGowan KB, Gratz KR, Schumacher BL, Sah RL: Mechanical characterization of native and tissue-engineered cartilage. In: *Methods in Molecular Medicine: Osteoarthritis: Methods and Protocols*, ed. by M Sabatini, DeCeuninck F, Pastoureau P, Humana Press, Totowa, NJ, 2004, pp 157-90.

Journal Articles

Gratz KR, Wong VW, Chen AC, Fortier LA, Nixon AJ, Sah RL: Biomechanical assessment of tissue retrieved after in vivo cartilage defect repair: tensile modulus of repair tissue and integration with host cartilage. *J Biomech* 39:138-46, 2006.

Selected Abstracts

Gratz KR, Wong BL, Bae WC, Sah RL: Focal Articular Defects Alter Cartilage Contact Mechanics. *5th International Symposium on Mechanobiology of Cartilage and Chondrocyte, Athens GR, 2007*

Williams GM, Gratz KR, Sah RL: Asymmetrical strain distribution and neutral axis location in cartilage subjected to bending. *5th International Symposium on Mechanobiology of Cartilage and Chondrocyte, Athens GR, 2007*

Wong BL, Bae WC, Chun J, Gratz KR, Sah RL: Micro-mechanics of cartilage articulation: effect of degeneration on shear deformation. *Trans Orthop Res Soc* 32:100, 2007.

Gratz KR, Wong BL, Bae WC, Sah RL: Effects of a focal articular defect on cartilage contact mechanics. *Trans Orthop Res Soc* 32:617, 2007.

Gratz KR, Wong BL, Bae WC, Sah RL: Focal articular defects modify cartilage contact mechanics. *Proc 25th SPRBM Conf*, in *MCB* 3:199-200, 2006.

Wong BL, Bae WC, Chun J, Gratz KR, Sah RL: Lubricating effect of synovial fluid on cartilage biomechanics during articulation. *BMES*, 2006.

Gratz KR, Wong VW, Chen AC, Goodrich LR, Hidaka C, Fortier LA, Nixon AJ, Sah RL: Integration of repair and host cartilage in vivo: effect of insulin-like growth factor I. *Trans Orthop Res Soc* 29:662, 2004.

Gratz KR and Davidson BD: A Combined Tension-Bending Test for Assessing Mixed-Mode Delamination Growth Predictions. *Proc. 42nd AIAA/ASME/ASCE /AHS/ASC Structures, Structural Dynamics and Materials Conf.* AIAA Paper No. 2001-1448, 2001.

ABSTRACT OF THE DISSERTATION

BIOMECHANICS OF ARTICULAR CARTILAGE DEFECTS

by

Kenneth R. Gratz

Doctor of Philosophy in Bioengineering

University of California, San Diego, 2007

Professor Robert L. Sah, Chair

Articular cartilage is the load-bearing connective tissue that covers the ends of long-bones in diarthroidal joints and provides low friction, wear resistant sliding during joint articulation. Cartilage has complex mechanical and surface properties that greatly complicate the biomechanics of contact between opposing cartilage surfaces. Focal damage to articular cartilage is common, and once initiated, shows limited capacity for repair. Furthermore, changes in the mechanical environment at a site of damage may make the tissue more susceptible to continued degeneration. The goal of this dissertation work was to contribute to the understanding of changes in the mechanical

environment due to focal articular defects and to quantify the extent to which normal mechanical properties are restored following *in vivo* cartilage defect repair.

Experimental methods were developed to allow *in vitro* mechanical testing of two contacting cartilage surfaces while tissue deformation was imaged; image analysis methods were introduced to automatically track fiducial markers within the tissue, and a mathematical framework was developed to describe the dynamic deformation and sliding between opposing surfaces from the movement of these discrete tissue markers.

In vitro experiments on both bovine and human cartilage showed elevated axial compressive strains in the cartilage adjacent to a defect and sharp increases in shear and lateral strains in the region opposing the defect rim. Changes in intra-tissue strains arose early during compressive loading and were maintained following stress relaxation in the loaded state. Increased sliding was also observed between surfaces near a focal defect and was related to characteristics of the defect edge.

Assessment of samples retrieved following *in vivo* defect repair showed that currently available cell-based therapies may result in greater integration strength than has previously been reported ($\sim 1/2$ normal tensile strength), but that the tensile modulus of the repair tissue remains orders of magnitude lower than that of normal articular cartilage after 9 months *in vivo*.

Understanding the changes in mechanical environment near a focal defect that are likely to lead to continued degeneration, and the ability for repair strategies to restore normal biomechanical tissue function, may help to guide treatments to arrest or reverse the degenerative process.

CHAPTER 1

INTRODUCTION

1.1 General Introduction to the Dissertation

Injured cartilage has a low capacity for repair and sites of damage may initiate continued degeneration of the tissue. Alterations to the mechanical environment in the vicinity of a focal defect have been proposed as a likely contributor to progressive tissue degradation by altering the cellular response to loading, causing acute damage to cells or matrix, or accelerating the fatigue and wear of the tissue. Previous studies investigated changes in contact pressures near focal defects and did not identify specific mechanical alterations likely to account for the deleterious consequences of defects. However, other studies have observed deformation of tissue near a defect, suggesting that large strains may occur locally and be responsible for continued tissue damage. Quantification of the effects of articular defects on adjacent and opposing cartilage deformations could provide insights into the possible source of adverse consequences. Characterization of the restoration of biomechanical properties at a defect and its interface with native cartilage following defect repair may indicate potential limitations to current therapies and identify targets for improvement.

The goal of this dissertation work was to contribute to the understanding of changes in the mechanical environment due to focal articular defects and the extent to which normal mechanical properties are restored *in vivo* using one current method cartilage defect repair. To achieve these goals, the effects of focal defect presence on cartilage contact mechanics (i.e. intra-tissue strain and induced sliding) were investigated in an *in vitro* model, and quantitative mechanical measures of repair were performed on retrieved *in vivo* samples.

Chapter 2, which was submitted to *Biorheology*, describes the deformation of opposing cartilage surfaces following loading in uniaxial compression. The study quantified the intra-tissue strain distributions in opposing intact osteochondral surfaces and the changes in these strains resulting from the creation of a focal defect in one of the surfaces. The presence of such a defect may affect more than just the static levels of strain directly following loading. These defects may also alter the dynamic redistribution of strain during loading and relaxation and the incongruous surface could increase sliding between the contacting surfaces.

The need for dynamic analyses of contact motivated the work in Chapter 3, a detailed mathematical framework to quantify the biomechanics of contact (including large deformations and slips) from 2-D or 3-D experimental datasets. In conjunction with this formulation, the image processing methods of Chapter 2 were modified to dynamically track tissue deformations using an automated image correlation-based approach.

Chapter 4 implemented the experimental and analytical techniques developed in previous chapters to characterize the dynamic contact mechanics between intact or

defect-containing surfaces. Specifically, changes in the dynamic development of strain during loading and the redistribution of those strains during stress relaxation were quantified. Additionally, surface sliding induced at the defect edge was analyzed.

The extent of success of repairing a focal cartilage defect may be predicated at least in part, on the ability to restore the normal mechanical environment. This may include the bulk mechanical properties of the graft tissue as well as functional integration between the graft and surrounding host tissue. Chapter 5, which was published, in full, in the *Journal of Biomechanics*, investigates for the first time, the tensile properties of retrieved repair tissue resulting from cell transplantation and the tensile strength of integration of this tissue to the surrounding host cartilage. Knowledge of the properties resulting from *in vivo* repair procedures may allow the mechanical functionality of these procedures to be investigated in *in vitro* models, similar to those used in this dissertation.

Chapter 6 summarizes the major findings of the studies, discusses the implications of these finding, and explores the future directions of the work.

1.2 Cartilage Composition, Structure, and Function

Articular cartilage normally functions as a load-bearing, low-friction, wear-resistant material at the ends of long-bones. It consists of two components: a solid component, composed primarily of extracellular matrix (ECM) proteins with a sparse population of highly specialized cells (chondrocytes) and a fluid component that accounts for up to 80% of the tissue wet weight [10]. The majority of the solid

cartilage matrix is composed of two proteins, the large aggregating proteoglycan aggrecan and a fibrillar network of type II collagen.

Mature articular cartilage is inhomogeneous in both composition and structure, showing significant variation with tissue depth. The superficial zone of cartilage is more densely populated with chondrocytes, and the cells in this region have a flattened morphology [49] and specialized physiological functions (i.e. PRG4 secretion [47]). In the middle and deep zones, chondrocytes have a round morphology and are more sparsely distributed, with cells in the deep zone and arranging into columns [49]. Proteoglycan content is lowest in the superficial region and increases significantly with tissue depth [35]. Collagen content varies little throughout the tissue, but organization of collagen fibrils changes markedly with tissue depth: fibrils are oriented parallel to the articular surface in the superficial zone and transition through the middle zone, eventually assuming a radial orientation in the deeper layers [4].

Mechanical properties of cartilage also differ significantly in different tissue zones and are related to the compositional and structural variations. The significant decrease in permeability [34] and increase in compressive modulus [46] observed with tissue depth are correlated to the increased proteoglycan content in the deeper cartilage layers. On the other hand, the collagen network is responsible for the majority of the tensile and restraining properties of the tissue [10]. Cartilage tensile properties are dependent on both the content and organization of the collagen network. Tissue contents of both collagen and collagen crosslinks correlate with the biomechanical tensile properties of cartilage [28, 44]. During normal growth and

maturation, changes in these contents correlate with increases in tissue mechanical properties [52]. The dependence of cartilage mechanical properties on collagen network structure is demonstrated by the changes in tensile modulus and strength with fibril orientation [28, 44, 54] and the role of superficial fibrils in resisting compression by the so-called “trampoline effect” [16].

1.3 Focal Defect Prevalence, Progression, and Intrinsic Repair

Focal articular cartilage defects are prevalent in symptomatic knees. Previously undiagnosed chondral lesions were present in ~60% of patients, between the ages of 1 and 96 (average ~40 y.o.), undergoing arthroscopies for knee pain, with roughly a third of these being classified as focal cartilage defects. The likelihood of finding chondral damage increased with patient age, as did the severity of the damage encountered [14, 23]. However, advanced chondral defects were also common in younger patients: ~10% of patients ≤ 40 years old had at least one defect extending $\geq \frac{1}{2}$ the cartilage thickness [14, 23].

Recent studies suggest that an articular defect, if left untreated, will continue progress and initiate osteoarthritis. Clinical MRI studies have observed increases in focal defect size over a 2 yr period [51], and accelerated rates of cartilage volume loss in joints containing focal defects [11, 53]. Similar degenerative changes have been observed near cartilage defects created in *in vivo* animal models [25, 31], but interpretation of these models is complicated by the use of different animal models with distinct differences in joint size and loading and cartilage thickness and

mechanical properties. The eventual fate of a defect may be related to the defect size or loading environment, with defects that are smaller or in unloaded regions generally showing fewer signs of degeneration and better filling of the defect with repair tissue [12, 17, 25, 39]. Theoretical modeling of the repair process has predicted that cartilage thickness and defect depth will also greatly affect the quality of repair [17].

1.4 Mechanical Effects of Focal Defects

The mechanical environment surrounding a focal defect is significantly altered and may contribute to progressive cartilage degradation. Elevated peak and average contact stresses and stress gradients have been measured near, but not at, the edges of experimentally-created defects [9, 21] in *ex vivo* whole joint studies. The magnitudes of contact stress increases were affected by the size of the defects significantly affected and the presence, or absence, of the meniscus. Recruitment of new contact area in the radial direction helped to minimize changes in contact stress [9], but in doing so may create substantial local deformations and intra-tissue strains. A recent study confirmed the presence of large macroscopic deformations in the tissue surrounding and opposing focal defects [6], and finite element modeling predicts increased strains in the surround tissue [41].

Treatments to repair focal defects show variable abilities to restore the normal contact stress distributions. Fibrin glue, modeling an immature graft, is able to prevent elevations in contact stresses at the surfaces of adjacent cartilage [42], but it is unknown whether they effectively limit tissue deformation. Osteochondral grafts can

also prevent abnormal contact stresses, but care must be taken to properly align and position the graft in the defect [29, 30].

Similar mechanical effects were observed in the analogous situation of intra-articular step-offs [8, 37, 38]. Additionally, elevated contact stresses and contact stress gradients were shown to be maintained during dynamic physiological loading [37, 38]. It has been suggested that persistent regions of higher pressures may result in lower local fluid content and possibly lead to greater solid matrix damage [38].

1.5 Articular Cartilage Repair and Integration

It is commonly noted that damaged articular cartilage has a low potential for intrinsic repair [33]. This problem has motivated a great deal of research into methods of enhancing the repair response [45]. A variety of surgical techniques can be used to treat focal chondral defects, and usually involve removal of damaged tissue from the defect edge, followed by filling of the defect with cells, graft, or implant. Current treatments include microfracture, osteochondral autografts [1, 22] and allografts [3, 13, 18, 20], and cell implantation [7], each with their own advantages. The choice of treatment is often guided by the location and physical characteristics (including size) of the defect [32].

Each of these treatments results in interfaces between repair and native tissues where integration is desirable. However, integrative repair is not observed in experimentally created lacerations in the articular surfaces of mature cartilage [33], or between the surface of repair tissue and native cartilage following intrinsic repair of

full-thickness defects [48]. Often, the development of adhesive strength is used as a functional measure of integration. *In vitro* studies have identified several factors contributing to the development of adhesive strength, including the presence of viable cells [5, 43], the biosynthesis and transport of collagen to the interface [15], and the formation of lysyl-oxidase mediated collagen crosslinks [2]. Initial adhesion of cartilaginous surfaces has been accomplished by the initiation of cross-linking through photochemical welding [26], fibrin glue [27], or transglutaminase treatments [27], while other treatments, such as selective enzymatic degradation of cartilage matrix components [5, 24, 40, 50], or pretreatment with the lathyrogen BAPN [36], have been shown to increase or accelerate, respectively, the development of adhesive strength *in vitro*. However, even with the current treatments, values of adhesive strength fall significantly below the strength of normal cartilage, and this lack of integrative repair may eventually lead to degeneration [19, 48].

1.7 References

1. Ahmad CS, Guiney WB, Drinkwater CJ: Evaluation of donor site intrinsic healing response in autologous osteochondral grafting of the knee. *Arthroscopy* 18:95-8, 2002.
2. Ahsan T, Lottman LM, Harwood FL, Amiel D, Sah RL: Integrative cartilage repair: inhibition by beta-aminopropionitrile. *J Orthop Res* 17:850-7, 1999.
3. Alford JW, Cole BJ: Cartilage restoration, part 2: techniques, outcomes, and future directions. *Am J Sports Med* 33:443-60, 2005.
4. Benninghoff A: Form und bau der gelenkknorpel in ihren beziehungen zur funktion. Zweiter teil: der aufbau des gelenkknorpels in seinen beziehungen zur funktion. *Z Zellforsch* 2:783-862, 1925.
5. Bos PK, DeGroot J, Budde M, Verhaar JA, van Osch GJ: Specific enzymatic treatment of bovine and human articular cartilage: implications for integrative cartilage repair. *Arthritis Rheum* 46:976-85, 2002.
6. Braman JP, Bruckner JD, Clark JM, Norman AG, Chansky HA: Articular cartilage adjacent to experimental defects is subject to atypical strains. *Clin Orthop Relat Res* 430:202-7, 2005.
7. Brittberg M, Lindahl A, Nilsson A, Ohlsson C, Isaksson O, Peterson L: Treatment of deep cartilage defects in the knee with autologous chondrocyte transplantation. *N Engl J Med* 331:889-95, 1994.
8. Brown TD, Anderson DD, Nepola JV, Singerman RJ, Pedersen DR, Brand RA: Contact stress aberrations following imprecise reduction of simple tibial plateau fractures. *J Orthop Res* 6:851-62, 1988.
9. Brown TD, Pope DF, Hale JE, Buckwalter JA, Brand RA: Effects of osteochondral defect size on cartilage contact stress. *J Orthop Res* 9:559-67, 1991.
10. Buckwalter JA, Mankin HJ: Articular cartilage. Part I: tissue design and chondrocyte-matrix interactions. *J Bone Joint Surg Am* 79-A:600-11, 1997.
11. Cicuttini F, Ding C, Wluka A, Davis S, Ebeling PR, Jones G: Association of cartilage defects with loss of knee cartilage in healthy, middle-age adults: a prospective study. *Arthritis Rheum* 52:2033-9, 2005.
12. Convery FR, Akeson WH, Keown GH: The repair of large osteochondral defects. An experimental study in horses. *Clin Orthop Rel Res* 82:253-62, 1972.
13. Convery FR, Akeson WH, Meyers MA: The operative technique of fresh osteochondral allografting of the knee. *Oper Techn Orthop* 7:340-4, 1997.
14. Curl WW, Krome J, Gordon ES, Rushing J, Smith BP, Poehling GG: Cartilage injuries: a review of 31,516 knee arthroscopies. *Arthroscopy* 13:456-60, 1997.

15. DiMicco MA, Sah RL: Integrative cartilage repair: adhesive strength correlates with collagen deposition. *J Orthop Res* 19:1105-12, 2001.
16. Donzelli PS, Spilker RL, Ateshian GA, Mow VC: Contact analysis of biphasic transversely isotropic cartilage layers and correlations with tissue failure. *J Biomech* 32:1037-47, 1999.
17. Duda GN, Maldonado ZM, Klein P, Heller MO, Burns J, Bail H: On the influence of mechanical conditions in osteochondral defect healing. *J Biomech* 38:843-51, 2005.
18. Garrett JC: Osteochondral allografts for reconstruction of articular defects of the knee. *Instr Course Lect* 47:517-22, 1998.
19. Ghadially FN, Thomas I, Oryschak AF, LaLonde J-MA: Long term results of superficial defects in articular cartilage. A scanning electron microscope study. *J Pathol* 121:213-7, 1977.
20. Ghazavi MT, Pritzker KP, Davis AM, Gross AE: Fresh osteochondral allografts for post-traumatic osteochondral defects of the knee. *J Bone Joint Surg Br* 79-B:1008-13, 1997.
21. Guettler JH, Demetropoulos CK, Yang KH, Jurist KA: Osteochondral defects in the human knee: influence of defect size on cartilage rim stress and load redistribution to surrounding cartilage. *Am J Sports Med* 32:1451-8, 2004.
22. Hangody L, Rathonyi GK, Z D, Vasarhelyi G, Fules P, Modis L: Autologous osteochondral mosaicplasty. *J Bone Joint Surg* 86-A, Supplement 1:65-72, 2004.
23. Hjelle K, Solheim E, Strand T, Muri R, Brittberg M: Articular cartilage defects in 1,000 knee arthroscopies. *Arthroscopy* 18:730-4, 2002.
24. Hunziker EB, Rosenberg LC: Repair of partial-thickness defects in articular cartilage: Cell recruitment from the synovial membrane. *J Bone Joint Surg Am* 78-A:721-33, 1996.
25. Jackson DW, Lalor PA, Aberman HM, Simon TM: Spontaneous repair of full-thickness defects of articular cartilage in a goat model. A preliminary study. *J Bone Joint Surg Am* 83-A:53-64, 2001.
26. Jackson RW, Judy MM, Matthews JL, Nosir H: Photochemical tissue welding with 1,8 naphthalimide dyes: in vivo meniscal and cartilage welds. *Trans Orthop Res Soc* 22:650, 1997.
27. Jürgensen K, Aeschlimann D, Cavin V, Genge M, Hunziker EB: A new biological glue for cartilage-cartilage interfaces: tissue transglutaminase. *J Bone Joint Surg Am* 79-A:185-93, 1997.

28. Kempson GE, Muir H, Pollard C, Tuke M: The tensile properties of the cartilage of human femoral condyles related to the content of collagen and glycosaminoglycans. *Biochim Biophys Acta* 297:456-72, 1973.
29. Koh JL, Kowalski A, Lautenschlager E: The effect of angled osteochondral grafting on contact pressure: a biomechanical study. *Am J Sports Med* 34:116-9, 2006.
30. Koh JL, Wirsing K, Lautenschlager E, Zhang LO: The effect of graft height mismatch on contact pressure following osteochondral grafting. A biomechanical study. *Am J Sports Med* 32:317-20, 2004.
31. Lefkoe TP, Trafton PG, Ehrlich MG, Walsh WR, Dennehy DT, Barrach HJ, Akelman E: An experimental model of femoral condylar defect leading to osteoarthritis. *J Orthop Trauma* 7:458-67, 1993.
32. Mandelbaum BR, Browne JE, Fu F, Micheli L, Mosely JB, Jr., Erggelet C, Minas T, Peterson L: Articular cartilage lesions of the knee. *Am J Sports Med* 26:853-61, 1998.
33. Mankin HJ: The response of articular cartilage to mechanical injury. *J Bone Joint Surg Am* 64-A:460-6, 1982.
34. Maroudas A: Physicochemical properties of cartilage in the light of ion exchange theory. *Biophys J* 8:575-95, 1968.
35. Maroudas A, Venn M: Chemical composition and swelling of normal and osteoarthrotic femoral head cartilage. II. Swelling. *Ann Rheum Dis* 36:399-406, 1977.
36. McGowan KB, Sah RL: Treatment of cartilage with beta-aminopropionitrile accelerates subsequent collagen maturation and modulates integrative repair. *J Orthop Res* 23:594-601, 2005.
37. McKinley TO, McKinley T, Rudert MJ, Koos DC, Pedersen DR, Baer TE, Tochigi Y, Brown TD: Stance-phase aggregate contact stress and contact stress gradient changes resulting from articular surface stepoffs in human cadaveric ankles. *Osteoarthritis Cartilage*, 2005.
38. McKinley TO, Rudert MJ, Koos DC, Pedersen DR, Baer TE, Tochigi Y, Brown TD: Contact stress transients during functional loading of ankle stepoff incongruities. *J Biomech*, 2005.
39. Nelson BH, Anderson DD, Brand RA, Brown TD: Effect of osteochondral defects on articular cartilage. Contact pressures studied in dog knees. *Acta Orthop Scand* 56:547, 1988.
40. Obradovic B, Martin I, Padera RF, Treppo S, Freed LE, Vunjak-Novakovic G: Integration of engineered cartilage. *J Orthop Res* 19:1089-97, 2001.
41. Pena E, Calvo B, Martinez MA, Doblare M: Effect of the size and location of osteochondral defects in degenerative arthritis. A finite element simulation. *Comput Biol Med* 37:376-87, 2007.

42. Raimondi MT, Pietrabissa R: Contact pressures at grafted cartilage lesions in the knee. *Knee Surg Sports Traumatol Arthrosc* 13:444-50, 2005.
43. Reindel ES, Ayroso AM, Chen AC, Chun DM, Schinagl RM, Sah RL: Integrative repair of articular cartilage *in vitro*: adhesive strength of the interface region. *J Orthop Res* 13:751-60, 1995.
44. Roth V, Mow VC: The intrinsic tensile behavior of the matrix of bovine articular cartilage and its variation with age. *J Bone Joint Surg Am* 62-A:1102-17, 1980.
45. Sah RL: Interface and bulk regions in the repair, regeneration, and replacement of articular cartilage. *J Musculoskelet Neuronal Interact* 4:393-5, 2004.
46. Schinagl RM, Gurskis D, Chen AC, Sah RL: Depth-dependent confined compression modulus of full-thickness bovine articular cartilage. *J Orthop Res* 15:499-506, 1997.
47. Schumacher BL, Block JA, Schmid TM, Aydelotte MB, Kuettner KE: A novel proteoglycan synthesized and secreted by chondrocytes of the superficial zone of articular cartilage. *Arch Biochem Biophys* 311:144-52, 1994.
48. Shapiro F, Koido S, Glimcher MJ: Cell origin and differentiation in the repair of full-thickness defects of articular cartilage. *J Bone Joint Surg Am* 75-A:532-53, 1993.
49. Stockwell RA, Meachim G: The chondrocytes. In: *Adult Articular Cartilage*, ed. by MAR Freeman, Pitman Medical, Tunbridge Wells, England, 1979, 69-144.
50. van de Breevaart Bravenboer J, In der Maur CD, Bos PK, Feenstra L, Verhaar JA, Weinans H, van Osch GJ: Improved cartilage integration and interfacial strength after enzymatic treatment in a cartilage transplantation model. *Arthritis Res Ther* 6:R469-76, 2004.
51. Wang Y, Ding C, Wluka AE, Davis S, Ebeling PR, Jones G, Cicuttini FM: Factors affecting progression of knee cartilage defects in normal subjects over 2 years. *Rheumatology (Oxford)* 45:79-84, 2006.
52. Williamson AK, Chen AC, Masuda K, Thonar EJ-MA, Sah RL: Tensile mechanical properties of bovine articular cartilage: variations with growth and relationships to collagen network components. *J Orthop Res* 21:872-80, 2003.
53. Wluka AE, Ding C, Jones G, Cicuttini FM: The clinical correlates of articular cartilage defects in symptomatic knee osteoarthritis: a prospective study. *Rheumatology (Oxford)* 44:1311-6, 2005.
54. Woo SL-Y, Akeson WH, Jemmott GF: Measurements of nonhomogeneous directional mechanical properties of articular cartilage in tension. *J Biomech* 9:785-91, 1976.

CHAPTER 2

THE EFFECTS OF FOCAL ARTICULAR DEFECTS ON INTRA-TISSUE STRAINS IN THE SURROUNDING AND OPPOSING CARTILAGE

2.1 Abstract

Focal damage to articular cartilage is found commonly in arthroscopy patients and the alteration of the mechanical environment of the chondrocytes may contribute to progressive degeneration of the cartilage. The objective of this study was to quantify changes in intra-tissue strain occurring in cartilage near and opposing a focal defect. Pairs of osteochondral blocks from the femoral condyles of adult human knees were compressed uniaxially by 20% of the total cartilage thicknesses, and the state of tissue deformation before and after compression was recorded by video microscopy. A single, full-thickness chondral defect was created in one block from each pair. Blocks were then allowed to re-swell for >1 hr and retested. Stained nuclei, acting as fiducial markers, were tracked by digital image correlation and used to calculate cartilage strains and relative surface displacement due to loading. Intact blocks displayed axial strains that increased with depth and relatively little sliding. In tests of samples with a

defect, strain magnitudes were elevated in cartilage adjacent to, and opposing, the defect, and sliding between surfaces was also increased. Localized alterations in strain may contribute to altered chondrocyte metabolism, chondrocyte death, matrix damage, or accelerated wear *in vivo*, and the efficacy of repair strategies may depend on the ability to alleviate adverse mechanical conditions.

2.2 Introduction

Focal defects in articular cartilage are commonly found in symptomatic knees [10, 20]. Previously undiagnosed chondral defects extending at least half the cartilage thickness have been documented in ~10% of patients ≤ 40 years old undergoing arthroscopies, with even greater frequency with advancing age [10, 20]. The presence of such defects may contribute to the progressive degeneration of the joint [8, 43, 47]. Untreated focal defects increase in size over time [43], and defect-containing joints have accelerated rates of cartilage volume loss [8, 47]. Similar degenerative changes have been observed near cartilage defects created in *in vivo* animal models [22, 28]. Despite these findings, the mechanism by which focal defect presence leads to progressive joint degeneration remains unclear.

Changes to the cartilage mechanical environment could contribute to the progression of a focal defect. Excessive mechanical loading can result in macroscopic [24, 36] and microscopic [37, 41, 46] matrix damage and cell death [9, 11, 12, 24, 27, 30, 34, 36, 41]. Over time, even moderate increases in load may be expected to accelerate the rates of both mechanical fatigue [4, 44, 45] and wear [1, 29]. Additionally, changes in the mechanical environment can affect the cellular response of the tissue. Localized cell death reduces the cell population available for tissue maintenance and repair [21], and remaining cells may have reduced metabolic function [27, 36]. In the long-term, mechanical stimuli may regulate the processes of tissue growth and remodeling [16, 19]. Given the influence of mechanical factors on the processes of tissue damage, repair, and remodeling, any changes in those factors

occurring near a focal defect are likely to be critical determinants of the tissue response.

Certain changes in the mechanical environment of a focal defect have been predicted or measured in a variety of animal models. Increases in peak and average contact stresses are measured adjacent to the rim of a focal defect and increased contact stress gradients are present directly at the rim [7, 17]. These results parallel those of studies investigating the mechanical effects of other sources of surface incongruities (i.e. intra-articular step-offs [6, 31, 32], misaligned grafts [26]). However, increases in contact stresses were generally moderate, offset by the recruitment of new contact area [7]; increased deformation of tissue in the normal contact area would be necessary to allow for this redistribution of load onto the surrounding surfaces. Indeed, a recent study revealed the presence of large macroscopic deformations in the tissue surrounding and opposing focal defects [5], and finite element models, showing good agreement with *ex vivo* contact stress measurements, predict increased strains in the tissue adjacent to a defect [35]. Experimental measurements of the intra-tissue strains near a defect site have not yet been quantified and it is unclear how changes in tissue properties (i.e. thickness, curvature, bulk mechanical properties) between species may affect these values.

One approach to assessing the intra-cartilage strain distribution is to use a 2-D experimental model and image the deforming tissue along the cross-section of loaded samples. Previous studies have used similar methods to measure spatial strain variations in biological tissues [39, 40, 42] and cells [15, 18]. These methods have elucidated the marked depth-dependent compressive properties of normal articular

cartilage under both confined [39, 40] and unconfined[42] compression. Subsequent studies have focused on cases of specific clinical interest: the properties tissue-engineered constructs [25], and the strains arising during indentation testing [2] and their relationship to the deleterious biological consequences of high indentation depths [3]. Extension of these techniques to study contact between opposing cartilage surfaces may provide useful insights into normal and pathological cartilage function.

The hypothesis of the current study is that presence of a focal defect alters the contact mechanics of opposing cartilage surfaces, producing elevated, possibly injurious, strains in the adjacent and opposing tissue and inducing sliding between articulating surfaces that may be relevant to tissue wear. Thus, the objective was to characterize these changes by quantifying the distribution of intra-tissue strains and relative surface sliding following uniaxial compression of opposing intact, and defect-containing, cartilage samples. Knowledge of the intra-tissue strains arising near a focal defect could help to identify tissue regions most susceptible to damage and provide data to verify and improve theoretical models of cartilage contact.

2.3 Materials and Methods

Study Design

Mechanical testing was first performed on pairs of intact osteochondral blocks, as a normal control. Following testing, a single, 4 mm wide, full-thickness defect was created in the center of one block from each sample pair. Samples were allowed to re-equilibrate for at least 1 hr in SF+PIs, and then retested using the same mechanical testing protocol.

Sample Preparation

Macroscopically normal osteochondral blocks ($10 \times 10 \times 2.5 \text{ mm}^3$; $L \times W \times H$) with smooth, intact surfaces were harvested from the femoral condyles of adult human ($23 \pm 3 \text{ y.o.}$) knees (Figure 2.1A). Human donor tissue was obtained from tissue banks with donation areas in the Western and Southern areas of the United States. Donors were excluded if they had a history of knee arthritis or if the cause of death was due to a high velocity impact that might cause acute knee injury. Blocks were soaked in phosphate buffered saline (PBS) with the addition of protease inhibitors (PIs) [14] and stored at -70°C until testing. Blocks were thawed by immersion in PBS+PIs, stained (cell nuclei) for at least 4 hr at 4°C with $20 \mu\text{g/ml}$ propidium iodide in PBS+PIs, and then equilibrated for 12 hr at 4°C in bovine synovial fluid (SF)+PIs, to ensure normal surface lubrication. Prior to testing, cartilage thickness was optically measured at 5 places spanning the sample width; sample cartilage thickness was recorded as the average of these 5 measurements (samples averaged a thickness of $2.12 \pm 0.13 \text{ mm}$). Blocks obtained from the same knee were

tested against each other to match the mechanical properties of the opposing sides. A total of $n=4$ pairs of human blocks were tested.

Defects were created by making 3 vertical incisions (center of the sample width, and 2 mm to each side of center) perpendicular to the articular surface and extending through the calcified cartilage layer. The cartilage was then undercut along the bone starting at the center cut and cutting towards each edge until the cartilage released.

Micro-scale Mechanical Testing

Mechanical testing was performed in a microscope-mounted test chamber, as described previously (Figure 2.1B) [2, 25, 39, 40]. Briefly, pairs of blocks were positioned with their articular surfaces opposing and aligned perpendicular to the direction of loading (z-axis). Tissue deformation was imaged through the glass chamber bottom (x-z plane) using a Nikon Diaphot 300 epi-fluorescence microscope fitted with a G-2A filter cube (Nikon, Melville, NY). Samples were imaged at 4x magnification ($\sim 1.8 \times 2.8 \text{ cm}^2$ field of view) and digital images (512x768 pixel resolution) were recorded with a charge-coupled device camera (Model 4913-5000, Cohu, Inc., San Diego, CA). Samples were loaded under uniaxial unconfined compression to a total tissue strain of 20% (defined as the applied displacement/sum of the cartilage thicknesses), at a strain rate of 1%/s using a displacement controlled actuator (Model MFN25PP, Newport Corporation, Irvine, CA). Static digital images of the contacting surfaces were acquired directly prior to, and following (30-45 s after the onset of loading), the application of load.

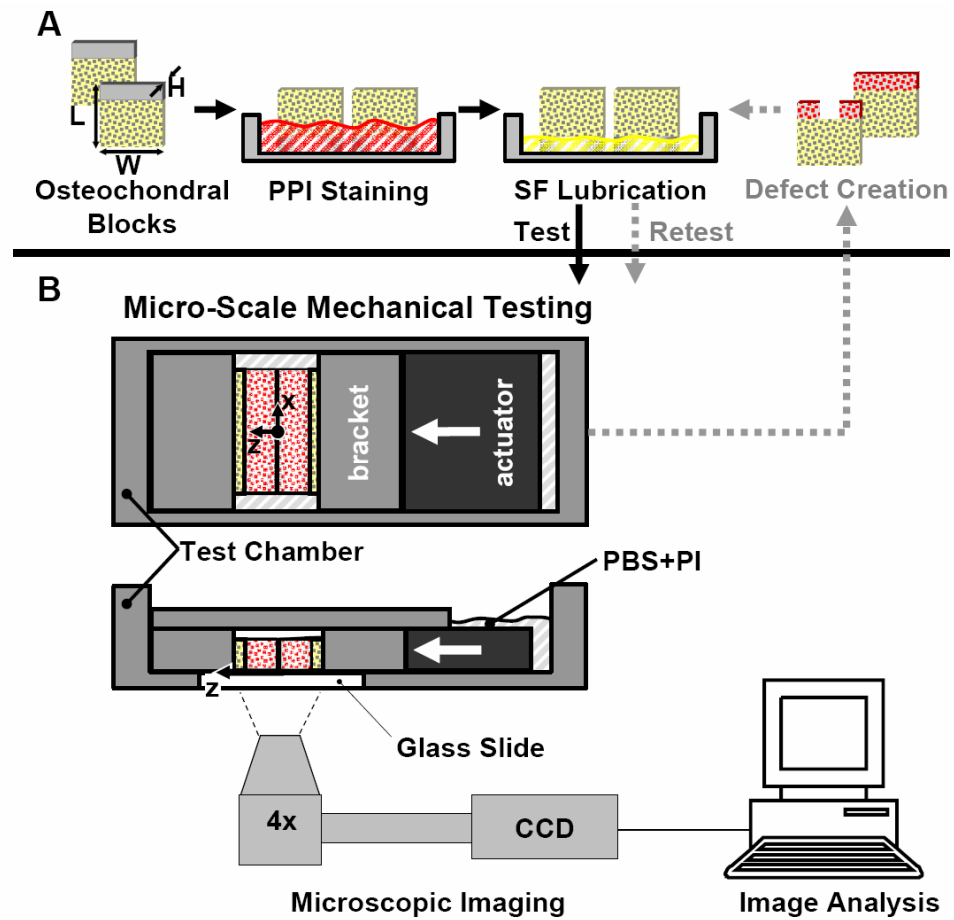


Figure 2.1: Sample preparation (A) and micro-mechanical testing (B) of opposing osteochondral blocks.

Endpoint measures

Indices of the biomechanics of cartilage contact were quantified from the acquired images as outlined in this section and as described in detail below. Macroscopic changes in deformation of the opposing tissue surfaces were observed qualitatively. Intra-tissue strains were calculated at 100 μm spacing, in full-thickness regions of both cartilage layers from the static images acquired directly before and after loading.

Strain values at select sub-regions (Figure 2.2) were then averaged between samples and analyzed statistically to determine the effects of defect presence on the magnitudes and distribution of strain components within the tissue. In the intact case, strains were averaged in rectangular, 100 μm tall (in the z-direction) \times 500 μm wide (in the x-direction) strips at superficial, S (z = surface to 100 μm), middle, M (z = 700 to 800 μm), and deep, D (z = 100 to 200 μm less than the average thickness of each individual sample) depths. In defect samples, strains were quantified in select 100 \times 100 μm^2 sub-regions located at the same three depths as control samples, but at three lateral distances from the defect rim. Along the adjacent cartilage, three lateral positions, with respect to defect edge (x=0), were analyzed: A1 (x = 500 to 600 μm), A2 (x = 200 to 300 μm), and A3 (x = 0 to 100 μm). For the opposing intact cartilage surface, five positions were quantified: O1 (x = 500 to 600 μm), O2 (x = 200 to 300 μm), O3 (x = 50 to -50 μm), O4 (x = -200 to -300 μm), O5 (x = -500 to -600 μm).

Sliding between surfaces was estimated by calculating the relative lateral (in the x-direction) displacement (RLD) of each point on the surface of the ROI, with

respect to the point on the opposing surface that was adjacent to it prior to loading. In intact control samples, the average RLD over the 500 μm analysis region was calculated. For defect samples, RLD's were calculated at several points along the adjacent cartilage surface ($x = 0, 100, 200, 300, 400, 500 \mu\text{m}$).

Automated Tracking of Fiducial Markers

Tissue deformation was quantified in digital images using a hybrid of the discrete point tracking [39] and digital image correlation [42] methods. Fluorescently stained nuclei served as fiducial markers of material points in digital images of the tissue in its initial and deformed states. Cell tracking was performed and deformation was calculated using a custom program written in MATLAB 6.5 using functions from the Image Processing Toolbox (Mathworks, Inc., Natick, Massachusetts).

Images from each cartilage block were analyzed individually. Cell nuclei in the initial, unloaded image were isolated by segmenting and intensity thresholding the image using methods described previously [23]. A region of interest (ROI) was manually selected in the initial image to analyze full-thickness deformations. Centroids of the nuclei lying within this ROI were determined, and a subset of these points, spaced at $\sim 50 \mu\text{m}$, was selected for tracking. To provide an initial guess for the positions of selected markers in the deformed image, a set of points (~ 40), spaced throughout the ROI, were selected and manually matched to their positions in the deformed image.

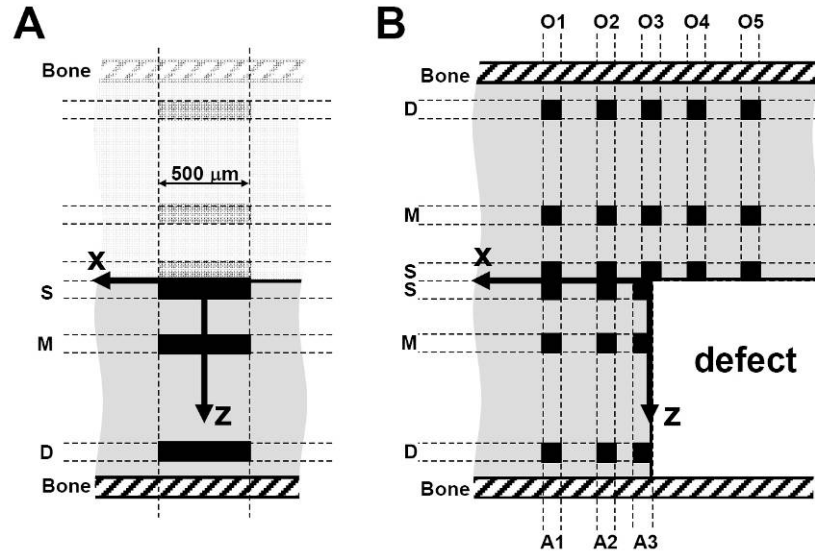


Figure 2.2: Locations of sub-regions used for statistical analysis of strain distributions in (A) intact control and (B) defect-containing samples. Measurements were made at three tissue depths: S { $z = 0:100 \mu\text{m}$ }; M { $z = 700:800 \mu\text{m}$ }, D { $z = [\text{thickness}-200]:[\text{thickness}-100]$ }. For intact control samples, a $500 \mu\text{m}$ width region was averaged to calculate a control strain value at each depth. For defect samples, $100 \times 100 \mu\text{m}$ sub-regions were analyzed for S, M, and D depths at select lateral locations on the adjacent (A1 { $x = 500:600 \mu\text{m}$ }; A2 { $x = 200:300 \mu\text{m}$ }; A3 { $x = 0:100 \mu\text{m}$ }) and opposing (O1 { $x = 500:600 \mu\text{m}$ }; O2 { $x = 200:300 \mu\text{m}$ }; O3 { $x = -50:50 \mu\text{m}$ }; O4 { $x = -200:-300 \mu\text{m}$ }; O5 { $x = -500:-600 \mu\text{m}$ }) cartilage surfaces.

Fiducial marker positions in the deformed image were first estimated from the displacements of the manually matched points. The position of each marker was then adjusted by a series of four correlation steps, maximizing normalized cross-correlation of equally-sized regions (centered on the marker) in the initial and deformed images. First, marker positions were coarsely adjusted using 20×20 pixel ($\sim 75 \times 75 \mu\text{m}$) regions, followed by fine adjustment using 5×5 ($\sim 20 \times 20 \mu\text{m}$) pixel regions. The displacements of the tracked markers were then used to compute theoretically-deformed images. To fit the 2-D deformation data the ROI was divided into 6 equally sized areas ($3 \text{ lateral} \times 2 \text{ depth}$) and the displacements of the points in those regions were used to calculate a bi-quadratic equation (of the form $A+Bx+Cz+Dx^2+Ez^2+Fxz$) describing deformation of the region. The transformation was then applied to the initial image and marker positions, generating a theoretically-deformed image/marker set for that sub-region. Coarse and fine adjustments were repeated as described above, but this time correlating to the corresponding theoretically-deformed image. These steps helped improve correlation and marker positioning in areas of large deformations. Poorly correlated points (where normalized cross-correlation of all four correlation steps fell below 0.40) were excluded from further calculations.

Calculations of Intra-Tissue Strain and Relative Tissue Movement

The contacting surface contours were defined by a smoothing spline fit to ~ 10 manually positioned points spanning the sample widths in both the initial and deformed images. This independent definition of the surface provided a boundary for calculations since tracking of points close to contacting surfaces was sometimes problematic due to the high deformations in the surface regions. Inter-user variability

(3 independent observers) of axial surface calculations was calculated to be $< \pm 2$ pixels and was highest for compressed surfaces; this error translates to variability of < 0.03 on axial strain measurements, in regions that were typically > 0.30 and > 0.40 for intact and defect samples, respectively.

Movements of the surface and tracked cell nuclei were used to update a uniform mesh of points that was used for all calculations of displacements, displacement gradients, and strains. The initial mesh-point positions, evenly spaced at $100\ \mu\text{m}$, were defined in the ROI in the initial, undeformed image. The starting locations of the mesh-point rows and columns were defined using the physical features of the samples: the axial positions of the surfaces and, when applicable, the lateral position of the defect edge ($x=0$). For the defect case, lateral position of the defect edge was manually chosen in the initial image as the point along the edge that was furthest away from the defect center. The lateral positions of mesh columns were defined at $100\ \mu\text{m}$ spacing until reaching the edge (or both edges, in the case of the opposing cartilage surface) of the chosen ROI. For the intact case, mesh columns were defined starting in the center of the ROI. For both intact and defect samples the axial (z -) positions of the mesh points lying closest to the surface were calculated from the lateral column positions and the surface spline. The remaining rows of points were defined at $100\ \mu\text{m}$ spacing from the inner-most surface point.

The position of each mesh-point not located along the contacting surface was determined in the compressed state using a local affine mapping of any tracked nuclei in the surrounding region (~ 16 nuclei, representing an $\sim 200 \times 200\ \mu\text{m}$ region), an arrangement that helped limit the effect of small errors in individual point tracking on

subsequent calculations and allowed poorly-correlated points (correlation < 0.4 for all correlation steps - the threshold where manual verification became difficult) to be excluded from the calculation of results. For points on the articular surface, the lateral position was calculated using the same affine mapping procedure, and used to calculate the deformed axial position from the surface spline. In regions without at least four well-correlated points, positions were updated using the positions of the neighboring mesh-points that had been successfully positioned. Displacement gradients were calculated at each mesh-point by finite difference approximations. Lagrangian strains were calculated from displacement gradients and then used to compute the principal strains and directions.

In-plane area changes in the contacting cartilage surfaces were calculated from the displacement gradients at each point. Since large deformations were present in many tissue regions, the change in area at each point was calculated as:

$$\frac{dA - dA_0}{dA_0} = \det \begin{pmatrix} 1 + \frac{\partial u}{\partial x} & \frac{\partial u}{\partial z} \\ \frac{\partial w}{\partial x} & 1 + \frac{\partial w}{\partial z} \end{pmatrix} \quad (1)$$

Estimates of local volumetric changes were also calculated within the tissue. Since only 2-D measurements were recorded in the current experimental setup, out-of-plane displacement gradients were approximated from values of in-plane displacement gradients measured in intact control samples. Volume changes could then be estimated using equation (1) with components in 3 dimensions.

The cartilage surfaces were assumed to be a transversely isotropic material, with properties being equal in the plane parallel to the articular surface (x and y). In

the current setup, this allows the out-of-plane strains in the intact control samples to be approximated as equal to the strains in the lateral direction. Using this assumption, it is possible to define:

$$\frac{\partial v}{\partial y} = \frac{\partial u}{\partial x} \quad (2)$$

$$\frac{\partial v}{\partial z} = \frac{\partial u}{\partial z} \quad (3)$$

$$\frac{\partial w}{\partial y} = \frac{\partial w}{\partial x} \quad (4)$$

Next, the shear gradients in the x-y plane were assumed to be negligible, so:

$$\frac{\partial v}{\partial x} = 0 \quad (5)$$

$$\frac{\partial u}{\partial y} = 0 \quad (6)$$

For the defect case, high values of shear and tension develop in the lateral in-plane direction in both the adjacent and opposing surfaces because of the surface incongruity at the defect edge. However, the out-of-plane direction (parallel to the defect edge) does not see the same incongruity and would likely experience strains similar to those measured in the intact case. Therefore, out-of-plane displacement gradients in the defect samples were approximated as:

$$\frac{\partial v}{\partial y} = \text{average } \frac{\partial u}{\partial x} \text{ at same depth of intact control samples} \quad (7)$$

$$\frac{\partial v}{\partial z} = \text{average } \frac{\partial u}{\partial z} \text{ at same depth of intact control samples} \quad (8)$$

$$\frac{\partial w}{\partial y} = \text{average } \frac{\partial w}{\partial x} \text{ at same depth of intact control samples} \quad (9)$$

$$\frac{\partial v}{\partial x} = 0 \quad (10)$$

$$\frac{\partial u}{\partial y} = 0 \quad (11)$$

Using those assumptions, volume changes could be calculated as:

$$\frac{dV - dV_0}{dV_0} = \det \begin{pmatrix} 1 + \frac{\partial u}{\partial x} & \frac{\partial u}{\partial y} & \frac{\partial u}{\partial z} \\ \frac{\partial v}{\partial x} & 1 + \frac{\partial v}{\partial y} & \frac{\partial v}{\partial z} \\ \frac{\partial w}{\partial x} & \frac{\partial w}{\partial y} & 1 + \frac{\partial w}{\partial z} \end{pmatrix} \quad (12)$$

The computational image analysis was validated using theoretically-generated sequential image sets of rigid body translation and rotation or large homogeneous deformations in tension, compression, and shear. Calculated strain values (data not shown) were found to be accurate to within 0.01 for regions under large deformations (axial strains of -0.32 to 0.48; shear strains of 0.10), with errors tending to decrease at smaller deformations.

Measured RLD's were considered to be a combination of two separate components: 1) the inherent sliding between a particular pair of cartilage blocks and 2) the sliding caused by a defect. During loading of intact blocks, the direction of sliding varied depending on the characteristics of the individual blocks. On the other hand, sliding near a defect always took place in the same direction, with the adjacent cartilage moving towards the defect with respect to the opposing surface. Thus, in cases where significant sliding occurs between the intact surfaces, sliding at a defect

may be exaggerated when the two contributions are in the same direction, and reduced when the two contributions are in opposite directions. In order to better discern the effects of a focal defect, the average relative lateral displacement (RLD) between the surfaces in the intact configuration was subtracted from RLD measurements for the analyzed surfaces in intact and defect samples. For each surface, lateral (x-direction) displacement was fit to a linear function of x- position (Figure 2.3). The average RLD for the intact surfaces was then determined as the difference between the lateral displacements calculated from the two equations at $x=0$ (the center of the block width). The average RLD for the intact blocks was then subtracted from the calculated RLD's in regions of interest in both the intact and defect samples. All RLD data is reported as these differential values.

For each sample, the average sliding distance over the analyzed 500 μm surface region (adjacent to the defect or in the center of intact samples) was calculated and normalized to the ~applied axial displacement. The average normalized RLD for the $n=4$ sample pairs was calculated for both the intact and defect configurations.

Statistics

Data are presented as mean \pm SEM unless otherwise noted. A total of $n=4$ pairs of blocks were tested; each pair of blocks was first tested in the intact state and then the same pair was re-tested following the creation of a focal defect. For tests of opposing intact surfaces, strain data from the two opposing surfaces were pooled to provide one set of strain measurements (at S, M, and D depths) per control sample pair. For defect-containing blocks, several lateral locations along the adjacent and opposing cartilage surfaces (as described earlier) were analyzed. All data was log

transformed before analysis to adjust for the uneven sample variances. Statistical analyses ($\alpha=0.05$) were performed using Systat 10.2.05 (Systat Software, Richmond, CA) and Microsoft Office Excel 2003 (Microsoft Corporation, Redmond, WA).

The overall effects of tissue depth (S, M, D) and surface location (9 groups: control, C; 3 locations on the adjacent surface, A1-A3; and 5 locations on the opposing surface, O1-O5) were analyzed by two-way repeated measures ANOVA, with tissue depth as a repeated measure. Additionally, planned comparison (*a priori*) t-tests (for uneven variances) were used to compare the values of strain at each position (S, M, and D depths at locations A1-A3, O1-O5) along the adjacent and opposing surfaces to the control value at the same depth: the choices of comparisons were made to elucidate the differences in cartilage deformation in surfaces adjacent to and opposing a focal defect, compared to that experienced by contacting intact surfaces.

The power of the planned comparisons to detect differences from control values was assessed. Using typical standard deviations ($\sigma=0.05$) for our samples, we could expect to detect differences in strain magnitudes of 0.10 (~33% change from control) with a Power = 0.66. Higher sample numbers would be necessary if smaller changes in strain magnitudes were of interest (Power = 0.22 for difference of 0.05), but changes in strain magnitudes below a certain threshold may not have significant physiological effects. In deeper regions, where strain magnitudes were significantly lower, variances were also smaller ($\sigma=0.03$), allowing differences in strains of 0.05 to be detected with a Power = 0.50.

Planned comparisons were also used to compare the relative lateral displacements at points along the surface adjacent to the defect rim, to the average relative lateral displacement between intact control surfaces. The average normalized sliding distance for the surface adjacent to the defect and the intact surfaces were compared using a t-test.

Power of sliding comparisons was also calculated. At the fully-compressed time-point, differences of 30 μm in sliding could be detected with Power=0.50, while 40 μm differences (~equal to the sliding experienced by intact controls) could be detected with Power=0.80 (assuming typical values of $\sigma=15$ μm for intact controls and $\sigma=20$ μm for defect samples). Generally, the standard deviations of sliding distances were proportional to the magnitudes of sliding, and power remained high for differences ~equal to control magnitudes.

2.4 Results

In intact cartilage samples, both opposing cartilage surfaces deformed similarly. The superficial regions displayed noticeably higher compressive axial deformation than the deeper cartilage, which was only slightly deformed. Relatively little sliding was observed between the contacting surfaces.

In the defect case, greater gross deformation of the surfaces was apparent. Cartilage adjacent to the defect expanded laterally into the defect, and the opposing surface “mushroomed” into the empty defect region (Figure 2.3). The cartilage adjacent to the defect rim appeared to collapse. Regions of the opposing surface lying over the empty defect and sufficiently far from the defect rim appeared undeformed. Lateral sliding between the surfaces was apparent near the defect, with the adjacent tissue moving toward and into the defect, relative to the opposing side.

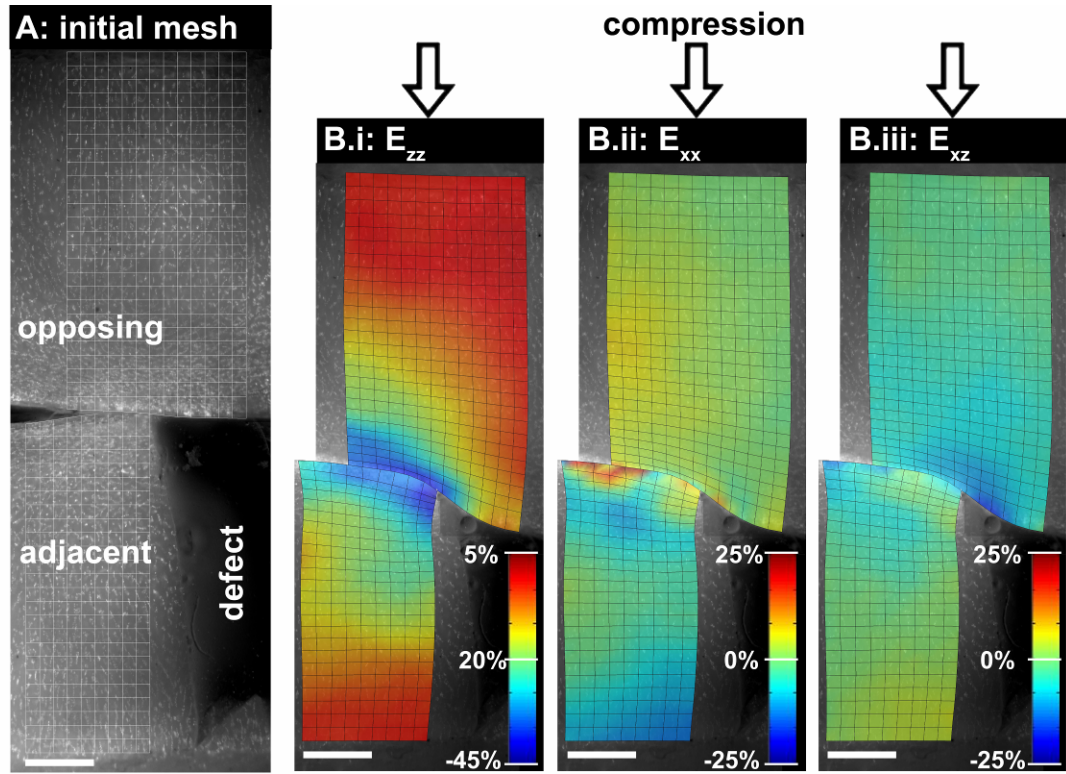


Figure 2.3: Representative defect sample before loading (A), showing the initial, undeformed mesh, and after loading (B), with superimposed contour maps of axial (B.i), lateral (B.ii) and shear (B.iii) strains.

Strains in intact control, C, samples (Figure 2.4) displayed a depth-varying distribution of axial compressive strain. Compressive strain was highest at the articular surface, averaging -0.28 ± 0.04 in the S regions, and decreased significantly with tissue depth ($p < 0.005$), reaching values of -0.20 ± 0.03 in the M regions, and plateauing to -0.09 ± 0.03 in the deeper zones. E_{xx} and $|E_{xz}|$ magnitudes were low throughout the tissue, averaging ≤ 0.05 in all regions; however, these variations were statistically significant, showing a decrease in lateral strain and increase in shear strain with increasing tissue depth ($p < 0.05$).

Overall, strain magnitudes of E_{zz} , E_{xx} , and $|E_{xz}|$ varied significantly with tissue depth ($p < 0.01$) and sample location ($p < 0.01$), with a significant interaction between depth and location for E_{zz} ($p < 0.01$) and $|E_{xz}|$ ($p < 0.05$) (Figure 2.4 and 2.5). The largest increases in strain magnitudes occurred near the defect rim, for both contacting surfaces, while the only significant reductions in strain magnitude occurred in the non-contacting regions of the opposing surface. For the most part, changes in strain distributions were concentrated in the S and M regions, with very few changes in the D region.

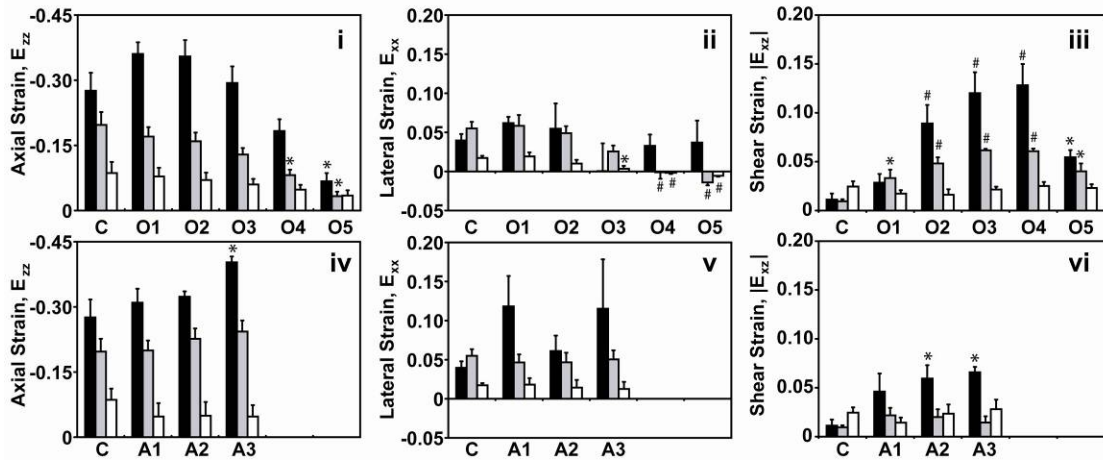


Figure 2.4: Strain measurements at selected sub-regions in opposing cartilage surfaces. Strains were calculated in $100 \times 100 \mu\text{m}^2$ sub-regions at S (■), M (■), and D (□) depths for several lateral positions along the cartilage surfaces adjacent (A1-A3) and opposing (O1-O5) a focal defect. Strain in each sub-region was compared to the value from intact control samples (C) at the corresponding depth (*p<0.05; #p<0.01; †p<0.001). Data are expressed as mean \pm SEM. n=4.

In the tissue adjacent to the defect, strains were significantly elevated compared to intact control values. At the defect rim (A3-S), E_{zz} compression reached -0.40 ± 0.01 ($p < 0.05$). Significantly higher $|E_{xz}|$ magnitudes along the adjacent surface (A2:A3-S) were also observed ($p < 0.05$).

Strain distributions were also significantly altered in the opposing cartilage surface, with increased shear magnitudes near the defect rim and diminishing strain magnitudes in the regions overlying the defect. E_{zz} did not differ significantly from controls at locations (O1, O2, O3) remaining in contact with the tissue adjacent to the defect ($p > 0.10$), but were significantly reduced in S and M regions at locations over the empty defect ($p < 0.05$), approaching zero away from the rim (O5). E_{xx} was significantly reduced at locations O4 and O5 ($p < 0.05$), with strains approaching or surpassing zero at all depths. Elevations in $|E_{xz}|$ magnitudes were measured in S and M depths at locations opposing (O3), and near (O2, O4) the defect rim ($p < 0.01$), peaking at > 0.10 .

Distributions of area and volume loss (Figure 2.6) closely resembled that of axial strain, with substantial compaction ($> 20\%$ volume loss) of tissue near the articular surface. The magnitudes of area and volume loss decreased with tissue depth and were negligible in the deep regions. In defect samples, significantly greater area, -0.55 ± 0.03 , and volume, -0.54 ± 0.04 , loss were measured at the defect rim ($p < 0.05$), than in the superficial regions in intact controls: -0.32 ± 0.07 and -0.29 ± 0.07 , respectively.

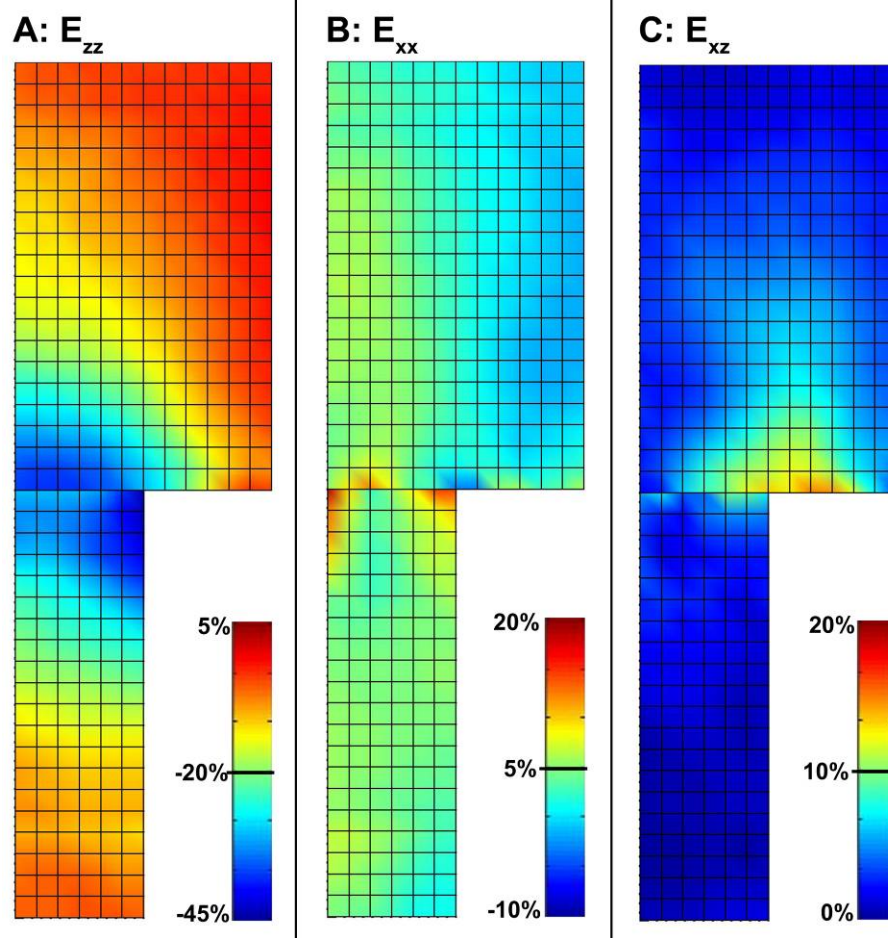


Figure 2.5: Composite contour maps of axial (A), lateral (B) and shear (C) strains of contacting surfaces in defect samples, for regions $\pm 600 \mu\text{m}$ laterally from the defect and 0-2 mm in tissue depth.

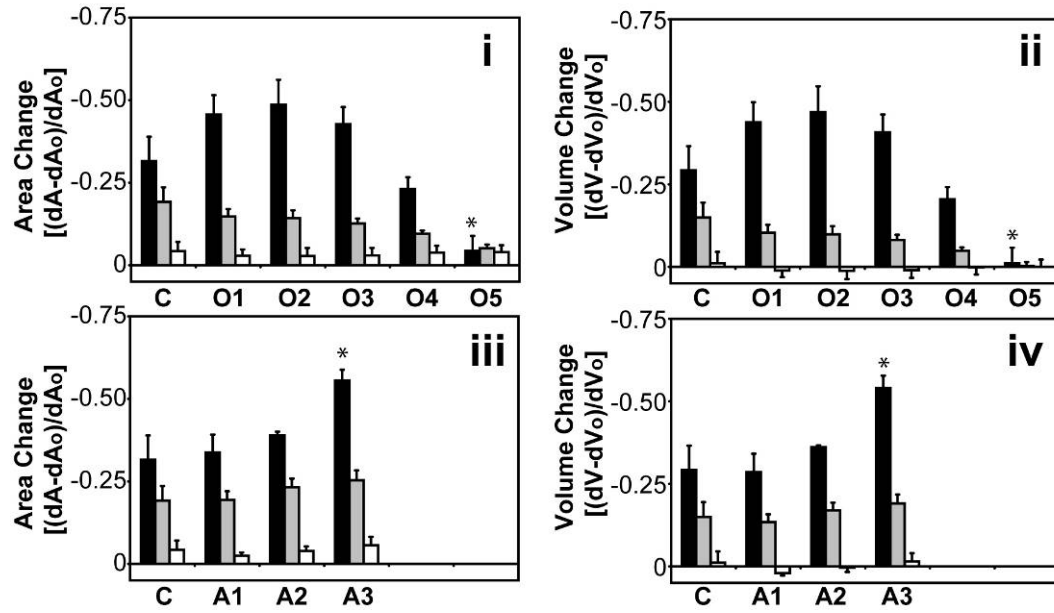


Figure 2.6: Area (i,iii) and volume (ii,iv) changes at selected sub-regions in opposing cartilage surfaces. Strains were calculated in $100 \times 100 \mu\text{m}^2$ sub-regions at S (■), M (■), and D (□) depths for several lateral positions along the cartilage surfaces adjacent (A1-A3) and opposing (O1-O5) a focal defect. Strain in each sub-region was compared to the value from intact control samples (C) at the corresponding depth (* $p < 0.05$; # $p < 0.01$; † $p < 0.001$). Data are expressed as mean \pm SEM. $n=4$.

Measurements of RLD (Figure 2.7) showed strong trends towards increased sliding near defects, but were complicated by high variability between individual samples. Higher magnitudes of adjusted RLD were measured between the surfaces near the defect rim (averaging $>30\text{ }\mu\text{m}$) than for the control samples ($7 \pm 2\text{ }\mu\text{m}$), but these increases did not reach statistical significance. However, the average normalized RLD was significantly higher for the surfaces near defects, 0.08 ± 0.03 , than for intact controls, 0.02 ± 0.01 . Sliding between surfaces near a defect always took place in a qualitatively similar fashion, with the adjacent cartilage moving toward the defect, relative to the opposing surface.

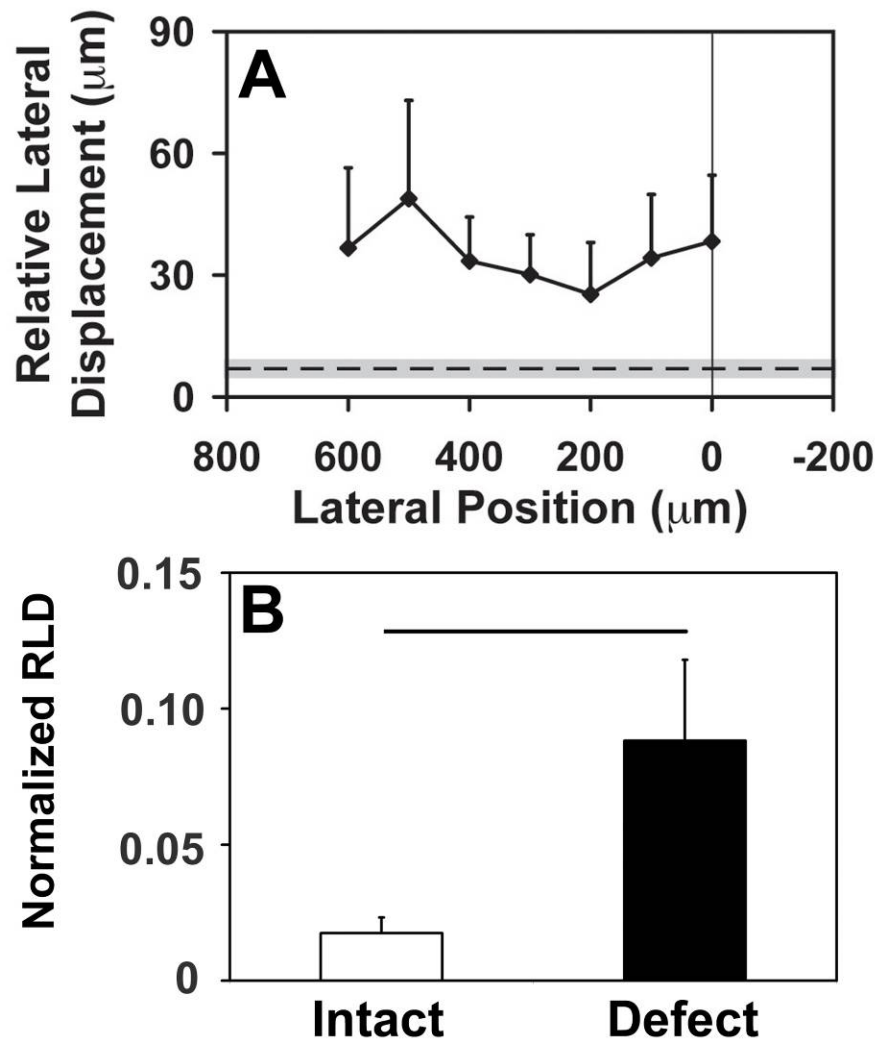


Figure 2.7: Adjusted relative lateral displacement (RLD) profiles and average normalized RLD. **A:** Profiles of RLD are plotted for points along the surfaces adjacent to defects (solid lines) are compared to the average RLD of points along the contacting intact control surfaces (mean: dashed line; SEM grey region). **B:** average RLD, normalized to the applied axial displacement, for intact surfaces (white) and surfaces adjacent to defects (black). $n=4$. (bar = $p<0.05$).

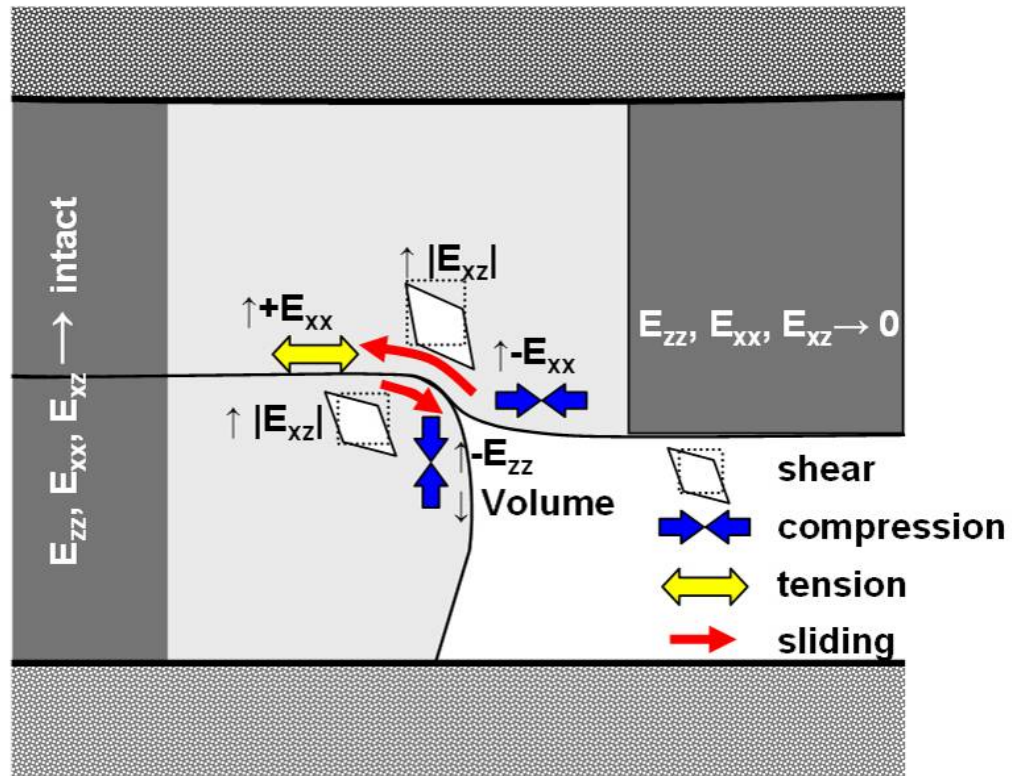


Figure 2.8: Summary of the effects of defects on cartilage mechanics.

2.5 Discussion

This study employed micro-scale mechanical testing to investigate changes in the cartilage deformation in regions near a focal chondral defect. The results confirm that defect presence has dramatic effects on macroscopic cartilage deformation and intra-tissue strain distribution under uniaxial compressive loading (Figure 2.8). Following compression, the tissue adjacent to the defect partially collapses laterally into the defect, and significant strain elevations are seen along the defect edge. In the tissue opposing the defect rim, the transition from contacting to non-contacting regions is marked by a shift in lateral strain from tension to compression and high magnitudes of shear strain. The “bending” of the adjacent cartilage into the defect region induced sliding between the contacting surfaces, manifest as the net relative lateral displacement of the two surfaces. The observed increases in local strain magnitudes and sliding may be relevant to mechanical wear and fatigue processes.

The current study quantified strains by optically tracking fiducial markers in a 2-D sample cross-section during loading. Similar setups have been successfully used in the past to measure spatially-varying intra-tissue cartilage strains in a variety of loading configurations [2, 25, 39, 40, 42]; however, some of the measured strain values may be affected by this 2-D configuration. The preparation of the cartilage blocks may eliminate some of the tangential stresses that may help to distribute load. Also, the defects in this model would be unable to develop a circumferential hoop stress at the defect rim that might help to resist deformation *in vivo*. Testing was performed in an unconfined geometry, with tissue depressurization possible through

the top and edges of the sample; this is most appropriate for modeling defects where depressurization is allowed because 1) defect size or surface curvatures prevent the opposing surface from producing a seal along the defect rim, or 2) the subchondral bone is compromised.

A loading protocol was chosen to provide a conservative comparison of the biomechanics of control and defect situations. Loading in the current study consisted of compression applied axially in displacement control at a constant strain rate, and with intact and defect-containing samples compressed to the same level of total bone-to-bone strain. This loading is simplified compared to that of the *in vivo* environment, which would include both lateral and axial components and where strain and strain rates would depend upon the joint loading during articulation. The compression to a common total tissue strain likely leads to an underestimate of the effects of defects, since the loss of load-bearing surface area and possible changes in mechanical properties of the adjacent tissue would likely lead to higher levels of total strain and strain rate. It is then notable that significant local strain elevations occurred, even under this conservative loading protocol. Conversely, compression of samples to a common load would likely overestimate the effects of defects, since the samples used here would be unable to distribute the load to the surrounding areas, as is expected *in vivo* [7]. Physiological loading conditions would likely fall somewhere between those two approximations; predictions of defect behavior under physiological loading could be estimated by adjusting the loading conditions of different experimental groups using data from *ex vivo*, whole-joint studies or finite element models. The applied strain rate (1%/s) was chosen to fall below the threshold known to induce tissue

damage, but still provide measurements that are representative of an instantaneous loading response [13,33].

The accuracy of image analysis techniques used here, was comparable (in performance on theoretically generated image sets) to that reported previously. Image analysis was performed using a hybrid approach of previous direct point tracking [39, 40] and digital image correlation [2, 42] techniques. Here, translations of a subset of cell nuclei, acting as fiducial markers, were tracked by maximizing normalized cross-correlation. Unlike digital image correlation approaches, where correlation is maximized for both translation and deformation of a region and gradient calculations are computed from those deformations, the current approach maximizes only for point displacement and calculates gradients from the relative movement of markers. This allows the results of the correlation steps to be easily verified by manual inspection, but avoids the labor intensive process of directly matching each point.

Measured axial strain distributions in intact control samples were qualitatively similar to previous reports [2, 39, 40, 42], showing significant decreases in strain with increasing tissue depth. The depth-wise distribution of strain differed slightly from previous studies, with peak strains tending to be slightly lower in the superficial region and slightly higher in the deep regions; however, differences in test parameters (e.g. presence or absence of underlying bone, unconfined vs. confined compression, relaxation time, and tissue source) prohibit direct comparison of the independent results. Strain data are reported as components in the axial and lateral directions, with the corresponding shear strain (as opposed to principal and maximum shear strains), since in a highly anisotropic tissue, such as cartilage, the effects of strains may depend

not only on their magnitudes, but also on their orientation with respect to the tissue structure. At lateral positions away from the defect edge, principal axes tended to closely align with the x- and z- axes, as seen by the low values of shear strain in those regions (Figure 2.5).

In the defect case, cartilage surfaces experienced elevated axial compression and lateral tension in the tissue adjacent to the defect, with strain elevations generally more confined to the surface regions. The samples also showed sharp increases in shear strain in the region contacting the defect rim and fluctuations between regions of tension and compression in the lateral direction. Although no directly comparable studies have been performed, the behavior of defect samples is in agreement with previous observations. The macroscopic deformation was similar to observations by Braman et al [5], while the trend for lower compression in the tissue directly opposing the defect rim corresponds well to reports that peak contact pressures occur near, but not at, the defect rim [7].

In the joint environment, defect behavior may also be influenced by several additional parameters. Foremost among them, inclusion of a lateral component of load may significantly influence strain distributions, with the protrusion of the opposing surface into the defect providing considerable resistance to lateral motion. Normal variations in cartilage thickness, mechanical properties, and surface curvatures, as well as the size and edge characteristics of the defect, could contribute to changes in contact mechanics. One of these effects was qualitatively observed in the current study; strain patterns directly at or opposing the defect rim and sliding between the surfaces in that region showed large variabilities that may have been governed by the

orientation of the defect edge (i.e. angle formed by the defect base and edge). An “open” defect orientation (i.e. angle $> 90^\circ$), where tissue at the base extends further into the defect than tissue at the rim (such as the defect in Figure 2.3), seems to result in a greater lateral compaction of the rim and a more abrupt transition in the opposing surface. A more “closed” defect angle (i.e. angle $< 90^\circ$), where there is excess tissue at the surface without support directly below it, tended to produce higher lateral tension and shear in the adjacent surface and a more gradual transition in the surface opposing the rim. The defect orientation also seems to affect the amount of sliding between surfaces at the defect edge, with higher magnitudes occurring near defects with a “closed” orientation. It is unclear if either these situations is physiologically preferable, although very large (135°) defect angles have been associated with negative *in vivo* outcomes [38].

The use of *in vitro* experimental model systems to study the effects of focal defects may allow for the determination of critical size thresholds where changes in cartilage contact are observed. In the current study, it is possible to estimate the minimum defect size that allows the opposing surface to completely transition to an uncompressed state in the region over the empty defect. Here, we will define this radius as the lateral distance from the point on the opposing surface that begins in contact with the defect rim, to the point where axial strain in the opposing surface equals zero. This was determined by fitting a cubic equation of x (lateral position) to the corresponding values of E_{zz} . Solving that equation using the current experimental results, gave a critical radius (R_{crit}) of $768 \mu\text{m}$. Since the transition radius is likely to depend on the applied axial displacement on the surface (which is, in turn, equal to

thickness \times applied total strain), it may be useful to express this distance in terms of these experimental parameters: average thickness of the opposing surfaces (h) and the applied compressive strain (ϵ_c). Doing this provides the relationship, $R_{crit} = Ch\epsilon_c$, where C is an experimentally derived parameter. For the current study, C was estimated to be 1.85.

The high level of strain present at the defect rim may play a crucial role in the continued progression of a defect. Using a conservative (equal applied displacement) loading protocol, local strain elevations still exceeded magnitudes that have been previously linked to cell [12, 27, 30, 34, 36] and matrix damage [36, 41]. Even in the absence of such acute damage, mechanical overload could contribute to accelerated rates of wear and fatigue over long-term loading [1]. Investigation of how the observed strain concentrations correlate to regions of cell or matrix damage may provide insights into disease progression. The current study could be extended, to investigate the mechanical performance (i.e. the ability to prevent abnormal strain development in adjacent or opposing tissue) of common repair strategies and gauge the relative significance of factors such as bulk material properties and host-graft integration to restoring normal mechanical function.

2.6 Acknowledgments

This chapter has been submitted, in full, for publication in *Biorheology*. The dissertation author is the primary investigator and thanks co-authors Ben Wong and Drs. Won Bae and Robert Sah. This work was supported in part by the National Institutes of Health and the National Science Foundation, and by a grant to the University of California, San Diego, in support of Dr. Robert Sah, from the Howard Hughes Medical Institute through the Professors Program.

2.7 References

1. Ateshian GA, Mow VC: Friction, lubrication, and wear of articular cartilage and diarthrodial joints. In: *Basic Orthopaedic Biomechanics and Mechano-Biology*, ed. by VC Mow, Huiskes R, Lippincott Williams & Wilkins, Philadelphia, 2005, 447-94.
2. Bae WC, Lewis CW, Levenston ME, Sah RL: Indentation testing of human articular cartilage: effects of probe tip geometry and indentation depth on intra-tissue strain. *J Biomech* 39:1039-47, 2006.
3. Bae WC, Schumacher BL, Sah RL: Indentation probing of human articular cartilage: effect on chondrocyte viability. *Osteoarthritis Cartilage* 15:9-18, 2007.
4. Bellucci G, Seedhom BB: Mechanical behaviour of articular cartilage under tensile cyclic load. *Rheumatology (Oxford)* 40:1337-45, 2001.
5. Braman JP, Bruckner JD, Clark JM, Norman AG, Chansky HA: Articular cartilage adjacent to experimental defects is subject to atypical strains. *Clin Orthop Relat Res* 430:202-7, 2005.
6. Brown TD, Anderson DD, Nepola JV, Singerman RJ, Pedersen DR, Brand RA: Contact stress aberrations following imprecise reduction of simple tibial plateau fractures. *J Orthop Res* 6:851-62, 1988.
7. Brown TD, Pope DF, Hale JE, Buckwalter JA, Brand RA: Effects of osteochondral defect size on cartilage contact stress. *J Orthop Res* 9:559-67, 1991.
8. Cicuttini F, Ding C, Wluka A, Davis S, Ebeling PR, Jones G: Association of cartilage defects with loss of knee cartilage in healthy, middle-age adults: a prospective study. *Arthritis Rheum* 52:2033-9, 2005.
9. Clements KM, Bee ZC, Crossingham GV, Adams MA, Sharif M: How severe must repetitive loading be to kill chondrocytes in articular cartilage? *Osteoarthritis Cartilage* 9:499-507, 2001.
10. Curl WW, Krome J, Gordon ES, Rushing J, Smith BP, Poehling GG: Cartilage injuries: a review of 31,516 knee arthroscopies. *Arthroscopy* 13:456-60, 1997.
11. D'Lima DD, Hashimoto S, Chen PC, Colwell CW, Jr., Lotz MK: Human chondrocyte apoptosis in response to mechanical injury. *Osteoarthritis Cartilage* 9:712-9, 2001.
12. D'Lima DD, Hashimoto S, Chen PC, Lotz MK, Colwell CW, Jr.: Cartilage injury induces chondrocyte apoptosis. *J Bone Joint Surg Am* 83-A Suppl 2:19-21, 2001.
13. Frank EH, Grodzinsky AJ: Cartilage electromechanics-I. Electrokinetic transduction and the effects of electrolyte pH and ionic strength. *J Biomech* 20:615-27, 1987.

14. Frank EH, Grodzinsky AJ, Koob TJ, Eyre DR: Streaming potentials: a sensitive index of enzymatic degradation in articular cartilage. *J Orthop Res* 5:497-508, 1987.
15. Gilchrist CL, Witvoet-Braam SW, Guilak F, Setton LA: Measurement of intracellular strain on deformable substrates with texture correlation. *J Biomech* 40:786-94, 2007.
16. Grodzinsky AJ, Levenston ME, Jin M, Frank EH: Cartilage tissue remodeling in response to mechanical forces. *Annu Rev Biomed Eng* 2:691-713, 2000.
17. Guettler JH, Demetropoulos CK, Yang KH, Jurist KA: Osteochondral defects in the human knee: influence of defect size on cartilage rim stress and load redistribution to surrounding cartilage. *Am J Sports Med* 32:1451-8, 2004.
18. Guilak F, Ratcliffe A, Mow VC: Chondrocyte deformation and local tissue strain in articular cartilage: a confocal microscopy study. *J Orthop Res* 13:410-21, 1995.
19. Guilak F, Sah RL, Setton LA: Physical regulation of cartilage metabolism. In: *Basic Orthopaedic Biomechanics*, ed. by VC Mow, Hayes WC, Raven Press, New York, 1997, 179-207.
20. Hjelle K, Solheim E, Strand T, Muri R, Brittberg M: Articular cartilage defects in 1,000 knee arthroscopies. *Arthroscopy* 18:730-4, 2002.
21. Hunziker EB, Quinn TM: Surgical removal of articular cartilage leads to loss of chondrocytes from cartilage bordering the wound edge. *J Bone Joint Surg Am* 85-A Suppl 2:85-92, 2003.
22. Jackson DW, Lalor PA, Aberman HM, Simon TM: Spontaneous repair of full-thickness defects of articular cartilage in a goat model. A preliminary study. *J Bone Joint Surg Am* 83-A:53-64, 2001.
23. Jadin KD, Wong BL, Bae WC, Li KW, Williamson AK, Schumacher BL, Price JH, Sah RL: Depth-varying density and organization of chondrocyte in immature and mature bovine articular cartilage assessed by 3-D imaging and analysis. *J Histochem Cytochem* 53:1109-19, 2005.
24. Jeffrey JE, Gregory DW, Aspden RM: Matrix damage and chondrocyte viability following a single impact load on articular cartilage. *Arch Biochem Biophys* 322:87-96, 1995.
25. Klein TJ, Chaudhry M, Bae WC, Sah RL: Depth-dependent biomechanical and biochemical properties of fetal, newborn, and tissue-engineered articular cartilage. *J Biomech* 40:182-90, 2007.
26. Koh JL, Wirsing K, Lautenschlager E, Zhang LO: The effect of graft height mismatch on contact pressure following osteochondral grafting. A biomechanical study. *Am J Sports Med* 32:317-20, 2004.

27. Kurz B, Jin M, Patwari P, Cheng DM, Lark MW, Grodzinsky AJ: Biosynthetic response and mechanical properties of articular cartilage after injurious compression. *J Orthop Res* 19:1140-6, 2001.
28. Lefkoe TP, Trafton PG, Ehrlich MG, Walsh WR, Dennehy DT, Barrach HJ, Akelman E: An experimental model of femoral condylar defect leading to osteoarthritis. *J Orthop Trauma* 7:458-67, 1993.
29. Lipshitz H, Glimcher MJ: In vitro studies of the wear of articular cartilage. II. characteristics of the wear of articular cartilage when worn against stainless steel plates having characterized surfaces. *Wear* 52:297-339, 1979.
30. Loening A, Levenston M, James I, Nuttal M, Hung H, Gowen M, Grodzinsky A, Lark M: Injurious mechanical compression of bovine articular cartilage induces chondrocyte apoptosis. *Arch Biochem Biophys* 381:205-12, 2000.
31. McKinley TO, McKinley T, Rudert MJ, Koos DC, Pedersen DR, Baer TE, Tochigi Y, Brown TD: Stance-phase aggregate contact stress and contact stress gradient changes resulting from articular surface stepoffs in human cadaveric ankles. *Osteoarthritis Cartilage*, 2005.
32. McKinley TO, Rudert MJ, Koos DC, Pedersen DR, Baer TE, Tochigi Y, Brown TD: Contact stress transients during functional loading of ankle stepoff incongruities. *J Biomech*, 2005.
33. Mow VC, Kuei SC, Lai WM, Armstrong CG: Biphasic creep and stress relaxation of articular cartilage in compression: theory and experiment. *J Biomech Eng* 102:73-84, 1980.
34. Patwari P, Gaschen V, James IE, Berger E, Blake SM, Lark MW, Grodzinsky AJ, Hunziker EB: Ultrastructural quantification of cell death after injurious compression of bovine calf articular cartilage. *Osteoarthritis Cartilage* 12:245-52, 2004.
35. Pena E, Calvo B, Martinez MA, Doblare M: Effect of the size and location of osteochondral defects in degenerative arthritis. A finite element simulation. *Comput Biol Med* 37:376-87, 2007.
36. Quinn TM, Allen RG, Schalet BJ, Perumbuli P, Hunziker EB: Matrix and cell injury due to sub-impact loading of adult bovine articular cartilage explants: effects of strain rate and peak stress. *J Orthop Res* 19:242-9, 2001.
37. Radin EL, Burr DB, Caterson B, Fyhrie D, Brown TD, Boyd RD: Mechanical determinants of osteoarthritis. *Sem Arthritis Rheum* 21:12-21, 1991.
38. Rudd RG, Visco DM, Kincaid SA, Cantwell HD: The effects of beveling the margins of articular cartilage defects in immature dogs. *Vet Surg* 16:378-83, 1987.

39. Schinagl RM, Gurskis D, Chen AC, Sah RL: Depth-dependent confined compression modulus of full-thickness bovine articular cartilage. *J Orthop Res* 15:499-506, 1997.
40. Schinagl RM, Ting MK, Price JH, Sah RL: Video microscopy to quantitate the inhomogeneous equilibrium strain within articular cartilage during confined compression. *Ann Biomed Eng* 24:500-12, 1996.
41. Thibault M, Poole AR, Buschmann MD: Cyclic compression of cartilage/bone explants in vitro leads to physical weakening, mechanical breakdown of collagen and release of matrix fragments. *J Orthop Res* 20:1265-73, 2002.
42. Wang CC, Deng JM, Ateshian GA, Hung CT: An automated approach for direct measurement of two-dimensional strain distributions within articular cartilage under unconfined compression. *J Biomech Eng* 124:557-67, 2002.
43. Wang Y, Ding C, Wluka AE, Davis S, Ebeling PR, Jones G, Cicuttini FM: Factors affecting progression of knee cartilage defects in normal subjects over 2 years. *Rheumatology (Oxford)* 45:79-84, 2006.
44. Weightman B: Tensile fatigue of human articular cartilage. *J Biomech* 9:193-200, 1976.
45. Weightman B, Chappell DJ, Jenkins EA: A second study of tensile fatigue properties of human articular cartilage. *Ann Rheum Dis* 37:58-63, 1978.
46. Wilson W, van Burken C, van Donkelaar C, Buma P, van Rietbergen B, Huiskes R: Causes of mechanically induced collagen damage in articular cartilage. *J Orthop Res* 24:220-8, 2006.
47. Wluka AE, Ding C, Jones G, Cicuttini FM: The clinical correlates of articular cartilage defects in symptomatic knee osteoarthritis: a prospective study. *Rheumatology (Oxford)* 44:1311-6, 2005.

CHAPTER 3

EXPERIMENTAL MEASUREMENT AND QUANTIFICATION OF FRICTIONAL CONTACT BETWEEN BIOLOGICAL SURFACES EXPERIENCING LARGE DEFORMATION AND SLIP

3.1 Abstract

The internal stress and strain states of tissues are known to play significant roles in physiological and pathological processes. However, the biomechanical interactions between tissue surfaces have received less attention. Theoretical models have described some special cases of contact, with simplifying assumptions about material properties, surface geometries, and loading conditions. The ability to experimentally track and quantify the surface interactions between contacting biological tissues would directly contribute to the understanding of contact and also help to validate theoretical analyses. The objectives of this study were to 1) develop a general mathematical approach describing the dynamics of deformation and relative surface motion between contacting bodies and 2) apply this approach to experimental data to describe the contact mechanics between opposing articular cartilage surfaces

with differing mechanical properties. The theoretical formulation describes contact and deformations from the displacement of discrete tissue markers on each surface, and is applicable to 2-D or 3-D datasets. The method was validated using a theoretically generated 3-D dataset designed to recreate many possible complications of experimental data, including 1) motion in three dimensions, with components tangential and normal to the surface, 2) finite surface deformations, 3) temporally and spatially varying surface orientations, and 4) surfaces entering and leaving contact; varying model parameters greatly altered the magnitudes of error, but errors were below 1% for many possible scenarios. Experimentally, fluorescently stained nuclei were automatically tracked through a dynamic image sequence by iteratively maximizing correlation between frames; the displacements of the nuclei were used to quantify tissue movement and deformation. The grossly softer surface experienced nearly twice the total strain and significant lateral expansion, producing sliding between the surfaces.

3.2 Introduction

Biomechanics play a crucial role in the normal function of the human body. It has been well documented that stresses and strains arising in tissues can influence cellular responses [14, 17] and contribute to processes such as growth, maturation, adaptation [14, 26], injury [36], and repair [16, 37]. However, tissues and organs often contact at surfaces, and the biomechanical interactions occurring at these surfaces may have significant implications to both normal and pathological processes. Recent studies have implicated the shearing of cartilage due to the articulation of joints to have dramatic effects on cellular response, and lubricant secretion in particular [33, 34]. Similar interactions can be observed throughout the body (e.g. eye lid sliding against the cornea [32], heart sliding in the pericardial sac, lungs sliding against the peritoneal cavity [29]). To fully understand the role that mechanics play in physiological function, it is important to study both the internal mechanical states of tissues and the interactions occurring between them.

Theoretical analyses of contact mechanics have been developed to predict the deformations and sliding in a variety of specific conditions. The topic of contact mechanics was approached by Heinrich Hertz in 1882 to describe the normal, frictionless contact between non-conforming, perfectly elastic bodies. Since then, much of the work in the field has focused on eliminating one or more of the assumptions made in the classical Hertzian solution and extending the applicability to more practical problems, including inhomogeneous or anisotropic materials, large deformations, and frictional contact [25]. In recent years, advancements in the field of

contact mechanics have been driven by the formulation of robust finite element approaches and increased computing power, allowing consideration of problems lacking closed-form solutions. Models have been developed for a variety of physiological [20], and even patient-specific [11], geometries, and more accurate boundary conditions have been prescribed by real-time tracking of movement in human subjects [11]. The use of these models provides analysis of joint kinematics, and predictions of stress and strain distributions in the opposing cartilage surfaces. However, these models still incorporate assumptions that may be difficult to validate, including the material constitutive equations and friction definitions. In biological tissues, the complex nature of the materials (e.g. cartilage, which is viscoelastic, anisotropic, and inhomogeneous) and their surfaces (which may include multiple modes of lubrication) [13] may make it difficult to fully predict the contact behaviors. With continued improvements in imaging and image processing, it may be possible to experimentally supplement and validate theoretical predictions of contact.

Previous experiments have approached the issue of tracking tissue kinematics, deformation, and loading at a variety of length-scales. Video dimensional analysis [23] and biplane cineradiography [31] have each been used to visualize displacement fields in tissues. In the heart, biplane cineradiography has been used to measure muscle strains [18, 30], using embedded surface markers. More recently MRI has been employed to image heart contractions, measuring changes in wall thickness and chamber volume [8]. Similar studies have been performed during joint articulation, to monitor changes in cartilage thickness [10], and joint kinematics [12]. *In vitro* studies have microscopically imaged spatial variations in articular cartilage intra-tissue strain

($\sim 10 \mu\text{m}$ resolution) under static or quasi-static compressive loading [38, 39, 41], and similar techniques were used to quantify the deformation of single cells [15]. However, to our knowledge, experimental investigations of the local deformations and surface interactions arising between dynamically contacting bodies have not been performed.

Several theoretical studies have attempted to predict the contact mechanics of articular cartilage surfaces. Many studies have modeled cartilage as an elastic solid, but such assumptions obscure the time-dependent viscoelastic response of the tissue and may not be suitable for dynamic analyses [1, 2, 6]. Other studies have incorporated the biphasic model of cartilage into solutions of cartilage contact. Hou et al developed boundary conditions relevant for the interface of a viscous fluid and a biphasic medium [21] and implemented them [22] in a numerical solution of dynamic contact between a rigid indenter and a cartilage surface separated by a thin fluid film. Those boundary conditions were then adapted to determine an asymptotic solution of the frictionless contact between two linearly elastic, biphasic cartilage layers [4]. More recently, finite element models have incorporated the biphasic and transversely isotropic properties of cartilage to study contact between cartilage layers with varying curvature [9]. These various solutions have provided some important insights and show agreement with certain cartilage behaviors (e.g. failure at the subchondral bone interface [2, 3]), but contain simplifications including sample geometries, material properties, or the assumption frictionless contact [1, 3, 6, 19], which may affect the accuracy of predictions under certain circumstances. Also, none of the models have attempted to quantify the local sliding between contacting cartilage surfaces.

Experimental quantification of cartilage contact could help to validate and refine the assumptions used in current theoretical models.

Thus, the objectives of this study were to 1) develop a general mathematical approach to quantify dynamic deformation and local surface interactions (i.e. sliding velocity and total sliding distance) between experimentally-tracked contacting bodies and 2) implement this approach to describe the contact mechanics between opposing articular cartilage surfaces. First, a mathematical approach that is applicable to both 2-D and 3-D datasets will be presented, and these methods will be validated using theoretically-generated 3-D datasets. Then, previous studies of intra-tissue cartilage strain will be extended to investigate contact between opposing cartilage surfaces under dynamic loading, and tissue displacements will be automatically tracked using digital image correlation techniques. Tissue deformation and surface interactions will then be quantified using the presented approach.

3.3 Methods

Theoretical Predictions of Contact

We will first present a brief review of the basic concepts included in continuum formulations developed for large deformation frictional contact [28, 35, 40]. Then, analogous formulations will be introduced for use with discrete, spatially and temporally sampled, experimental data. Continuum and discretized finite element approaches to large deformation frictional contact problems often follow the same general approach. Forces or displacements are applied to two independent bodies

which move relative to each other and interact over some portion of their surfaces. Contact solutions seek to describe the deformations of the individual sides and the resulting position of each point in the bodies. This is achieved by solving the independent motion of each body over a short time-step and then analyzing the contact conditions. If the independent movements result in overlap of the two surfaces, the deformations that would eliminate the overlap can be determined. Constitutive laws are then used to derive the tractions arising from surface deformations, while defined frictional laws determine the slip behavior and frictional forces. Solutions are calculated through minimization of error terms by adjusting the deformation and slipping between surfaces to achieve an equilibrium condition. This procedure is then repeated over subsequent time-steps.

Description of when surfaces are in contact, the surface area that participates in this contact, and the sliding that occurs between them requires knowledge of both the surface movements and of their positions in relation to one another. For an idealized case, where two surfaces are assumed to remain in contact and overlap does not occur, the instantaneous rate of sliding at any contact point will be equal to the difference in velocities of the two surfaces at that point. In general, the relative velocity of contacting surfaces may have components both tangent and normal to the surface plane. The component of relative velocity in the direction normal to the plane is typically called the gap velocity, and determines whether surfaces are coming into, or out of, contact. The component of the velocity tangent to the surface is then referred to as the sliding velocity. To account for the independent velocities of points on the two surfaces, solution of these problems requires the use of a reference frame describing

the movement of one body with respect to the other body; this has been accomplished by description of a body's motion as a convective velocity [28] of the other surface or by using mixed Lagrangian-Eulerian [7] approaches. For the purposes of predicting long-term wear, it may be advantageous to quantify the total sliding distance over a point, or an entire surface, during a finite time period, values that can be obtained by integrating the sliding velocity over time or the surface, respectively.

Discrete Analysis of Experimentally-Tracked Contact

The time-dependent positions of experimentally-tracked mesh-points are used for all calculations of displacement, displacement gradient, strain, and surface interactions. Unlike theoretical predictions of contact mechanics, where the deformation of contacting bodies and the interaction between their surfaces are related by constitutive equations and must be solved for simultaneously, analysis of experimentally-derived data allows decoupling of deformation and sliding calculations. Therefore, the current approach is presented in two parts: 1) analysis of the internal deformations of each body, individually and 2) calculation of the interactions between the body surfaces.

Intra-tissue Strain Equations

The initial position of each point in the body is given by \mathbf{a} , and the corresponding positions at all subsequent times in the deformed state, by $\mathbf{x} = f(\mathbf{a}, t)$. Deformation of each body is calculated individually (without consideration of the opposing surface) by calculation of the displacements of each point, $\mathbf{u} = \mathbf{x} - \mathbf{a}$, and displacement gradients in the three (or two, for 2-D analyses) orthogonal directions. For the discretely sampled data, with points equally spaced at

$$h = (a_j)_m - (a_j)_{m-1} = (a_j)_{m+1} - (a_j)_m = \dots \quad (1)$$

the displacement gradients can be calculated at each mesh-point using 2nd (edges) or 4th (interior) order finite difference calculations.

4th order central (used for all interior points):

$$\left(\frac{du_i}{dx_j} \right)_m = \frac{(u_i)_{m-2} - 8(u_i)_{m-1} + 8(u_i)_{m+1} - (u_i)_{m+2}}{12h} \quad (2)$$

2nd order central (used at positions adjacent to edge):

$$\left(\frac{du_i}{dx_j} \right)_m = \frac{(u_i)_{m+1} - (u_i)_{m-1}}{2h} \quad (3)$$

2nd order forward (used at the starting edge):

$$\left(\frac{du_i}{dx_j} \right)_m = \frac{-3(u_i)_m + 4(u_i)_{m+1} - 1(u_i)_{m+2}}{2h} \quad (4)$$

2nd order backward (used at the ending edge):

$$\left(\frac{du_i}{dx_j} \right)_m = \frac{1(u_i)_{m-2} - 4(u_i)_{m-1} + 3(u_i)_m}{2h} \quad (5)$$

Lagrangian strains can then be calculated from the displacement gradients (equation written with no summation).

$$(E_{ij})_m = \frac{1}{2} \left\{ \left(\frac{du_i}{dx_j} \right)_m + \left(\frac{du_j}{dx_i} \right)_m + \left(\frac{du_i}{dx_i} \right)_m \left(\frac{du_i}{dx_j} \right)_m + \left(\frac{du_j}{dx_i} \right)_m \left(\frac{du_j}{dx_j} \right)_m \right\} \quad (6)$$

Surface Interactions

Analysis of surface interactions requires consideration of only those points lying at (or in the absence of points directly at the surface, closest to) the surface. Since the two surfaces are allowed to move independently, the kinematics of points on each surface must be considered simultaneously to determine their interactions.

Analysis of surface interactions (Figure 3.1) will be performed by describing motion in reference to one surface, often referred to as a slave surface [11], or contactor [35]. For each point on the slave surface, the length of the opposing surface (called the master surface [11], or target [35]) that slides over it during each time-step will be determined. As has been noted for finite element analyses of contact, sliding velocities calculated from discrete data, unlike those in the continuous case, may depend on the choice of reference side. This complication arises because changes in surface velocity, orientation, and deformation that may occur within a single time-step could affect the lengths of the contacting surfaces and the directions of relative motion; refinements in the mesh or time-step lengths will more closely approximate the continuous case.

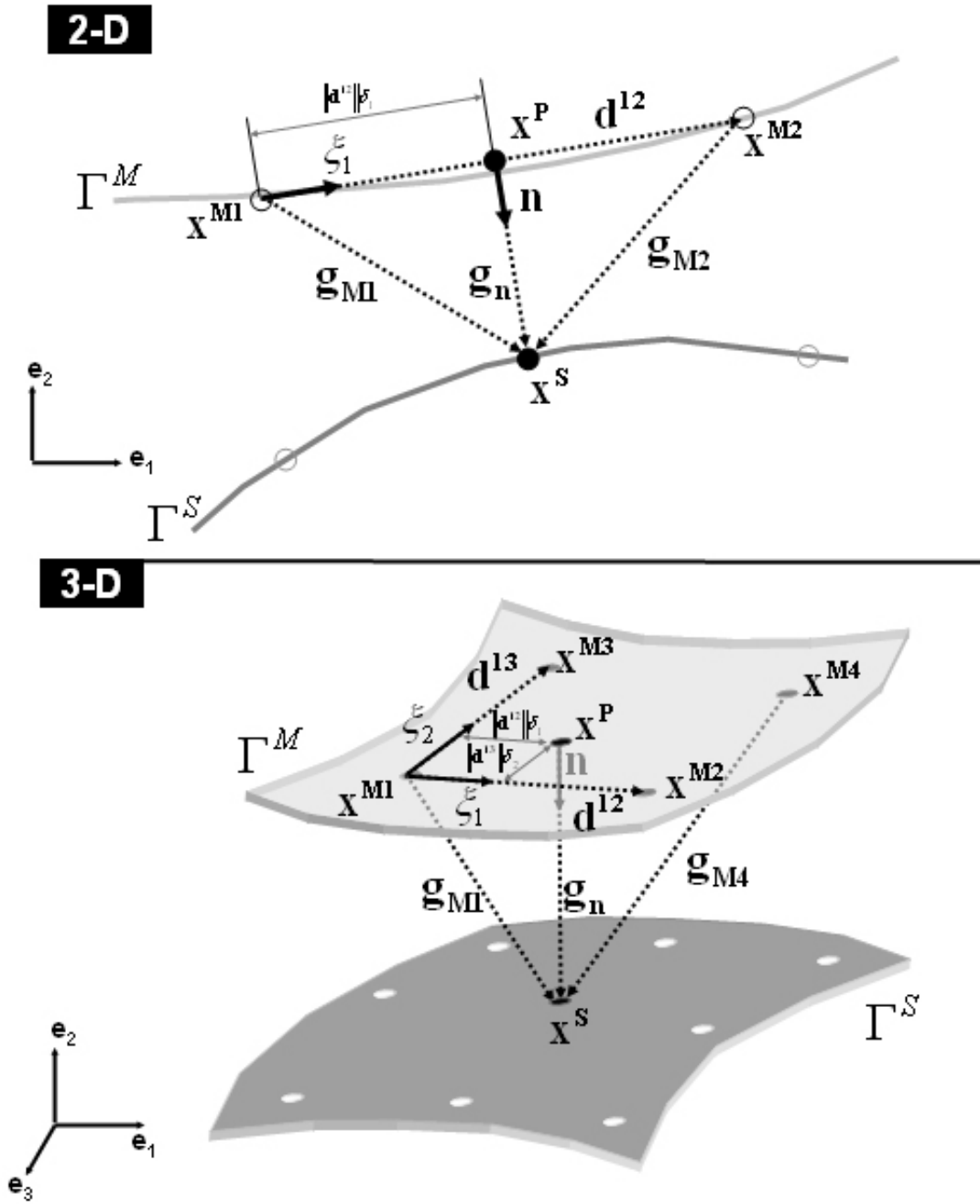


Figure 3.1: Diagram of contact definitions in 2 and 3 dimensions.

The position, orientation, and movement of the master surface will be described with respect to each point on the slave surface. At each time-point, the first step will be determining the projection, \mathbf{x}^p , of the slave point onto the master surface. The four mesh-points on the master surface that surround the projection of the reference slave point (\mathbf{x}^{M1} , \mathbf{x}^{M2} , \mathbf{x}^{M3} , and \mathbf{x}^{M4} ; ordered from closest to furthest from the slave point) will be determined. Four vectors are defined describing the relative positions of the slave point and master points: \mathbf{g}_{M1} (equal to $\mathbf{x}^s - \mathbf{x}^{M1}$), \mathbf{d}^{12} ($\mathbf{x}^{M2} - \mathbf{x}^{M1}$), \mathbf{d}^{13} ($\mathbf{x}^{M3} - \mathbf{x}^{M1}$), and \mathbf{g}_{M4} ($\mathbf{x}^s - \mathbf{x}^{M4}$). The unit vectors ξ_1 and ξ_2 are then defined in the directions of \mathbf{d}^{12} and \mathbf{d}^{13} , respectively, representing the local coordinate axes of the contacting, master surface sub-region. The position of \mathbf{x}^p within the sub-region (with respect to \mathbf{x}^{M1}) is obtained from the equations:

$$\delta_1 = (\mathbf{g}_{M1} \cdot \xi_1) / \|\mathbf{d}^{12}\|, \quad \delta_2 = \mathbf{g}_{M1} \cdot \xi_2 / \|\mathbf{d}^{13}\| \quad (7)$$

$$\mathbf{x}^p = \delta_1 \|\mathbf{d}^{12}\| \xi_1 + \delta_2 \|\mathbf{d}^{13}\| \xi_2 \quad (8)$$

The displacement of \mathbf{x}^p over a time-step can be determined by bilinear interpolation of the incremental displacements of the four surrounding master points.

$$\Delta \mathbf{u}^p = (1 - \delta_1)(1 - \delta_2) \Delta \mathbf{u}^{M1} + \delta_1(1 - \delta_2) \Delta \mathbf{u}^{M2} + (1 - \delta_1)\delta_2 \Delta \mathbf{u}^{M3} + \delta_1\delta_2 \Delta \mathbf{u}^{M4} \quad (9)$$

Analogous variables may be derived for the 2-D case. The projection of the slave point onto the master surface falls along a line segment connecting \mathbf{x}^{M1} and \mathbf{x}^{M2} , the closest and second closest points on the master surface. The vectors connecting these points to the slave point and each other are defined as \mathbf{g}_{M1} ($\mathbf{x}^s - \mathbf{x}^{M1}$), \mathbf{g}_{M2}

$(\mathbf{x}^S - \mathbf{x}^{M2})$, and the surface tangent $\mathbf{d}^{12}(\mathbf{x}^{M2} - \mathbf{x}^{M1})$. As before, the unit tangent, ξ_1 , is defined in the direction of \mathbf{d}^{12} , and the location of the projected point on the segment, with respect to \mathbf{x}^{M1} , is given by:

$$\delta_1 = (\mathbf{g}_{M1} \bullet \xi_1) / \|\mathbf{d}^{12}\| \quad (10)$$

$$\mathbf{x}^P = \delta_1 \|\mathbf{d}^{12}\| \xi_1 \quad (11)$$

The displacement of \mathbf{x}^P over a time-step is then determined by linear interpolation of the incremental displacements of the two bounding points.

$$\Delta \mathbf{u}^P = (1 - \delta_1) \Delta \mathbf{u}^{M1} + \delta_1 \Delta \mathbf{u}^{M2} \quad (12)$$

Since, the location of the projected point on the master surface changes during a single time-step, Δt , (if sliding is present) it would be possible to define the displacement of the contacting surface as the displacement of either 1) the point that begins in contact with the slave point, $\mathbf{x}^P(t-1)$, or 2) the point that ends in contact with the slave point, $\mathbf{x}^P(t)$. Therefore, displacement of the contacting master surface over a single time-step will be calculated by averaging the displacements of those two points. The relative displacement of the master surface with respect to the slave point, in turn, is calculated by subtracting this average value from the displacement of the slave point over that same time-step, and the relative velocity is calculated, by dividing that value by the time-step length. These calculations are the same for 2-D or 3-D geometries.

$$\Delta \mathbf{U} = (\Delta \mathbf{u}^P(t - \Delta t) + \Delta \mathbf{u}^P(t)) / 2 - \Delta \mathbf{u}^S \quad (13)$$

$$\mathbf{V} = \Delta \mathbf{U} / \Delta t \quad (14)$$

Definition of Contact

The gap distance between the slave point and its projection on the master surface can be used to describe whether two surfaces are in contact at that point. This distance is obtained by taking the dot product of \mathbf{g}_{M1} and the unit normal to the master surface, defined by the cross product of the two tangent vectors.

$$\mathbf{n} = |\xi_1 \times \xi_2| * \text{sign}_n \quad (15)$$

$$\text{sign}_n = \begin{cases} +, & \text{if } |\xi_1 \times \xi_2| \bullet \mathbf{g}_{M1} \geq 0 \\ -, & \text{if } |\xi_1 \times \xi_2| \bullet \mathbf{g}_{M1} < 0 \end{cases} \quad (16)$$

$$\mathbf{g}_n = (\mathbf{n} \bullet \mathbf{g}_{M1}) \mathbf{n} \quad (17)$$

In theoretical discussions, contact is generally defined as a gap distance equal to zero [11],[35]. In those cases, negative magnitudes, representing overlap of contacting sides, are prohibited. However, when dealing with experimental data where the outermost tracked points lie slightly below the surface, it may be necessary to alter the definition of what constitutes contact. In that case, contact would occur when the gap distance falls below a prescribed threshold, D_{contact} (roughly equal to twice the distance from the outermost points to the overlying surface); negative gap distances would still be impossible, but distances lower than the contact threshold would be allowed and signal compression of the surface-most tissue layers. In the current approach, surfaces were defined as contacting when the following three relations held true:

$$\|\mathbf{g}_n\| < D_{\text{contact}} \quad (18)$$

and for the 3-D case:

$$\|\mathbf{g}_{M1}\| < \sqrt{\|\mathbf{g}_n\|^2 + 0.5h^2} \quad (19)$$

$$\|\mathbf{g}_{M4}\| < \sqrt{\|\mathbf{g}_n\|^2 + 2h^2} \quad (20)$$

or for the 2-D case:

$$\|\mathbf{g}_{M1}\| < \sqrt{\|\mathbf{g}_n\|^2 + 0.25h^2} \quad (21)$$

$$\|\mathbf{g}_{M2}\| < \sqrt{\|\mathbf{g}_n\|^2 + h^2} \quad (22)$$

The first criterion sets the threshold for normal gap distance, while the second and third criteria set a limit on the distance to the closest and furthest of the four points on the master surface, to assure that the normal vector projects onto the slave surface.

The relative displacement of the two surfaces can be divided into components tangent and normal to the master surface. An average unit normal will be determined for each time-step and used to define in- and out- of-plane motion.

$$\mathbf{n}_{avg} = (\mathbf{n}(t - \Delta t) + \mathbf{n}(t)) / \|\mathbf{n}(t - \Delta t) + \mathbf{n}(t)\| \quad (23)$$

The gap displacement is oriented in the direction of the average unit normal vector, and its magnitude is determined by taking the dot product of the relative displacement with the average unit normal vector. The gap velocity is then determined by dividing by the time-step length.

$$\Delta \mathbf{g}_n = (\Delta \mathbf{U} \cdot \mathbf{n}_{avg}) \mathbf{n}_{avg} \quad (24)$$

$$\dot{\mathbf{g}}_n = \Delta \mathbf{g}_n / \Delta t \quad (25)$$

The sliding displacement during an individual time-step may then be calculated by subtracting the gap displacement from the relative displacement.

$$\Delta \mathbf{S} = \Delta \mathbf{U} - \Delta \mathbf{g}_n \quad (26)$$

$$\dot{\mathbf{S}} = \mathbf{S} / \Delta t \quad (27)$$

The sliding distance is equal to the magnitude of the sliding displacement; sliding velocity and rate are obtained by dividing sliding displacement and distance, respectively, by the time-step interval. Summing the sliding distance over each time-step would give the total sliding distance traveled by a single slave point. Sliding rates or distances may be numerically integrated over the slave surface to provide measures of sliding for an entire surface. As mentioned previously, magnitudes of the sliding rate and distance at a specific contact point can vary depending on the choice of reference side, but integrating these quantities over the entire contact surface should eliminate this dependence.

Validation of Deformation and Sliding Calculations

A theoretically-generated, 3-D dataset was used to validate the equations introduced in the preceding section. The geometry and kinematics were chosen to account for many of the potential pitfalls of experimental data, but still permit the calculation of the exact interactions needed for verification. This was accomplished by considering the contact between a semi-infinite cylindrical rod and an elastic band wrapped partially around its circumference (Figure 3.2); the desired surface interactions were created through superposition of several simple translations, rotations, and deformations. Axial and radial velocities were applied to the rod, resulting in rotation about its long axis and translation in the axial direction, and uniform expansion of the rod was applied in the radial direction. At the same time, the band remained fixed at one end, and was uniformly stretched in the circumferentially

around the rod. Although this scenario is relatively trivial to analyze when decomposed, it accounts for many of the complications that may arise in experimental data: 1) motion in three dimensions, with components both tangential and normal to the surface, 2) finite surface deformations, 3) temporally and spatially varying surface orientations, and 4) surfaces entering and leaving contact. Analysis was performed on several scenarios with varying model parameters, and results were compared to the theoretically prescribed velocities.

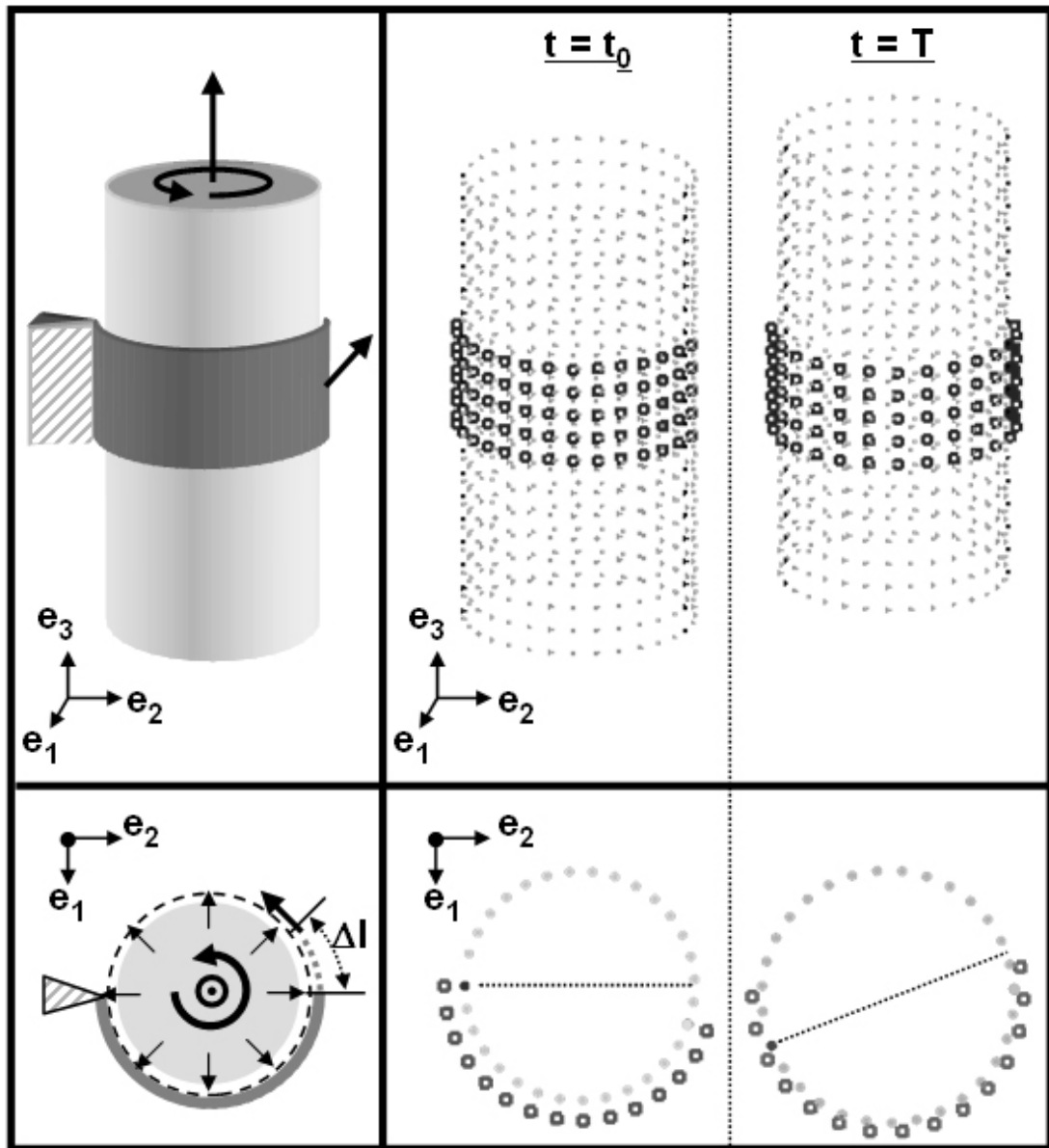


Figure 3.2: Diagram of the theoretical dataset used for validation of 3-D contact definitions. A semi-infinite cylinder is allowed to slide axially, rotate, and expand inside a band that remains fixed at one end and deforms uniformly in the circumferential direction of the cylinder.

Experimental Model of Cartilage Contact

A simple 2-D experiment was performed to demonstrate the utility of the developed formulation. Opposing osteochondral slabs were loaded in uniaxial compression and tissue deformation was tracked using video microscopy (Figure 3.3). Similar techniques have been previously employed to determine intra-tissue strains in single explants of articular cartilage [5, 27, 38, 39]. In this case, simultaneous tracking of markers in both cartilage layers allowed intra-tissue strains for each individual layer and the local sliding between the two surfaces to be quantified. Two experimental groups were investigated. In the first, the two osteochondral blocks were taken from the patellofemoral groove (PFG) and had ~matched mechanical properties. In the other, one osteochondral block was taken from the PFG, while the opposing block was taken from the uncovered tibial plateau (UTP) and was grossly softer. The expectation of the testing was that the mismatched mechanical properties would result in greater axial strain in the tibial block, producing greater lateral expansion and, in turn, sliding between the two surfaces. A detailed description of the methods of mechanical testing and image analysis follows.

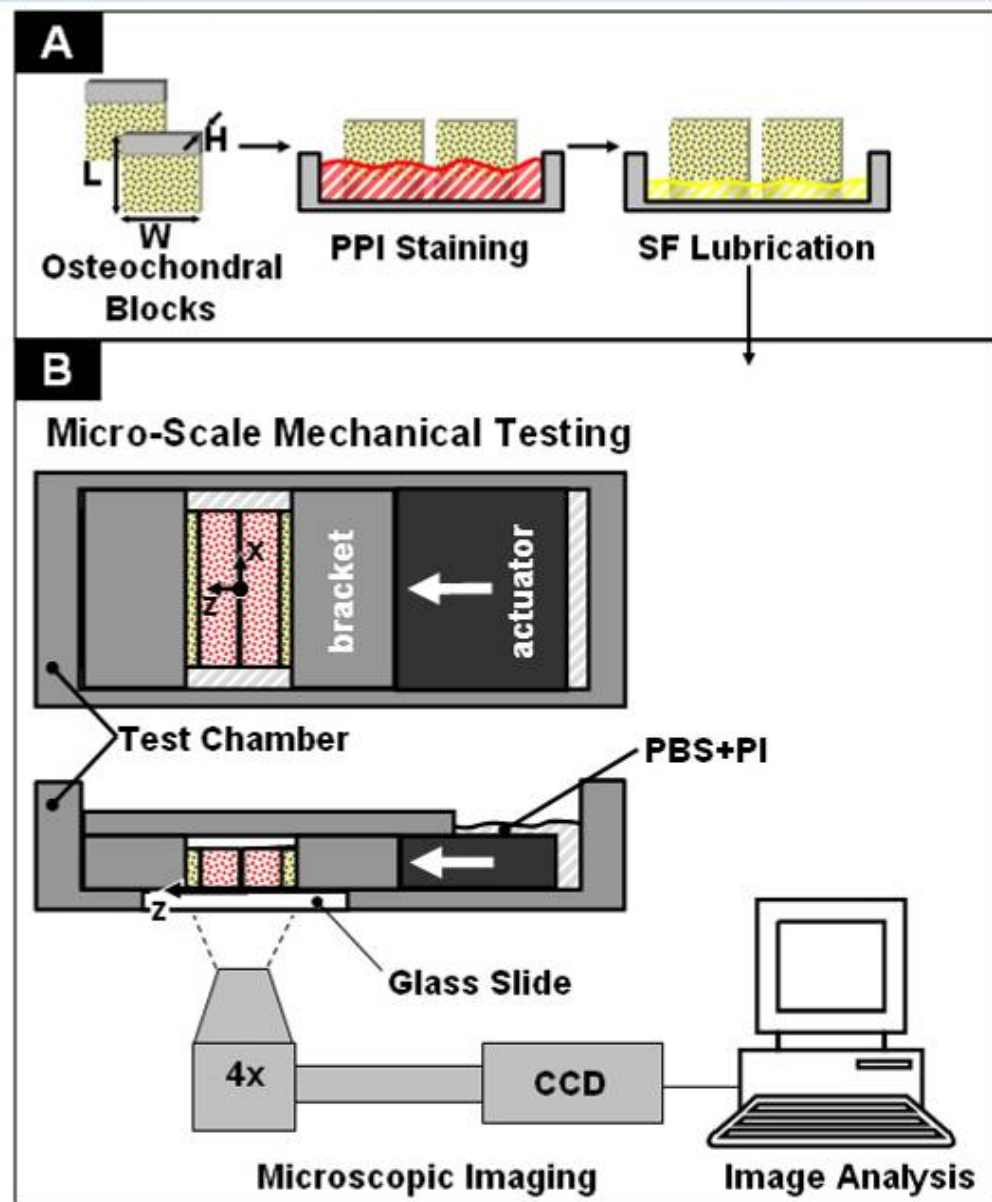


Figure 3.3: Sample preparation (A) and mechanical testing setup (B) of opposing cartilage blocks.

Mechanical testing

Slab pairs were placed in a microscope-mounted test chamber with their cartilage-bone surfaces flush with the glass chamber bottom and their articular surfaces in opposition and aligned perpendicular to the direction of loading (z-axis). Intra-tissue deformation was imaged through the chamber bottom (x-z plane) using a Nikon Diaphot 300 epi-fluorescence microscope fitted with a G-2A filter cube (Nikon, Melville, NY). Samples were imaged at 4x magnification ($\sim 1.8 \times 2.8 \text{ cm}^2$ field of view) and digital images (512x768 pixel resolution) were recorded with a charge-coupled device camera (Model 4913-5000, Cohu, Inc., San Diego, CA). Sample pairs were uniaxially compressed (unconfined) to 15% total tissue strain (defined as the applied displacement divided by the sum of the cartilage thicknesses), at a strain rate of 1%/s ($\sim 25 \text{ um/s}$) using a displacement-controlled actuator (Model MFN25PP, Newport Corporation, Irvine, CA). Digital images were acquired dynamically during loading at 4 frames/s.

Correlative Point Tracking

Fluorescently stained nuclei were used as fiducial markers to track tissue deformation in the digital images. Cell tracking and deformation calculations (described earlier) were performed automatically using a custom code written in MATLAB 6.5 including functions from the Image Processing Toolbox (Mathworks, Inc., Natick, Massachusetts). Briefly, the program consisted of a hybrid of the discrete point tracking [38] and digital image correlation[41] methods that have been previously employed to determine cartilage strain. Translations of cell nuclei, acting as fiducial markers, were tracked automatically through the dynamic image sequence

by maximizing the normalized cross-correlation; positions of nuclei were used to update positions of mesh-points, where displacement gradients and strains were determined by finite difference approximations (as described above). Following analysis of deformation in each side, displacements of mesh-points lying on the two surfaces were used to calculate sliding using the approach described earlier.

Image sequences were imported into Matlab for analysis. First, cell nuclei in the initial, unloaded image were identified by intensity normalizing and segmenting the images using methods similar to those described previously [24]; since segmentation was performed to identify potential markers, and not for quantification of cellularity, it was not vital to identify every nucleus. A region of interest (ROI), where deformations would be calculated, was manually selected in the initial image. Centroids of all segmented nuclei were determined, and an approximately uniformly-spaced ($\sim 50 \mu\text{m}$) subset of these cell nuclei was created by defining a uniform grid in the region of interest and selecting the nearest nucleus to each of these points; the points in this subset were used as the fiducial markers to track deformation through subsequent images.

For each frame, base points were tracked using an iterative correlation process (Figure 3.4). First, the coordinates of the points in the previous frame were used as an approximation of their positions in the current frame. Then, point positions were updated by four successive correlation steps (using modified versions of the Matlab function `cpcorr`) maximizing normalized cross-correlation of equally-sized regions (centered on the marker) between image frames. 1) Positions of the points were coarsely adjusted by selecting a 20×20 pixel region around each point and

maximizing the normalized cross-correlation to an equally-sized region surrounding the point in the previous frame; the use of a relatively large correlation window allowed displacements of up to 20 pixels in each of the two orthogonal directions to be captured. 2) Positions were refined by repeating this correlation process using a 5 x 5 pixel region; positioning of these smaller regions were affected less by sample deformation. 3) The positions of points were further refined by correlation of 10 x 10 pixel regions to regions around the base points in the initial, undeformed image to eliminate accumulation of error through successive frames. 4) Using the newly determined coordinates, the displacements of each point from their initial positions (in the first frame) were calculated. The displacements of the tracked markers were then used to compute theoretically-deformed images. Since different tissue regions deformed in grossly different manners, no single, and still relatively simple, image transform could adequately re-create the deformed state. For this reason, the ROI was divided into 6 equally sized areas ($3 \text{ lateral} \times 2 \text{ depth}$) and the displacements of the points in those regions were used to calculate a bi-quadratic equation describing deformation of the region. The transformation was then applied to the initial image and marker positions, generating a theoretically-deformed image/marker set for that sub-region. The positions of points were adjusted a final time by correlation of 5 x 5 pixel regions to regions around the base points in the theoretically deformed image. As in step 3, this final step attempts to prevent error accumulation by linking the points back to their initial positions, but is meant to handle cases with large deformations that may correlate poorly with the undeformed image. Poorly correlated

points (every correlation step falling below 0.40) were excluded from further calculations.

Automated Surface Tracking

An independent definition of the surface provided a boundary for calculations that was necessary in cases where correlation of the surface-most points was inadequate. Tracking of points directly adjacent to contacting surfaces was often problematic because of the high deformations in the surface regions. However, the larger-scale intensity profile in the axial direction was preserved. The surface was tracked by minimizing the error between these intensity profiles.

In the initial frame, each of the contacting surface contours were defined a by smoothing spline fit to ~ 10 points, manually selected at positions evenly spaced across the sample widths. In each subsequent frame, points (spaced at 25 pixels, $\sim 90 \mu\text{m}$, in the lateral direction) defined by this spline were automatically repositioned to determine the updated surface contour. This was accomplished by defining 100 pixel wide (in the lateral, x-direction) \times length of the image (in the axial, z-direction) rectangular regions, centered in the lateral direction at the surface point that is being updated. A width-averaged intensity is then calculated at each axial (z-) position for the length of the rectangle. This intensity profile was then compared to the profile at the same lateral (x-) position in the subsequent frame and the axial position of the new profile was adjusted to minimize the squared error terms between the intensity profiles and their intensity gradient profiles. This process was repeated for each surface point at each subsequent time-step.

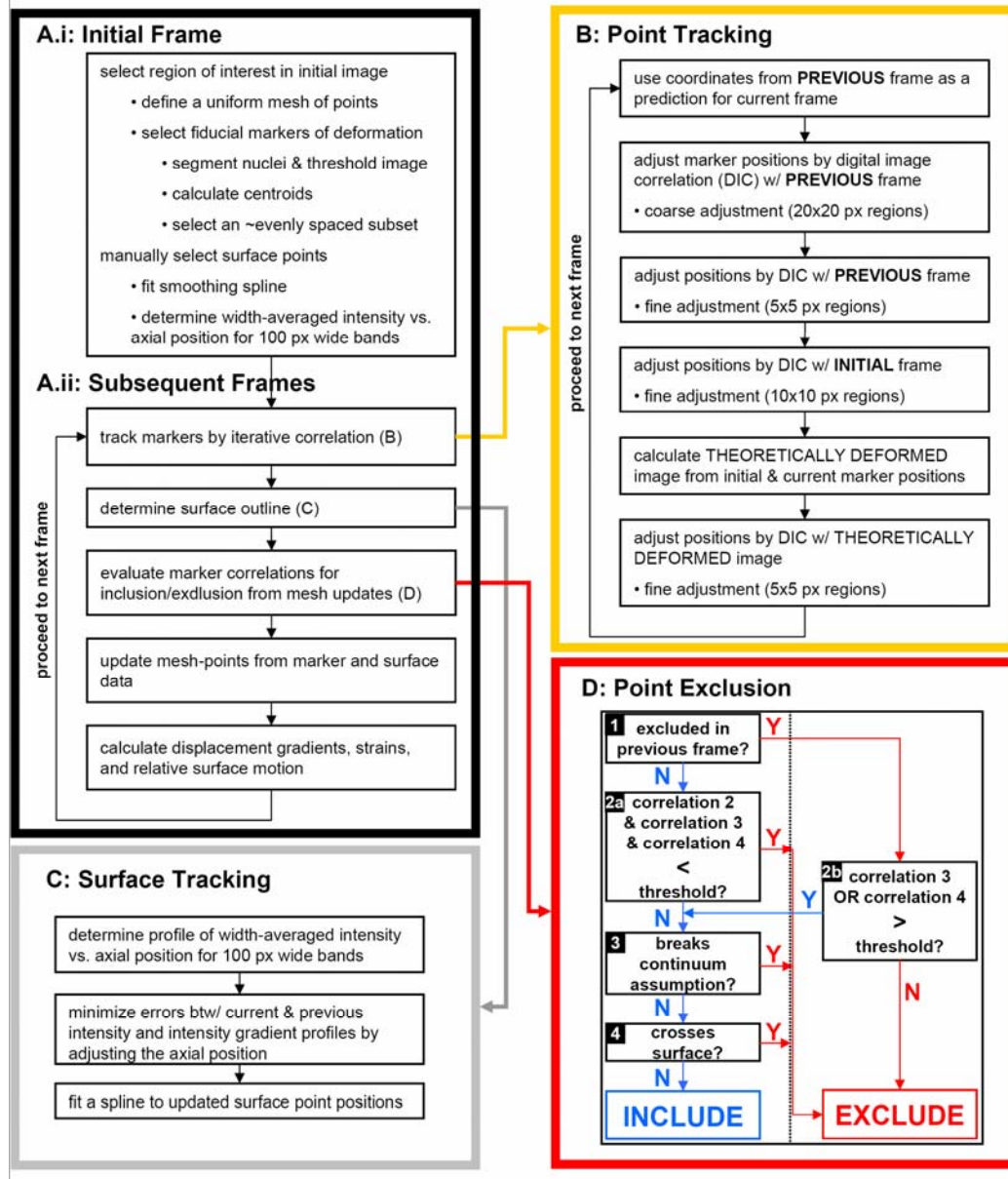


Figure 3.4: Flowchart of image processing routine. A region of interest and bounding surface are manually selected in the initial frame image (A.i). At each subsequent frame (A.ii), fiducial markers (B), and the surface (C) are automatically tracked and areas of low correlation are excluded from further analysis (D). Movement and deformation of the tissue is calculated from the tracked points.

Calculations of Tissue Movement and Deformation

Uniform sets of mesh-points were defined with 27 pixel (100 μm) spacing, in the chosen ROI. The axial (z-) positions of the mesh points lying closest to the surface were calculated from the lateral column positions and the surface spline. The remaining rows of points were defined at 100 μm spacing from the inner-most (into the tissue) surface point.

The deformed position/displacement of each mesh-point not located along the contacting surface was determined from a local affine mapping of the surrounding tracked nuclei (~ 16 nuclei; 200 x 200 μm region), an arrangement that helped limit the affect of small errors in individual point tracking on subsequent strain calculations and allowed poorly correlated points to be excluded from further calculations. For points on the articular surface, the lateral position was calculated using the same affine mapping procedure, and used to calculate the deformed axial position from the updated surface spline. In regions without at least four well-correlated points, positions were updated using the positions of the neighboring mesh-points that had been successfully positioned. Mesh-point displacements were used for all calculations of tissue deformation and sliding using the equations introduced above. To reduce accumulation of noise, displacement data of surface points were smoothed in time and x-position using a moving average filter.

Validation of Point Tracking and Strain Determination

The ability of the image analysis program to accurately track nuclei displacements and calculate intra-tissue strains was assessed by analyzing image sequences generated by applying uniform deformation gradients to a sample image.

Five image sequences were generated to assess the program's ability to handle different types of deformation: 1) rigid body translation at > 10 pixels/frame, 2) rigid body rotation to 20° at 1° /frame, 3) 40% uniaxial extension ($du/dx = 0.4$) at 2%/frame, 4) 40% uniaxial compression ($du/dx = -0.4$) at 2%/frame, 5) 20% simple shear ($dv/dx = 0.2$) at 1%/frame. Each deformation sequence was then analyzed as described above; a ROI (50 x 50 pixels) was chosen in the initial frame and point displacements were used for displacement gradient and strain calculations. Calculated strains (E_{xx} , E_{zz} , and E_{xz}) were checked for consistency with the applied deformations. Errors were calculated as the absolute values of the differences between the calculated strains and the applied strains and are presented as the mean \pm std of errors calculated at each mesh-point within the selected ROI ($5 \times 5 = 25$ mesh-points).

Data Analysis and Statistics

A total of $n=3$ matched and $n=3$ mismatched samples were tested. With $x=0$ defined as the center of the block (5 mm from each edge) in the lateral direction, average sliding was assessed over three surface regions along mismatched samples (center: $x = -250$ to $250 \mu\text{m}$; left: $x = -3.75$ to -3.25 mm; right: $x = 3.25$ to 3.75 mm). Sliding was quantified at the center region ($x = -250$ to $250 \mu\text{m}$) of the matched samples, as a control. For mismatched pairs, average axial and lateral strains were quantified for the superficial $500 \mu\text{m}$ of each surface in the center regions. The effect of sample type on sliding was determined using a t-test comparing the central region of matched and mismatched pairs. The effect of surface location on sliding between mismatched pairs was determined using a one-way ANOVA with a Tukey post-hoc

test. Differences in axial and lateral strain at the surfaces of UTP and PFG blocks in mismatched samples were determined by t-tests. Data are presented as mean \pm SEM.

3.4 Results

Validation of Deformation and Sliding Calculations

Calculations of relative surface velocity and sliding contact in the theoretical dataset corresponded well to the prescribed velocities. Errors were defined as the difference between the prescribed values and the calculated value, normalized to the prescribed value. Best performance was obtained for cases with only an applied axial velocity and surfaces that maintained contact (errors $< 0.00001\%$). In this situation, the orientations of the surface normals do not change over time and the estimate of velocity (displacement/ Δt) is exactly equal to the applied condition.

When a radial component of velocity is added, these estimates may become a significant source of error. At a given radius, error increased with increasing radial velocity; more generally, error was related to the applied angular velocity ($\dot{\theta}$ = radial velocity / radius of curvature), representing the change in orientation being approximated by the average velocity vector. As angular velocity increases, the linear displacement of the point no longer closely approximates the arc traveled by the point during the single time-step. For cases with a radial velocity applied alone (by various combinations of cylinder rotation and band stretching), errors $< 1\%$ for $\dot{\theta} = 0.2$ rad/s, $< 5\%$ for $\dot{\theta} = 0.5$ rad/s, and approached 20% for $\dot{\theta} = 1$ rad/s. Using this relationship, it is possible to determine the maximum acceptable time-step length for surfaces with a given curvature and expected relative velocities.

In general, choice of reference side had little effect on the accuracy of the calculations, except in relation to defining contact. In the cases examined with gap velocity equal to zero, band points remained in contact, but points on the cylinder entered and left contact. Errors for points on the cylinder remaining in contact were equivalent to those for points on the band. Differences between calculated and expected values of sliding for points entering or leaving contact were relatively consistent at 10-20% of the mesh-point spacing, resulting in lower errors for higher prescribed velocities. Similar behavior was seen with contact transitions caused by a finite gap velocity (cylinder expansion), and were independent of the gap velocity. Accordingly, % errors were higher for lower gap velocities. Depending on surface curvature and point spacing, choice of reference side may also be important in defining the onset of contact, due to a slight underestimate of gap distance in concave master surfaces (and overestimate of convex master surfaces). While this could result in large differences in sliding distance calculations in certain circumstances, this difference may not be physically significant because sliding that is erroneously discounted would take place at low contact stresses.

Validation of Point Tracking and Strain Determination

Validation experiments showed acceptably low error values for all tested forms of image deformation. In most cases, the errors did not exceed 0.005 ± 0.005 . The highest error was seen for E_{xx} in the 40% compression case (0.012 ± 0.007). For non-rigid body transformations, lower deformations generally resulted in lower errors. For all transformations, increasing spacing between grid-points resulted in lower magnitudes of error, but reduced the spatial resolution of strain measurements.

Experimental Compression of Opposing Osteochondral Blocks

Qualitatively, sliding occurred between the surfaces of both matched and mismatched samples during compression, but in distinctive manners. In matched samples, the direction of sliding tended to be the same across the entire surface and appeared to be related to the surface curvatures of the particular blocks. For mismatched samples, the softer UTP surface experienced grossly greater lateral expansion, concomitant with sliding toward the block edges with respect to the PFG surface, especially in regions away from the center axis of contact.

The differences in contact mechanics for matched and mismatched samples were apparent in quantitative deformation and sliding measures. For the matched samples, lateral strains (Figure 5A.i) in matched samples were similar for both surfaces and varied relatively little throughout the tissue depth analyzed; the axial strains (Figure 5B.i) near the surface were similar between the two contacting surfaces and decreased markedly with tissue depth. In contrast, for the mismatched samples, the UTP surface experienced greater lateral expansion than the PFG surface ($p < 0.05$, Figure 5A.ii) and also higher peak axial strains ($p < 0.05$; Figure 5B.ii). Sliding between the surfaces was consistent with the extent of differences in the lateral strain of the surfaces. In the center regions of mismatched samples, surfaces averaged ~ 110 μm of sliding, more than double that experienced along the same region of matched samples ($p < 0.05$). Sliding magnitudes varied significantly with lateral position along the surfaces of mismatched samples ($p < 0.05$). Sliding was increased in left and right regions (-3.5mm and $+3.5\text{ mm}$ from the center) when compared to the center region ($p < 0.05$), with magnitudes exceeding $200\text{ }\mu\text{m}$.

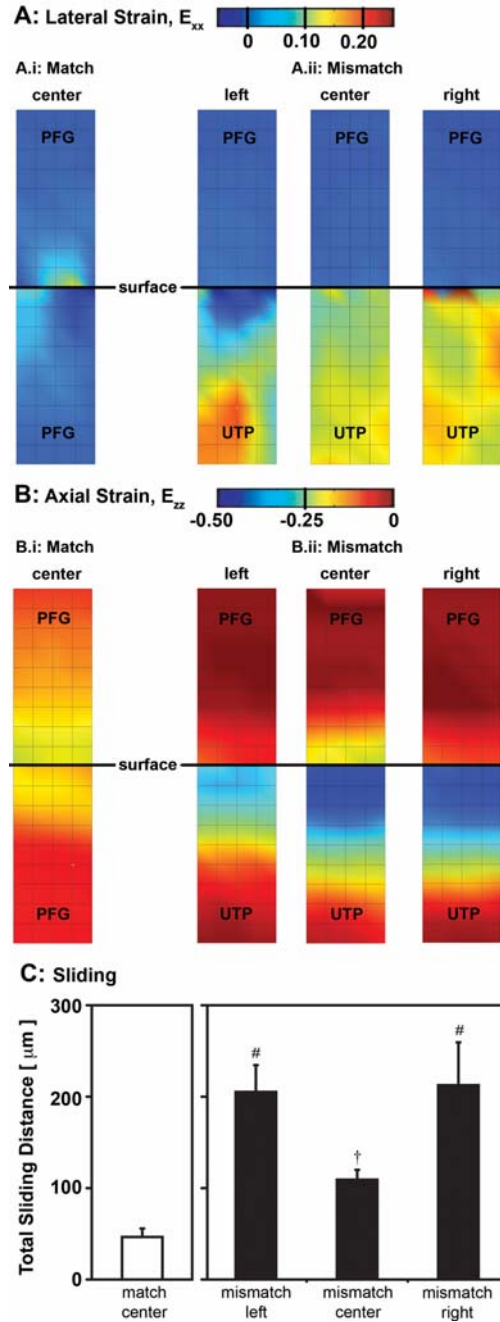


Figure 3.5: Deformation and sliding between cartilage surfaces with matched (PFG-PFG) or mismatched (PFG-UTP) mechanical properties. Composite contour maps show average lateral (A) and axial (B) strains in $400 \times 900 \mu\text{m}^2$ (lateral distance \times tissue depth; box = $100 \mu\text{m}$) tissue regions at the lateral center of matched samples (A.i, B.i) and at the center and near the edges of mismatched (A.ii, B.ii) samples. Total sliding distances between the surfaces at those same locations along matched and mismatched samples are also shown (C). $n=3$. (# $p < 0.05$ compared to center match; † $p < 0.05$ compared to center mismatch).

3.5 Discussion

This paper has described a mathematical formulation to be used with experimental measurements to characterize the deformation and surface interactions between two deformable bodies. The developed approach has the ability to handle dynamic interactions of complex geometries, moving in 2 or 3 dimensions. The formulation was first validated using a series of theoretically-generated datasets. It was then used to analyze an experimental dataset of 2-D cartilage contact. The approach is compatible with a variety of experimental techniques, with calculations based on the tracked movement of tissue. The reduction of experimental measurements using the methods described could be applicable broadly to surfaces and contribute to an improved understanding of contacting tissue surfaces.

The accuracy of the contact description will depend on the specific experimental setup and choices of parameters in both data collection and analysis. The spatial and temporal sampling of any imaging technique must be fine enough so that assumptions of the calculations hold true, including that 1) linear displacements of points over a single time-step are a good estimate of their actual path and 2) variations in strain between mesh-points are \sim linear. Choices of mesh spacing and sampling rate should be determined by weighing the resolution necessary to sufficiently describe the material behavior against the computational cost, and may also be limited by the choice of experimental methods. Ideally, experimental parameters would be adjusted to avoid scenarios with high expected errors; for instance, if contact is expected to occur along a path with high curvature, it may be necessary to increase the temporal

sampling rate. Choices in data analysis could also be used to maximize the accuracy of the results. Since one of the larger sources of error comes from slave points that enter or leave contact with the master surface, the slave surface should be chosen that minimizes that occurrence (the band in the current 3-D example), unless there is a specific experimental interest in the other surface (e.g. a certain side exhibits greater wear or physiological response not seen by the opposing side).

Under an arbitrary load, macroscopic sliding or a mixture of sliding and rolling may occur between contacting surfaces. However, even in the absence of macroscopic displacements between the opposing sides, local sliding may be induced near the contact point by differences in material properties or surface geometries. This second, more subtle, type of sliding depends on both the geometry and material properties of the bodies and the frictional characteristics of the surfaces and may be difficult to accurately predict using theoretical models. The complexity of such interactions highlights the need for experimental determination. Measuring the displacement between the initial and final frames only, would result in an underestimate of the sliding length.

Detailed descriptions of sliding may provide information on the frictional properties of the surfaces and have implications to tissue wear. The ability to simultaneously quantify the strains in tissues during sliding may also be important, by giving some indication of the applied normal force. The ability for tissue deformation and interactions to be experimentally quantified during physiological loading may be of use in determining normal or pathological biomechanical processes.

3.6 List of Variables

variable	units	description
\mathbf{a}	μm	initial marker coordinates
\mathbf{d}^{12}	μm	relative position of \mathbf{x}^{M2} to \mathbf{x}^{M1} (equal to $\mathbf{x}^{\text{M2}} - \mathbf{x}^{\text{M1}}$)
\mathbf{d}^{13}	μm	relative position of \mathbf{x}^{M3} to \mathbf{x}^{M1} (equal to $\mathbf{x}^{\text{M3}} - \mathbf{x}^{\text{M1}}$)
D_{contact}	μm	gap distance threshold
E_{ij}	—	Lagrangian strain
\mathbf{g}_{M1}	μm	relative position of \mathbf{x}^{S} to \mathbf{x}^{M1} (equal to $\mathbf{x}^{\text{S}} - \mathbf{x}^{\text{M1}}$)
\mathbf{g}_{M2}	μm	relative position of \mathbf{x}^{S} to \mathbf{x}^{M2} (equal to $\mathbf{x}^{\text{S}} - \mathbf{x}^{\text{M2}}$)
\mathbf{g}_{M4}	μm	relative position of \mathbf{x}^{S} to \mathbf{x}^{M4} (equal to $\mathbf{x}^{\text{S}} - \mathbf{x}^{\text{M4}}$)
\mathbf{g}_n	μm	gap distance between the slave point and master surface
$\Delta \mathbf{g}_n$	μm	gap displacement
$\dot{\mathbf{g}}_n$	$\mu\text{m} \cdot \text{s}^{-1}$	gap velocity
h	μm	initial spacing between mesh points
i	—	coordinate directions: 1,2,3
\mathbf{n}	μm	unit normal to the master surface
\mathbf{n}_{avg}	μm	average unit normal to the master surface over Δt
$\Delta \mathbf{S}$	μm	sliding displacement
$\dot{\mathbf{S}}$	$\mu\text{m} \cdot \text{s}^{-1}$	sliding velocity
sign_n	—	
t	s	time
Δt	s	duration of a single time-step

$\Delta \mathbf{u}$	μm	disp. of a point over Δt
$\Delta \mathbf{U}$	μm	relative disp. of the contacting master surface over Δt
\mathbf{u}	μm	displacement of points
\mathbf{V}	$\mu\text{m}\cdot\text{s}^{-1}$	relative velocity of master surface to the slave point
\mathbf{x}	μm	current marker coordinates evaluated at time t
\mathbf{x}^{M1}	μm	closest mesh point to \mathbf{x}^{P} on the master surface
\mathbf{x}^{M2}	μm	second closest mesh point to \mathbf{x}^{P} on the master surface
\mathbf{x}^{M3}	μm	third closest mesh point to \mathbf{x}^{P} on the master surface
\mathbf{x}^{M4}	μm	fourth closest mesh point to \mathbf{x}^{P} on the master surface
\mathbf{x}^{S}	μm	coordinates of the slave point
\mathbf{x}^{P}	μm	coordinates of the projection \mathbf{x}^{S} onto the master surface
δ_1	μm	coordinates of \mathbf{x}^{P} within the sub-region in \mathbf{d}^{12} direction
δ_2	μm	coordinates of \mathbf{x}^{P} within the sub-region in \mathbf{d}^{13} direction
ξ_1	μm	unit vector in direction of \mathbf{d}^{12}
ξ_2	μm	unit vector in direction of \mathbf{d}^{13}

3.7 Acknowledgments

This chapter has been submitted, in part, for publication in *Journal of Biomechanics*. The dissertation author is the primary investigator and thanks co-author

Dr. Robert Sah. This work was supported in part by the National Institutes of Health and the National Science Foundation, and by a grant to the University of California, San Diego, in support of Dr. Robert Sah, from the Howard Hughes Medical Institute through the HHMI Professors Program.

3.8 References

1. Anderson DD, Brown TD, Radin EL: Stress wave effects in a finite element analysis of an impulsively loaded articular joint. *Proc Inst Mech Eng [H]* 205:27-34, 1991.
2. Armstrong CG: An analysis of the stresses in a thin layer of articular cartilage in a synovial joint. *Eng Med* 15:55-61, 1986.
3. Ateshian GA, Lai WM, Zhu WB, Mow VC: An asymptotic solution for the contact of two biphasic cartilage layers. *J Biomech* 27:1347-60, 1994.
4. Ateshian GA, Wang H: A theoretical solution for the frictionless rolling contact of cylindrical biphasic articular cartilage layers. *J Biomech* 28:1341-55, 1995.
5. Bae WC, Lewis CW, Levenston ME, Sah RL: Indentation testing of human articular cartilage: effects of probe tip geometry and indentation depth on intra-tissue strain. *J Biomech* 39:1039-47, 2006.
6. Blankevoort L, Kuiper JH, Huiskes R, Grootenboer HJ: Articular contact in a three-dimensional model of the knee. *J Biomech* 24:1019-31, 1991.
7. Boman R, Ponthot JP: Finite element simulation of lubricated contact in rolling using the arbitrary Lagrangian-Eulerian formulation. *Comput Method Appl M* 193:4323-53, 2004.
8. Costandi PN, McCulloch AD, Omens JH, Frank LR: High-resolution longitudinal MRI of the transition to heart failure. *Magn Reson Med* 57:714-20, 2007.
9. Donzelli PS, Spilker RL, Ateshian GA, Mow VC: Contact analysis of biphasic transversely isotropic cartilage layers and correlations with tissue failure. *J Biomech* 32:1037-47, 1999.
10. Eckstein F, Lemberger B, Gratzke C, Hudelmaier M, Glaser C, Englmeier KH, Reiser M: In vivo cartilage deformation after different types of activity and its dependence on physical training status. *Ann Rheum Dis* 64:291-5, 2005.
11. Fernandez JW, Hunter PJ: An anatomically based patient-specific finite element model of patella articulation: towards a diagnostic tool. *Biomech Model Mechan* 4:20-38, 2005.
12. Freeman MA, Pinskerova V: The movement of the normal tibio-femoral joint. *J Biomech* 38:197-208, 2005.
13. Fung YC. *Biomechanics: Mechanical Properties of Living Tissues*. New York: Springer-Verlag; 1981.
14. Fung YC. *Biomechanics: Motion, Flow, Stress, and Growth*. New York: Springer-Verlag; 1981.

15. Gilchrist CL, Witvoet-Braam SW, Guilak F, Setton LA: Measurement of intracellular strain on deformable substrates with texture correlation. *J Biomech* 40:786-94, 2007.
16. Goldin B, Block WD, Pearson JR: Wound-Healing of Tendon .1. Physical, Mechanical and Metabolic Changes. *J Biomech* 13:241-&, 1980.
17. Guilak F, Sah RL, Setton LA: Physical regulation of cartilage metabolism. In: *Basic Orthopaedic Biomechanics*, ed. by VC Mow, Hayes WC, Raven Press, New York, 1997, 179-207.
18. Hashima AR, Young AA, McCulloch AD, Waldman LK: Nonhomogeneous analysis of epicardial strain distributions during acute myocardial ischemia in the dog. *J Biomech* 26:19-35, 1993.
19. Hayes WC, Keer LM, Herrmann KG, Mockros LF: A mathematical analysis for indentation tests of articular cartilage. *J Biomech* 5:541-51, 1972.
20. Herzog W, Federico S: Considerations on joint and articular cartilage mechanics. *Biomech Model Mechan* 5:64-81, 2006.
21. Hou JS, Holmes MH, Lai WM, Mow VC: Boundary conditions at the cartilage-synovial fluid interface for joint lubrication and theoretical variations. *J Biomech Eng* 111:78-87, 1989.
22. Hou JS, Mow VC, Lai WM, Holmes MH: An anlysis of the squeeze-film lubrication mechanism for articular cartilage. *J Biomech* 25:247-59, 1992.
23. Intaglietta M, Tompkins WR: On-line measurement of microvascular dimensions by television microscopy. *J Appl Physiol* 32:546-51, 1972.
24. Jadin KD, Wong BL, Bae WC, Li KW, Williamson AK, Schumacher BL, Price JH, Sah RL: Depth-varying density and organization of chondrocyte in immature and mature bovine articular cartilage assessed by 3-D imaging and analysis. *J Histochem Cytochem* 53:1109-19, 2005.
25. Johnson KL. Contact Mechanics. New York: Cambridge University Press; 1985.
26. Kiviranta I, Tammi M, Jurvelin J, Saamanen AM, Helminen HJ: Moderate running exercise augments glycosaminoglycans and thickness of articular cartilage in the knee joint of young beagle dogs. *J Orthop Res* 6:188-95, 1988.
27. Klein TJ, Chaudhry M, Bae WC, Sah RL: Depth-dependent biomechanical and biochemical properties of fetal, newborn, and tissue-engineered articular cartilage. *J Biomech* 40:182-90, 2007.
28. Laursen TA: The Convected Description in Large-Deformation Frictional Contact Problems. *Int J Solids Struct* 31:669-81, 1994.

29. Loring SH, Brown RE, Gouldstone A, Butler JP: Lubrication regimes in mesothelial sliding. *J Biomech* 38:2390-6, 2005.
30. McCulloch AD, Omens JH: Non-homogeneous analysis of three-dimensional transmural finite deformation in canine ventricular myocardium. *J Biomech* 24:539-48, 1991.
31. Meier GD, Bove AA, Santamore WP, Lynch PR: Contractile function in canine right ventricle. *Am J Physiol* 239:H794-804, 1980.
32. Meyer AE, Baier RE, Chen HG, Chowhan M: Tissue-on-tissue testing of dry eye formulations for reduction of bioadhesion. *J Adhesion* 82:607-27, 2006.
33. Nugent GE, Aneloski NA, Schmidt TA, Schumacher BL, Voegtline MS, Sah RL: Dynamic shear stimulation of bovine cartilage biosynthesis of proteoglycan 4 (PRG4). *Arthritis Rheum* 54:1888-96, 2006.
34. Nugent-Derfus GE, Takara T, O'Neill J K, Cahill SB, Gortz S, Pong T, Inoue H, Aneloski NM, Wang WW, Vega KI, Klein TJ, Hsieh-Bonassera ND, Bae WC, Burke JD, Bugbee WD, Sah RL: Continuous passive motion applied to whole joints stimulates chondrocyte biosynthesis of PRG4. *Osteoarthritis Cartilage* 15:566-74, 2007.
35. Pietrzak G, Curnier A: Large deformation frictional contact mechanics: continuum formulation and augmented Lagrangian treatment. *Comput Method Appl M* 177:351-81, 1999.
36. Quinn TM, Allen RG, Schalet BJ, Perumbuli P, Hunziker EB: Matrix and cell injury due to sub-impact loading of adult bovine articular cartilage explants: effects of strain rate and peak stress. *J Orthop Res* 19:242-9, 2001.
37. Salter RB, Simmonds DF, Malcolm BW, Rumble EJ, MacMichael D, Clements ND: The biological effect of continuous passive motion on the healing of full-thickness defects in articular cartilage. *J Bone Joint Surg Am* 62-A:1232-51, 1980.
38. Schinagl RM, Gurskis D, Chen AC, Sah RL: Depth-dependent confined compression modulus of full-thickness bovine articular cartilage. *J Orthop Res* 15:499-506, 1997.
39. Schinagl RM, Ting MK, Price JH, Sah RL: Video microscopy to quantitate the inhomogeneous equilibrium strain within articular cartilage during confined compression. *Ann Biomed Eng* 24:500-12, 1996.
40. Simo JC, Laursen TA: An Augmented Lagrangian Treatment of Contact Problems Involving Friction. *Comput Struct* 42:97-116, 1992.
41. Wang CC, Deng JM, Ateshian GA, Hung CT: An automated approach for direct measurement of two-dimensional strain distributions within articular cartilage under unconfined compression. *J Biomech Eng* 124:557-67, 2002.

CHAPTER 4

THE EFFECTS OF FOCAL ARTICULAR DEFECTS ON CARTILAGE CONTACT MECHANICS

4.1 Abstract

Focal damage to articular cartilage is found commonly in arthroscopy patients and the alteration of the mechanical environment of the chondrocytes may contribute to progressive degeneration of the cartilage. Chapter 2 established that local strain elevations occur in the cartilage adjacent to and opposing a focal defect directly after application of a load, but the effects of a defect on the time-course of strain development and redistribution and the dynamic contact of opposing surfaces are unclear. The objective of this study was to quantify changes in intra-tissue strain occurring in cartilage near and opposing a focal defect during dynamic loading and stress relaxation. Pairs of intact osteochondral blocks from the femoral condyles of mature bovine knees were compressed uniaxially by 20% of the total cartilage thicknesses, and allowed to stress relax for 1 hr in the compressed state. Tissue deformation during compression and at several time-points during relaxation was recorded by video microscopy. Following testing, a single, full-thickness chondral defect was created in one block from each pair with one of two edge orientations:

“open” defects (sloping down into the defect from the rim) or “closed” defects (tissue at the rim overhanging into the defect). The blocks were allowed to re-swell for >1 hr and then tested a second time using the same protocol. The edges of the defect were then re-cut to have the opposite edge orientation, allowed to re-swell for >1 hr, and tested for a third and final time. Stained nuclei, acting as fiducial markers, were tracked by digital image correlation and used to calculate cartilage intra-tissue strains and relative surface sliding. Intact blocks displayed axial strains that increased with depth and relatively little sliding. In tests of samples with a defect, strain magnitudes were elevated in cartilage adjacent to, and opposing, the defect. Increased sliding was seen between cartilage surfaces adjacent to “closed” defects ($p < 0.05$); there was no effect on sliding of “open” defects. Localized alterations in strain and strain rate may contribute to altered chondrocyte metabolism, chondrocyte death, matrix damage, or accelerated wear *in vivo*.

4.2 Introduction

Focal defects in articular cartilage are commonly found in symptomatic knees [11, 18], and may be implicated in the progressive degeneration of cartilage [9, 19, 24, 39, 43]. Although the exact mechanism by which defects result in cartilage damage have not been elucidated, prior studies have suggested a mechanical role in this process.

A variety of excessive mechanical loading protocols have been shown to result in both matrix damage [20, 32, 33, 37, 42] and cell death [10, 12, 13, 20, 23, 26, 30, 32, 37]. However, the exact conditions that result in this damage have not been established. The magnitudes of applied or local strains [4] may be correlated to some of this damage. Additionally, the strain rate of the tissue has been identified as a determinant of the extent of tissue damage, with higher strain rates proving more destructive [32]. Over time, even moderate increases in load may be expected to accelerate the rates of both mechanical fatigue [5, 40, 41] and wear [1, 25]. Additionally, changes in the magnitudes or dynamics of cartilage loading may affect the cellular response of the tissue[34], and in the long-term, mechanical stimuli may regulate the processes of tissue growth and remodeling [17]. Changes to the dynamic tissue response to loading that may occur with a defect could significantly contribute to tissue damage or changes in cellular activity.

Changes in mechanical environments of focal defects have been predicted and experimentally measured in *in vitro* systems. Peak and average contact stresses and contact stress gradients are increased along surfaces adjacent to the rim of a focal

defect [8, 16]. Similar results are observed for analogous surface incongruities (i.e. intra-articular step-offs [7, 27, 28] or misaligned grafts [22]). However, the loss of contact area at a defect site is offset by the radial recruitment of new contact area, helping to limit increases in contact stresses [8]. Increased deformation of tissue surrounding a defect must be present to allow the redistribution of load onto the surrounding surfaces. These large macroscopic deformations in the surfaces surrounding and opposing focal defects [6] have been observed in histological sections of loaded joints. Additionally, theoretical models of cartilage contact have predicted that lower congruity between contacting surfaces will result in a decrease in fluid support and thus greater loading on the solid matrix [2]. And finite element models of joints with focal defects, which predict changes in contact stresses that are in close agreement with *ex vivo* experimental measurements, predict increased strains in the tissue adjacent to a defect [31].

Several past studies have measured intra-tissue cartilage strains under a variety of loading conditions by optically tracking cell nuclei [3, 21, 35, 36, 38]. Chapter 2 of this dissertation extended these methods to investigate the contact of two independent cartilage surfaces, quantifying 2-D cartilage deformation directly following the application of a uniaxial compressive load in both intact and defect-containing surfaces. In chapter 3, methods of mechanical testing and image analysis were developed to allow the dynamic deformation of contacting cartilage surfaces to be automatically tracked, and a detailed mathematical framework to describe the contact between the two surfaces was presented. These methods allow more in depth studies of cartilage contact mechanics to be performed.

Chapter 2 of this thesis demonstrated that the presence of a cartilage defect increases local strain magnitudes in the adjacent and opposing cartilage surfaces and tends to increase the amount of relative lateral displacement between the two surfaces. The hypothesis of the current study is that, in addition to affecting intra-tissue strain distributions directly following loading, the presence of a defect also alters the time-course of strain development and surface sliding during loading and the redistribution of strain during relaxation. Thus, the objectives were to 1) quantify the distribution of intra-tissue strains during uniaxial compression and stress relaxation of opposing intact, and defect-containing, cartilage samples and 2) determine the effect of defect presence and edge orientation on the sliding between contacting surfaces. Knowledge of changes in the mechanical environment arising near a focal defect could help to identify tissue regions most susceptible to damage and provide data to verify and improve theoretical models of cartilage contact.

4.3 Materials and Methods

Study Design

Mechanical testing was first performed on 4 pairs of intact osteochondral blocks, as a normal control. Following testing, a single, 4 mm wide, full-thickness defect was created in the center of one block from each sample pair. The defect edge was created at either a slightly “open” ($\sim 100^\circ$) or slightly “closed” ($\sim 80^\circ$) orientation, with respect to the defect base (Figure 4.1A). Samples were allowed to re-equilibrate for at least 1 hr in SF+PIs, and then retested using the same mechanical testing protocol. The defect edge was then re-cut, to have the opposite orientation (closed edges were made open and vice versa); samples were again allowed to re-equilibrate for at least 1 hr in SF+PIs and retested a final time using the same mechanical testing protocol. The initial orientation of the defect edge was randomly chosen for each sample.

Sample Preparation

Macroscopically normal osteochondral blocks ($10 \times 10 \times 2.5 \text{ mm}^3$; $L \times W \times H$) with smooth, intact surfaces were harvested from the femoral condyles of mature bovine knees (Figure 4.1A). Blocks were soaked in phosphate buffered saline (PBS) with the addition of protease inhibitors (PIs) [15] and stored at -70°C until testing. Blocks were thawed by immersion in PBS+PIs, stained (cell nuclei) for at least 4 hr at 4°C with $20 \mu\text{g/ml}$ propidium iodide in PBS+PIs, and then equilibrated for 12 hr at 4°C in bovine synovial fluid (SF)+PIs, to ensure normal surface lubrication. Prior to testing, cartilage thickness was optically measured at 5 places spanning the sample

width; sample cartilage thickness was recorded as the average of these 5 measurements. Blocks obtained from the same knee were tested against each other to match the mechanical properties of the opposing sides.

Defects were created by making 3 vertical incisions (center of the sample width, and 2 mm to each side of center) ~perpendicular to the articular surface and extending through the calcified cartilage layer. The cartilage was then undercut along the bone starting at the center cut and cutting towards each edge until the cartilage released.

Micro-scale Mechanical Testing

Mechanical testing was performed in a microscope-mounted test chamber, as described in Chapters 2 and 3 (Figure 4.1B) [3, 21, 35, 36]. Briefly, pairs of blocks were positioned with their articular surfaces opposing and aligned perpendicular to the direction of loading (z-axis). Tissue deformation was imaged through the glass chamber bottom (x-z plane) using a Nikon Diaphot 300 epi-fluorescence microscope fitted with a G-2A filter cube (Nikon, Melville, NY). Samples were imaged at 4x magnification ($\sim 1.8 \times 2.8 \text{ cm}^2$ field of view) and digital images (512x768 pixel resolution) were recorded with a charge-coupled device camera (Model 4913-5000, Cohu, Inc., San Diego, CA). Samples were loaded under uniaxial unconfined compression to a total bone-to-bone strain of 20% (defined as the applied displacement/sum of the cartilage thicknesses), at a strain rate of $1\% \cdot \text{s}^{-1}$ using a displacement controlled actuator (Model MFN25PP, Newport Corporation, Irvine, CA).

Image Acquisition

Digital images of the contacting surfaces (centered at the defect rim where applicable) were acquired directly prior to loading, during loading at a rate of 4 frames/s ($\sim 8 \mu\text{m}$ applied displacement/frame), directly following loading, and during stress relaxation (30 s intervals between 1 and 6 min after loading, and then at 10, 15, 30, and 60 min). Additional, static digital images of chosen regions were acquired directly prior to loading and in the stress relaxed state for regions near the bone, the contacting surfaces far removed from the defect ($x = 1\text{:}3 \text{ mm}$), and the opposing surface region over the center of the defect ($x = -1\text{:}-3 \text{ mm}$).

Endpoint measures

Indices of the biomechanics of cartilage contact were quantified from the acquired images as outlined in this section and as described in detail below. Macroscopic changes in deformation of the opposing tissue surfaces and sliding behavior were observed qualitatively. Intra-tissue strains were calculated at $100 \mu\text{m}$ spacing, in full-thickness regions of both cartilage layers at each time-point during loading and stress relaxation using the acquired images.

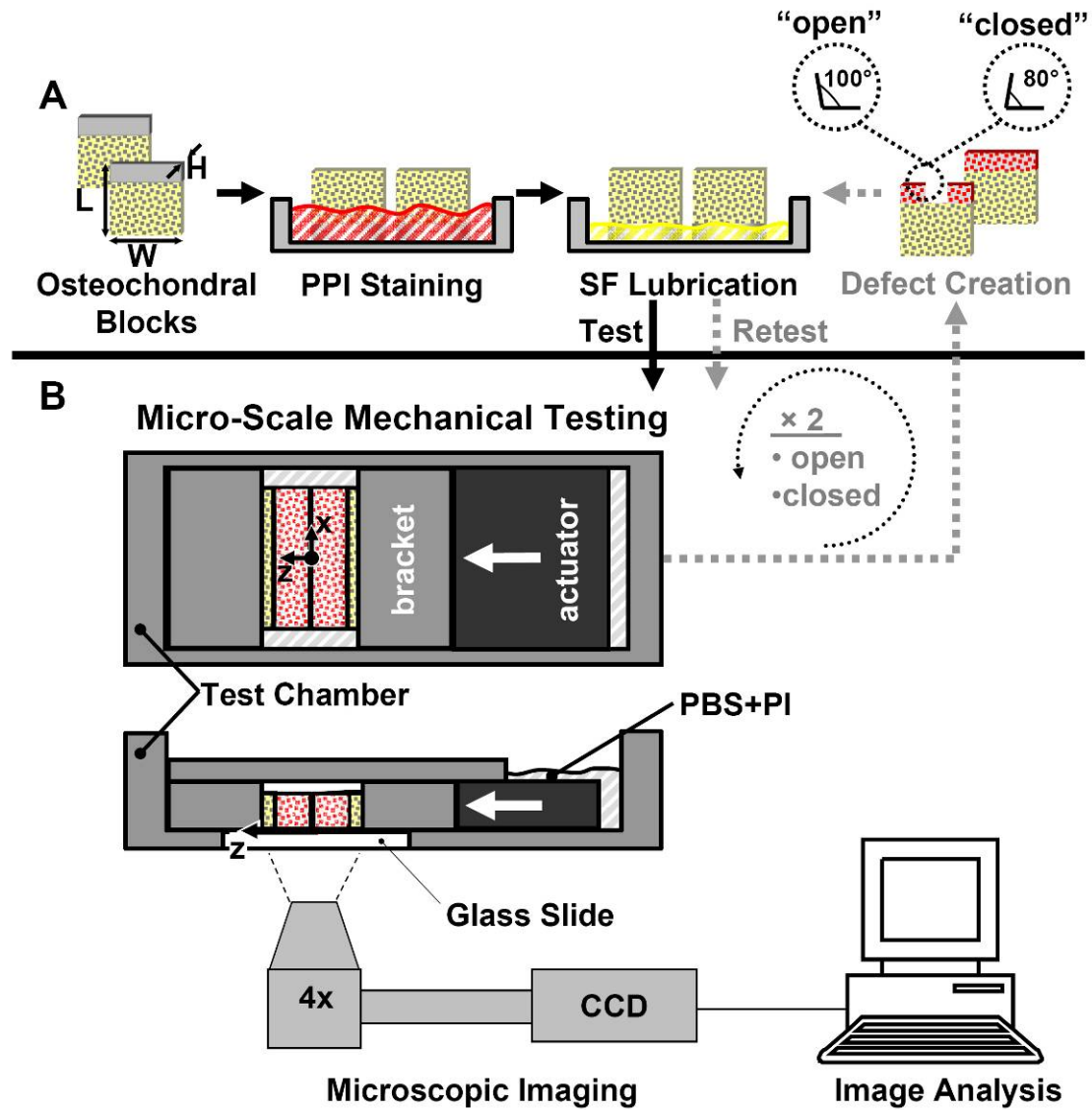


Figure 4.1: Sample preparation (A) and micro-mechanical testing (B) of opposing osteochondral blocks.

Strain values at select sub-regions (Figure 4.2) were then averaged between samples and analyzed statistically to determine the effects of defect presence on the magnitudes and distribution of strain components within the tissue at two time-points: 1) directly following loading and 2) after 60 min stress relaxation. Statistical analyses were performed on the same set of sub-region locations introduced in Chapter 2. In the intact case, strains were averaged in rectangular, 100 μm tall (in the z-direction) \times 500 μm wide (in the x-direction) strips at superficial, S (z = surface to 100 μm), middle, M (bovine: z = 300 to 400 μm), and deep, D (z = 900 to 1000 μm) depths. In defect samples, strains were analyzed in 100 \times 100 μm sub-regions at S, M, and D depths and at different lateral positions along the two cartilage layers: A1 (x = 500 to 600 μm), A2 (x = 200 to 300 μm), and A3 (x = 0 to 100 μm), in the adjacent cartilage, and O1 (x = 500 to 600 μm), O2 (x = 200 to 300 μm), O3 (x = 50 to -50 μm), O4 (x = -200 to -300 μm), O5 (x = -500 to -600 μm) in the opposing cartilage.

Sliding between surfaces was calculated from surface displacements during the dynamic loading phase using the methods described in detail in Chapter 3. In intact control samples, the average sliding distance over the 500 μm analysis region was calculated. For defect samples, sliding was calculated at several points along the adjacent cartilage surface (x = 0, 100, 200, 300, 400, 500 μm). Additionally, sliding distances for each sample were averaged over the 500 μm long analyzed regions and divided by the applied axial displacement at four time-points (corresponding to applied compressive strains of -0.05, -0.10, -0.15, and -0.20), with the average of these four time-points providing a normalized sliding distance for the sample.

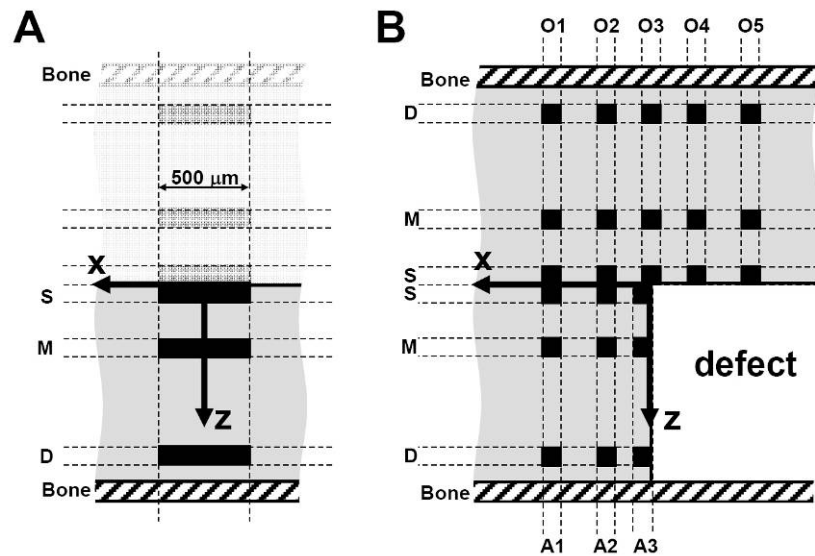


Figure 4.2: Locations of sub-regions used for statistical analysis of strain distributions in (A) intact control and (B) defect-containing samples. Measurements were made at three tissue depths: S $\{z = 0:100 \mu\text{m}\}$; M $\{z = 300:400 \mu\text{m}\}$, D $\{z = 900:1000 \mu\text{m}\}$. For intact control samples, a 500 μm width region was averaged to calculate a control strain value at each depth. For defect samples, 100 x 100 μm sub-regions were analyzed for S, M, and D depths at select lateral locations on the adjacent (A1 $\{x = 500:600 \mu\text{m}\}$; A2 $\{x = 200:300 \mu\text{m}\}$; A3 $\{x = 0:100 \mu\text{m}\}$) and opposing (O1 $\{x = 500:600 \mu\text{m}\}$; O2 $\{x = 200:300 \mu\text{m}\}$; O3 $\{x = -50:50 \mu\text{m}\}$; O4 $\{x = -200:-300 \mu\text{m}\}$; O5 $\{x = -500:-600 \mu\text{m}\}$) cartilage surfaces.

Image Analysis

A subset of fluorescently stained cell nuclei, spaced at ~ 15 pixels ($\sim 55 \mu\text{m}$), served as fiducial markers of material points in digital images of the tissue during loading and stress relaxation. Cell tracking was performed and deformation was calculated using a custom program written in MATLAB 6.5 using functions from the Image Processing Toolbox (Mathworks, Inc., Natick, Massachusetts). The methods for the automated tracking of the fiducial markers and contacting sample surfaces, and the subsequent calculations of intra-tissue strains and surface sliding from those data, are described in detail in Chapter 3.

Surface tracking was performed as described in Chapter 3, and the accuracy of surface tracking was manually verified. In certain instances, large changes in the axial intensity profile of the image resulted in loss of surface tracking. Loss of surface tracking was generally related to one of two phenomena: 1) surfaces starting with a noticeable gap between them and coming into contact, or 2) the consolidation of the tissue between the image directly following loading and the first image in the relaxation sequence (1 min after loading). In these cases, points were manually repositioned in the following frame and tracking was restarted from that point. Since the opposing surfaces remained in contact, surface points were selected once and used to define both surfaces.

Mesh-points where displacements would be quantified and used to calculate displacement gradients, Lagrangian strains, and surface sliding were defined in the manually-selected region of interest (ROI) at $100 \mu\text{m}$ spacing. Initial positions of the mesh-points were determined using the boundary of the ROI, the axial position of the

surface, and the lateral location of the defect edge (where applicable), as is described in detail in chapter 2.

In-plane area changes in the contacting cartilage surfaces were calculated from the displacement gradients at each point. Since large deformations were present in many tissue regions, the change in area at each point was calculated as:

$$\frac{dA - dA_0}{dA_0} = \det \begin{pmatrix} 1 + \frac{\partial u}{\partial x} & \frac{\partial u}{\partial z} \\ \frac{\partial w}{\partial x} & 1 + \frac{\partial w}{\partial z} \end{pmatrix} \quad (1)$$

Estimates of local volumetric changes were also calculated within the tissue. Since only 2-D measurements were recorded in the current experimental setup, out-of-plane displacement gradients were approximated from values of in-plane displacement gradients measured in intact control samples. Volume changes could then be estimated using equation (1) with components in 3 dimensions.

The cartilage surfaces were assumed to be a transversely isotropic material, with properties being equal in the plane parallel to the articular surface (x and y). In the current setup, this allows the out-of-plane strains in the intact control samples to be approximated as equal to the strains in the lateral direction. Using this assumption, it is possible to define:

$$\frac{\partial v}{\partial y} = \frac{\partial u}{\partial x} \quad (2)$$

$$\frac{\partial v}{\partial z} = \frac{\partial u}{\partial z} \quad (3)$$

$$\frac{\partial w}{\partial y} = \frac{\partial w}{\partial x} \quad (4)$$

Next, the shear gradients in the x-y plane were assumed to be negligible, so:

$$\frac{\partial v}{\partial x} = 0 \quad (5)$$

$$\frac{\partial u}{\partial y} = 0 \quad (6)$$

For the defect case, high values of shear and tension develop in the lateral in-plane direction in both the adjacent and opposing surfaces because of the surface incongruity at the defect edge. However, the out-of-plane direction (parallel to the defect edge) does not see the same incongruity and would likely experience strains similar to those measured in the intact case. Therefore, out-of-plane displacement gradients in the defect samples were approximated as:

$$\frac{\partial v}{\partial y} = \text{average } \frac{\partial u}{\partial x} \text{ at same depth of intact control samples} \quad (7)$$

$$\frac{\partial v}{\partial z} = \text{average } \frac{\partial u}{\partial z} \text{ at same depth of intact control samples} \quad (8)$$

$$\frac{\partial w}{\partial y} = \text{average } \frac{\partial w}{\partial x} \text{ at same depth of intact control samples} \quad (9)$$

$$\frac{\partial v}{\partial x} = 0 \quad (10)$$

$$\frac{\partial u}{\partial y} = 0 \quad (11)$$

Using those assumptions, volume changes could be calculated as:

$$\frac{dV - dV_0}{dV_0} = \det \begin{pmatrix} 1 + \frac{\partial u}{\partial x} & \frac{\partial u}{\partial y} & \frac{\partial u}{\partial z} \\ \frac{\partial v}{\partial x} & 1 + \frac{\partial v}{\partial y} & \frac{\partial v}{\partial z} \\ \frac{\partial w}{\partial x} & \frac{\partial w}{\partial y} & 1 + \frac{\partial w}{\partial z} \end{pmatrix} \quad (12)$$

Sliding calculations were performed as described in chapter 3. Since the contacting surfaces were visually confirmed to remain in contact and were defined identically for the two cartilage layers, the gap distance at all time-points was ~ 0 . In the analyses, contact was defined numerically as a gap distance of < 1 pixel ($\sim 4 \mu\text{m}$) to account for slight numerical errors introduced by the approximation of the curved surfaces as linear segments.

Since non-negligible magnitudes of sliding were observed between intact control surfaces, the sliding measured near defects was considered as the sum of two separate components: 1) the intrinsic sliding between a particular pair of cartilage blocks and 2) the sliding due to the defect. During loading of intact blocks, the direction of sliding varied depending on the characteristics of the individual blocks. On the other hand, sliding near a defect always took place in the same direction, with the adjacent cartilage moving towards the defect with respect to the opposing surface. Thus, in cases where significant sliding occurs between the intact surfaces, sliding at a defect may be exaggerated when the two contributions are in the same direction, and reduced when the two contributions are in opposite directions. To better discern the effects of a defect, sliding distances at each analyzed time-point were first adjusted by subtracting the relative lateral displacement (RLD) measured between intact blocks at the same level of applied compression. Since the majority of sliding in the current

experimental setup occurs in the lateral direction (especially in the intact case), the RLD provided a good estimate of the tendency of the surfaces to slide preferentially in a given direction. For each surface, lateral (x- direction) displacement was fit to a linear function of x- position (Figure B.1). The average RLD for each intact surface was then determined as the difference between the lateral displacements calculated from the two equations at $x=0$ (the center of the block width). The average RLD for each pair of intact blocks was then subtracted from the total sliding distances calculated for points along surfaces of that same pair of blocks in each of the 3 sample configurations (intact, “open” defect and “closed” defect). All sliding data is reported as the differential values.

Statistics

Data are presented as mean \pm SEM, unless otherwise noted. N=4 pairs of blocks were tested; each pair of blocks was first tested in the intact state and then the same pair was re-tested twice: once with each of the two defect edge orientations. For tests of opposing intact surfaces, strain data from the two opposing surfaces were pooled to provide one set of strain measurements (at S, M, and D depths) per control sample pair. For defect-containing blocks, several lateral locations along the adjacent and opposing cartilage surfaces (as described earlier) were analyzed. All data was log transformed before analysis to adjust for the uneven sample variances. Statistical analyses ($\alpha=0.05$) were performed using Systat 10.2.05 (Systat Software, Richmond, CA) and Microsoft Office Excel 2003 (Microsoft Corporation, Redmond, WA).

Strain and area change data were analyzed over two separate time periods: during loading and during relaxation. First, effects of “open” vs. “closed” defects were

compared (data not shown) in a four-way ANOVA with defect type, tissue depth (S, M, D), surface location (8 groups: A1-A3 and O1-O5) as factors, and time (representing either applied compression or relaxation time) as a repeated factor. Analyses showed no effect of defect type on any strain component during loading ($|E_{xz}|$, $p=0.18$; E_{xx} , $p=0.23$; E_{zz} , $p=0.38$) or relaxation ($|E_{xz}|$, $p=0.47$; E_{xx} , $p=0.28$; E_{zz} , $p=0.76$). Subsequent analyses pooled the strain data from “open” and “closed” orientations, to provide a single strain distribution per sample pair.

The overall effects of tissue depth (S, M, D), surface location (9 groups: control, C; 3 locations on the adjacent surface, A1-A3; and 5 locations on the opposing surface, O1-O5), and time (representing either the applied compression or the relaxation time for loading and relaxation periods, respectively) were analyzed by three-way ANOVA, with tissue depth and time as repeated factors. Additionally, the regional variations in strain were analyzed in detail at two specific time-points: post-loading and post-relaxation. Planned comparison (*a priori*) t-tests (for uneven variances) were used to compare the values of strain at each position (S, M, and D depths at locations A1-A3 and O1-O5) along the adjacent and opposing surfaces to the control value (C) at the same depth.

The power of the planned comparisons to detect differences from control values was assessed. Using typical values of variance (0.025) for our samples, we could expect to detect differences in strain magnitudes of 0.10 (~33% change from control) with a Power = 0.66. Higher sample numbers would be necessary if smaller changes in strain magnitudes were of interest (Power = 0.22 for difference of 0.05), but changes in strain magnitudes below a certain threshold may not have significant

physiological effects. In deeper regions, where strain magnitudes were significantly lower, variances were also smaller (~ 0.009), allowing differences in strains of 0.05 to be detected with a Power = 0.50.

The total sliding distances over points along the intact surfaces and surface adjacent to defects were analyzed at 4 time-points during loading (corresponding to applied compressions of approximately -0.05, -0.10, -0.15 and -0.20). At each time-point, planned comparisons were used to compare sliding at points near each of the defect configurations to the average sliding between control samples. For each sample, the average sliding distance over the analyzed 500 μm surface region (adjacent to the defect or in the center of intact samples) was also calculated at each of the 4 time-points. The overall effects and interactions of defect presence and level of applied compression (time-point) were analyzed by two-way ANOVA with applied compression as a repeated factor. Average sliding distances at each time-point were then normalized to the \sim applied axial displacement at that time, and the average value over those 4 times was calculated, representing the normalized sliding distance of the sample. The average normalized sliding distance for the $n=4$ sample pairs was calculated in the intact, open defect, and closed defect configurations. The values were then analyzed by ANOVA with a Tukey post-hoc test.

Power of sliding comparisons was also calculated. At the fully-compressed time-point, differences of 30 μm in sliding could be detected with power=0.50, while 40 μm differences (\sim equal to the sliding experienced by intact controls) could be detected with power=0.80 (assuming typical values of $\sigma=15$ μm for intact controls and $\sigma=20$ μm for defect samples). Generally, the standard deviations of sliding distances

were proportional to the magnitudes of sliding, and power remained high for differences ~equal to control magnitudes.

4.4 Results

Overall, there were significant effects ($p < 0.001$) of tissue depth, surface location, and applied compression (loading time), on both axial and shear strain magnitudes during the loading period (data not shown for intermediate time-points). All first-order ($p < 0.001$) and second-order ($p < 0.05$) interactions between these factors were also significant, indicating that the effects of defects are not experienced equally at all tissue depths and that the time-course of strain development during loading depends on both tissue depth and the lateral location with respect to a defect. Lateral strains were also significantly affected by applied compression, surface location, and their interaction ($p < 0.001$), but was not affected by tissue depth ($p = 0.12$).

In intact samples (Figure 4.3), strains first accumulated in the superficial region, reaching local compressive magnitudes of approximately -0.10 before noticeable deformation occurred in the middle or deep regions. As loading was continued, strains in the superficial region continued to rise, but middle and deep regions also began to accumulate measurable levels of strain. Directly following loading, there was a depth dependent distribution of axial compressive strain (Figure 4.4), with high strains -0.31 ± 0.02 in S, roughly half that amount of strain, -0.18 ± 0.04 , in M, and low levels of strain, -0.03 ± 0.01 , in D. Magnitudes of lateral and shear

strains rose slightly during loading but remained low, generally staying below 0.05 at all depths and time-points.

Cartilage adjacent to a defect (Figure 4.5 and 4.6) experienced increased axial compression, lateral tension, and shear. Strain was again initially carried in the superficial region, but in addition to the axial compression, there was an early onset of lateral tensile strains in the superficial region and increased shear magnitudes as the adjacent cartilage began to bow into the defect region and was resisted by the tractions exerted by the opposing cartilage layer. As loading proceeded, strain rose more quickly in the S and M regions, than in the intact control samples. As the peak displacement was reached, axial strain and shear strain at the defect rim (A3-S) were significantly elevated compared to controls (Figure 4.4; $p < 0.05$).

During stress relaxation, axial strains were significantly affected ($p < 0.001$) by surface location, tissue depth, and relaxation time with significant interactions between the relaxation time and both surface location and depth. Both lateral and shear strains were also significantly affected by surface location ($p < 0.001$), tissue depth ($p < 0.05$), and their interaction ($p < 0.05$), but showed no effect of stress relaxation time ($p > 0.30$) or its interactions ($p > 0.08$).

As intact samples were held in the loaded position, the cartilage quickly began to redistribute strain into the superficial and middle layers. In this relaxed stated, axial strain decreased significantly with depth. Axial compression of the S region averaged -0.36 ± 0.01 , and the M region, -0.27 ± 0.03 . Lateral and shear strains remained low at all tissue depths, not exceeding 0.05.

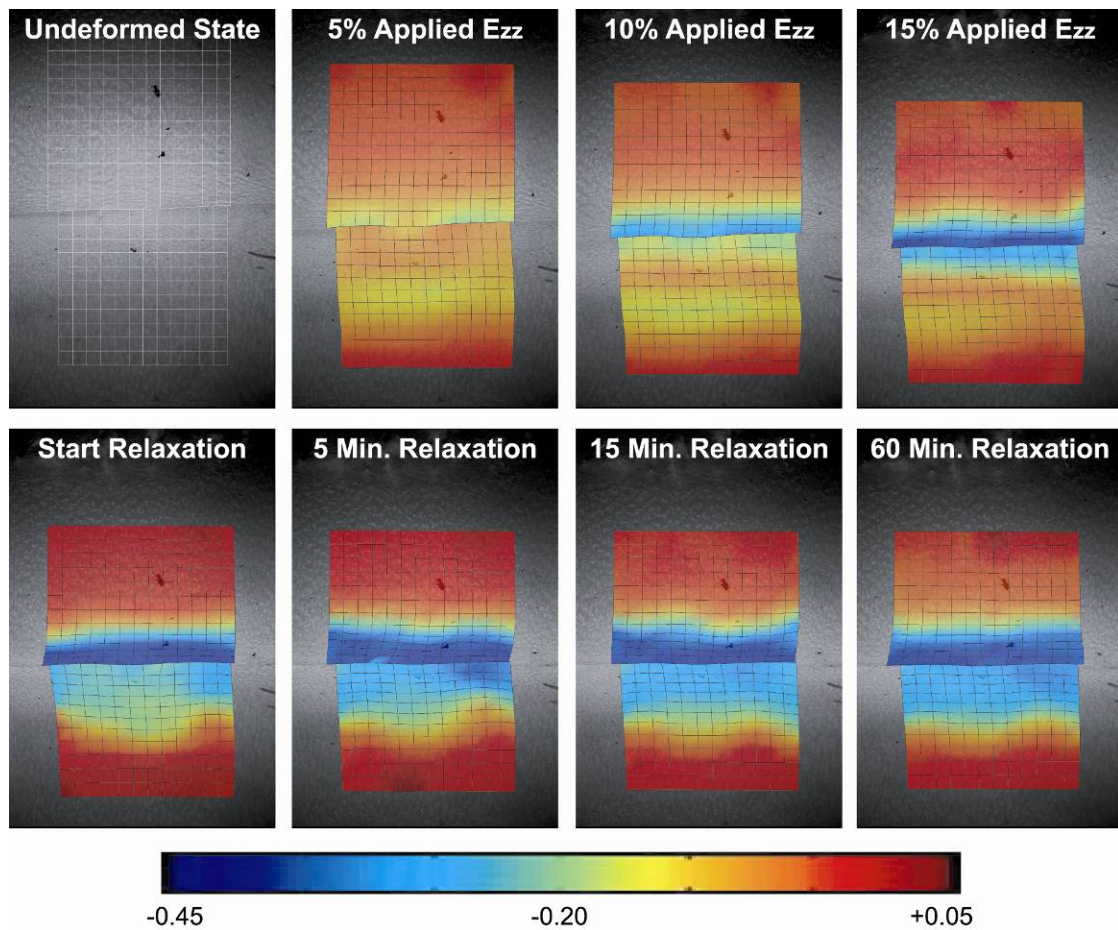


Figure 4.3: Representative images depicting the time-course of axial strain development in intact samples.

During stress relaxation, the strains in the tissue adjacent to a defect reached equilibrium quickly (within 6 minutes post-loading), similar to the behavior of control samples. In the relaxed state, axial strains in S, M, and D regions were no longer significantly different than control values. However, significantly elevated shear strain was still present at the defect rim ($p < 0.05$). Interestingly, there was a strong trend ($p = 0.057$ and $p = 0.053$ after loading and relaxation, respectively) towards increased lateral tensile strains in the deep regions of the adjacent cartilage (A1-D) throughout loading and relaxation, seemingly resisting the bending of the adjacent cartilage into the defect area.

Cartilage opposing the defect rim also experienced significantly elevated strain magnitudes, and displayed a similar time-course of strain development to intact samples. The cartilage remaining in contact with the adjacent surface (O1-O3) patterns of axial strain were similar to intact controls. Increased shear ($p < 0.05$) was experienced in the S and D regions of tissue directly opposing the defect rim (O3), and in the D regions of neighboring regions (O2, O4); shear strains in the D region remained elevated even following stress relaxation. The regions over the empty defect area had significantly lower axial strains ($p < 0.05$) and were slightly compressed in the lateral direction ($p < 0.05$) at both time-points.

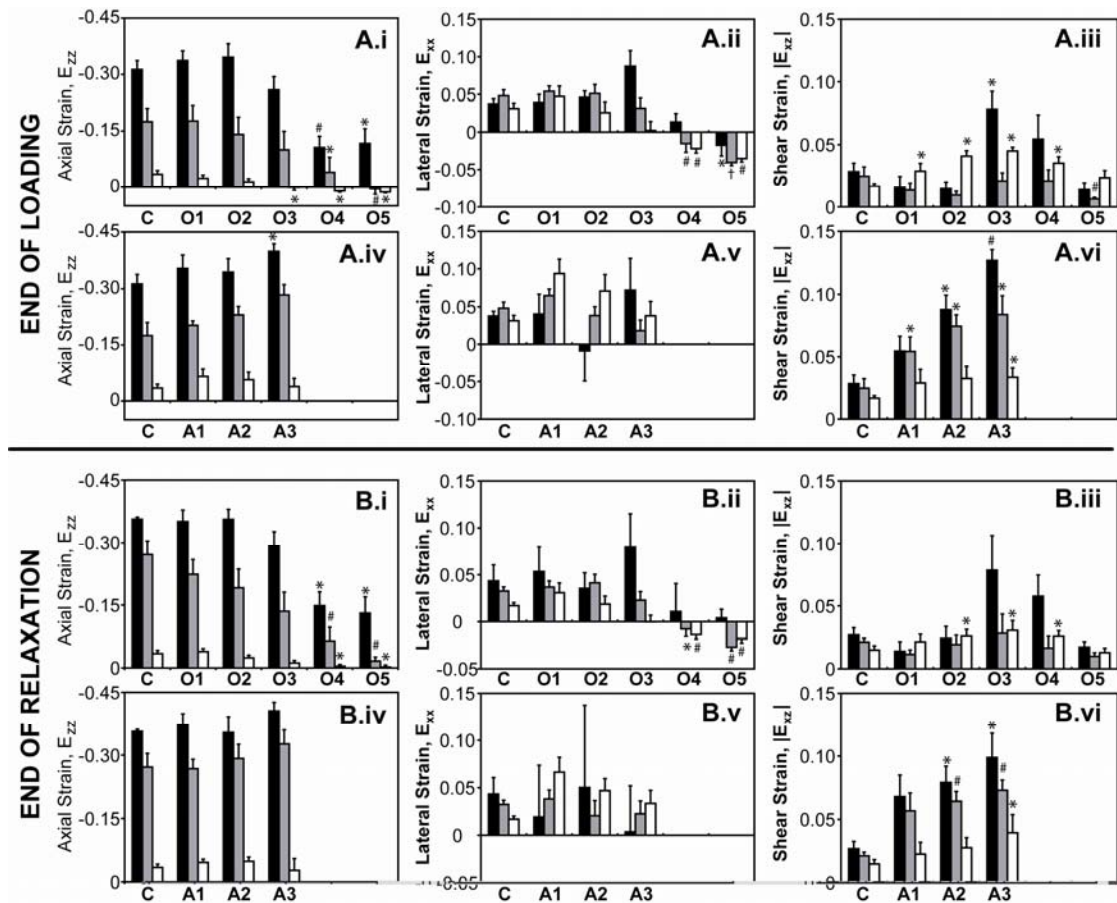


Figure 4.4: Strain measurements at selected sub-regions at time-points directly following loading (A.i-A.vi) and after stress relaxation for 1 hr. (B.i-B.vi). Strains were calculated in 100 x 100 μm sub-regions at S (■), M (■), and D (□) depths for several lateral positions along the cartilage surfaces adjacent (A1-A3) and opposing (O1-O5) a focal defect. Strain in each sub-region was compared to the value from intact control samples (C) at the corresponding depth (* $p < 0.05$; # $p < 0.01$; † $p < 0.001$). Data are expressed as mean \pm SEM. $n=4$.

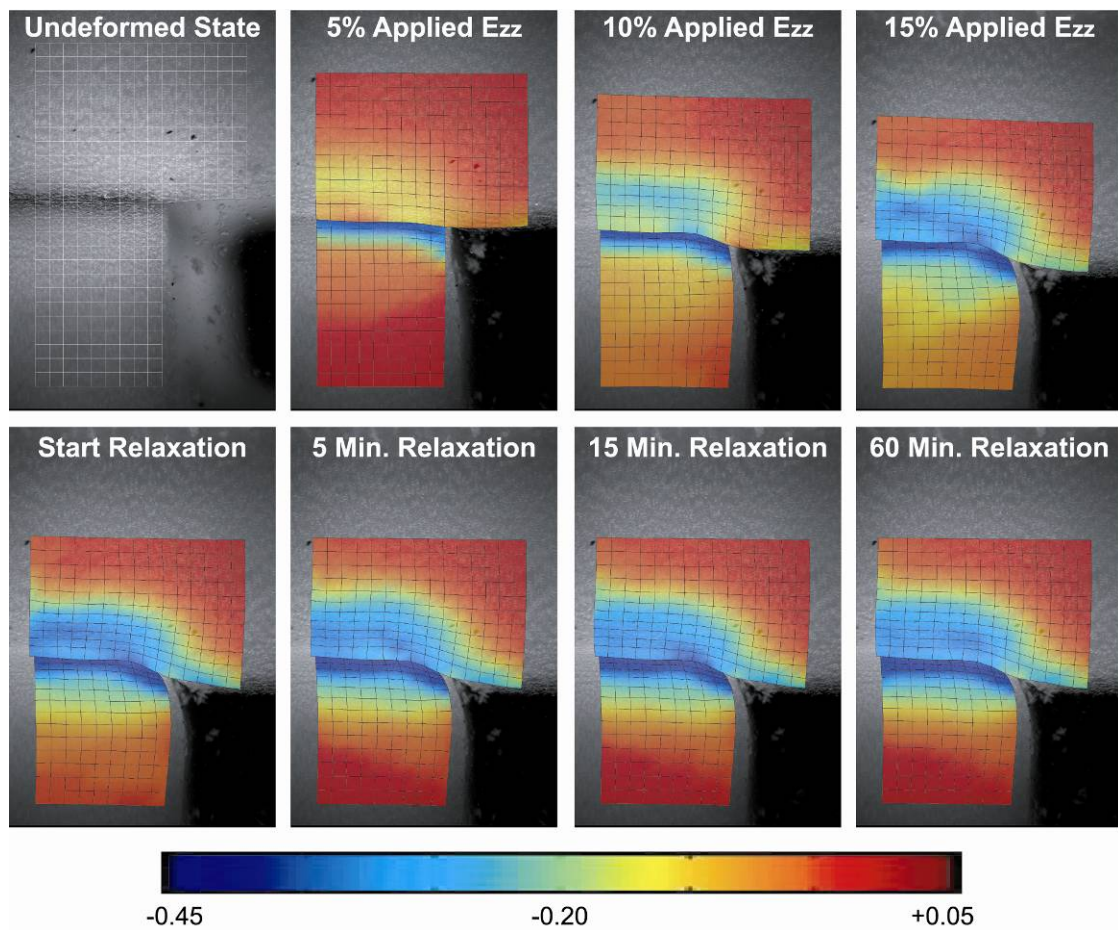


Figure 4.5: Representative images depicting the time-course of axial strain development in defect-containing samples.

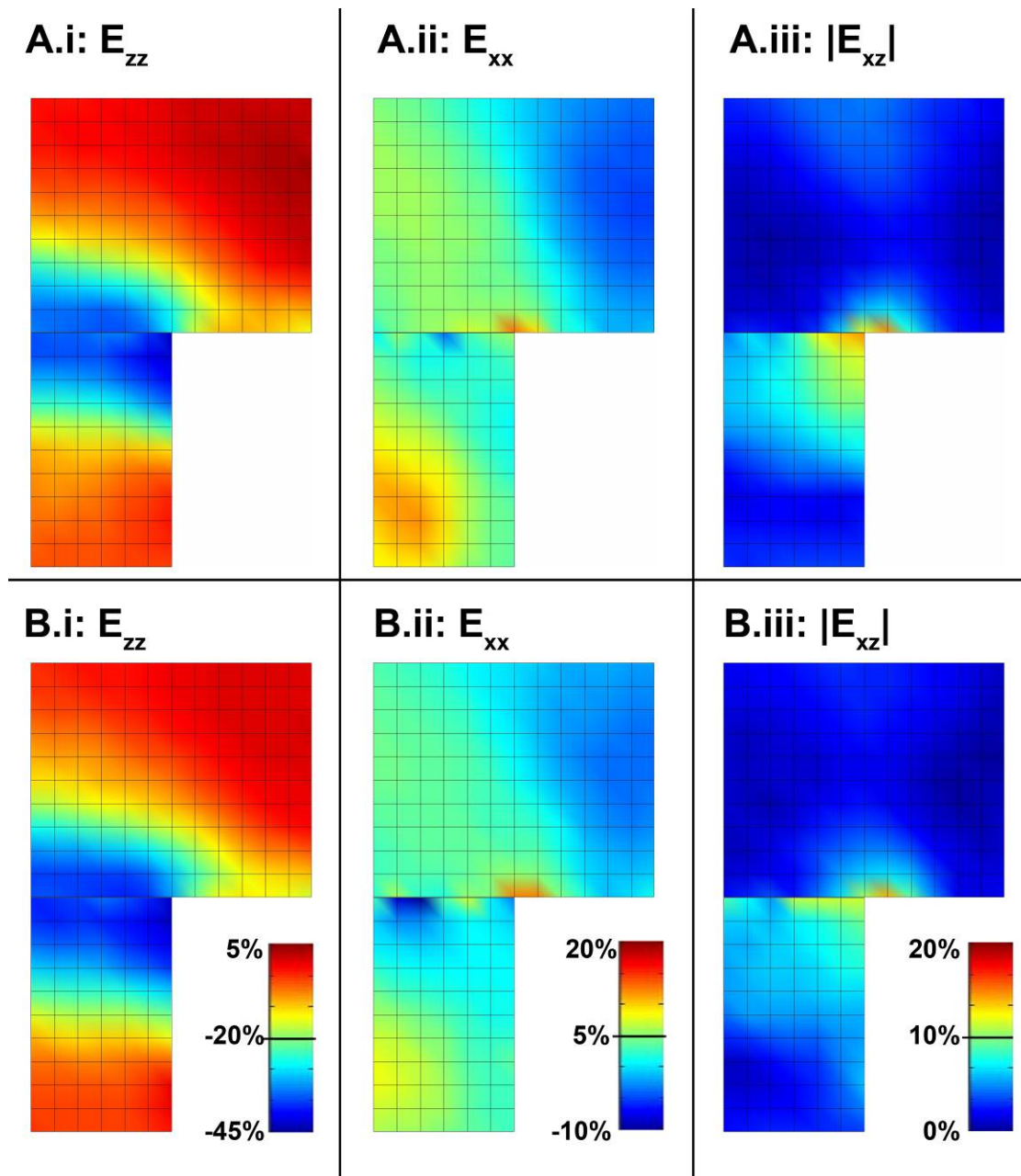


Figure 4.6: Composite strain maps in bovine samples (A) directly following loading or (B) after stress relaxation, for regions $\pm 600 \mu\text{m}$ laterally from the defect and 1 mm depth. Boxes = $100 \times 100 \mu\text{m}^2$.

The time-courses and distributions of area and volume loss (Figure 4.7) closely resembled that of axial strain, with substantial compaction ($>25\%$ volume loss) of tissue near the articular surface directly after loading. Area and volume loss were significantly affected by surface location, tissue depth, time, and their first-order interactions during both loading and relaxation periods ($p<0.01$). The magnitudes of area and volume loss decreased with tissue depth and were negligible in the deep regions. During relaxation, the magnitudes of area and volume loss increased ~ 2 -fold in the S and M regions of intact control surfaces, while the D region tissue remained approximately uncompressed. In defect samples, significantly greater area, -0.64 ± 0.04 , and volume, -0.63 ± 0.05 , loss were measured at the defect rim, than in the superficial regions in intact controls (-0.37 ± 0.05 and -0.34 ± 0.05 , respectively) directly following loading ($p<0.05$). Unlike intact samples, the area and volume of the tissue at the defect rim remained \sim constant during stress relaxation, but was still significantly higher than controls in the stress relaxed state ($p<0.05$).

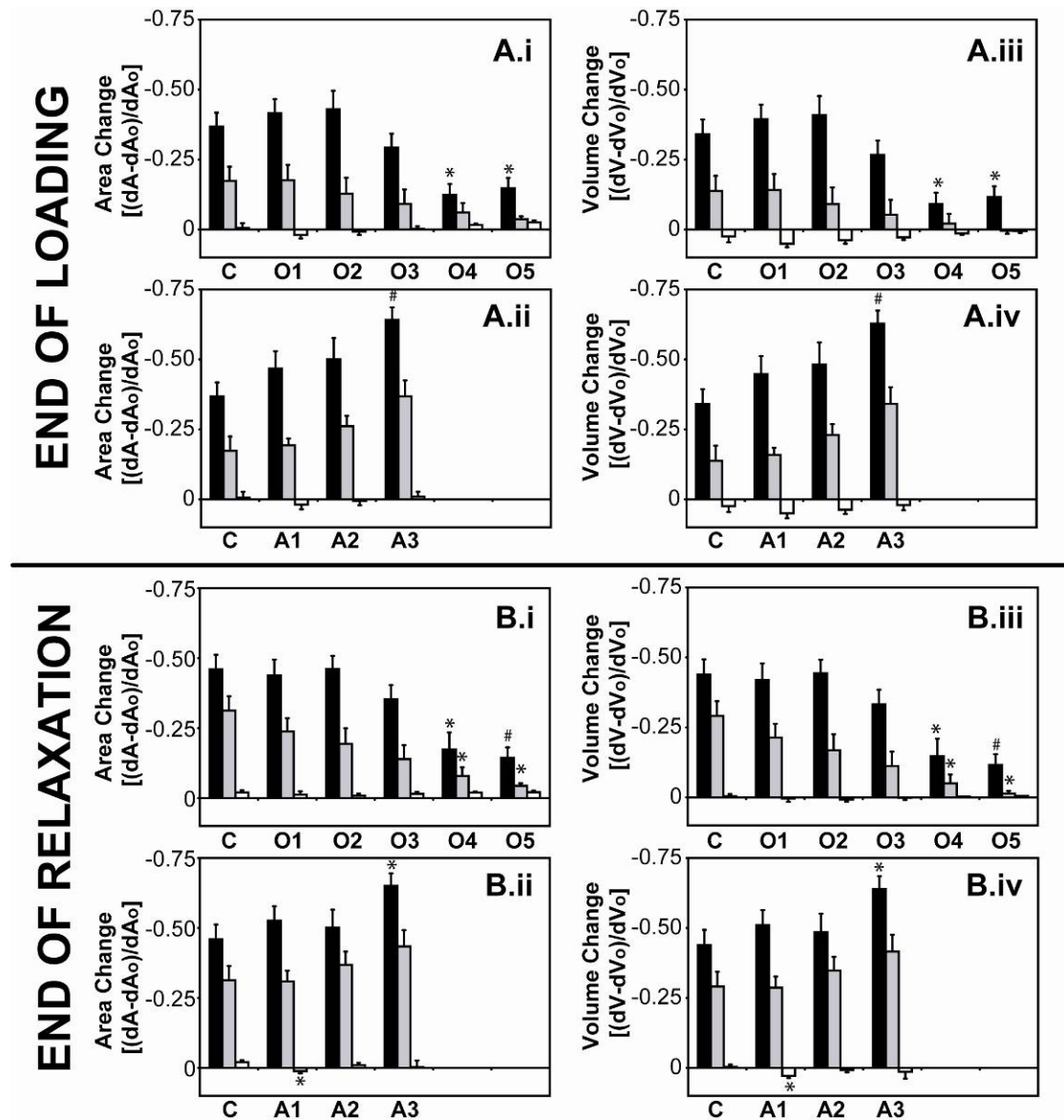


Figure 4.7: Area and volume changes at selected sub-regions in bovine samples directly following loading (A.i-A.iv) or after stress relaxation (B.i-B.iv). Strains were calculated in 100 x 100 μm sub-regions at S (■), M (■), and D (□) depths for several lateral positions along the cartilage surfaces adjacent (A1-A3) and opposing (O1-O5) a focal defect. Strain in each sub-region was compared to the value from intact control samples (C) at the corresponding depth (* $p < 0.05$; # $p < 0.01$; † $p < 0.001$). Data are expressed as mean \pm SEM. $n=4$

Average sliding distances increased with greater applied compression ($p < 0.001$) and differed significantly between sample types ($p < 0.05$), with a significant interaction between those two factors. Sliding distance appeared to be affected by the presence and edge orientation (closed: $79.5^\circ \pm 3.5^\circ$; open: $98.8^\circ \pm 3.0^\circ$) of a defect (Figure 4.8). Increased magnitudes of sliding were measured at all surface points within 500 μm of “closed” defects, at all analyzed time-points ($p < 0.05$). “Open” defect orientations resulted in a trend towards increased sliding, but no statistically significant increases compared to controls. Similar results (Figure 4.9) were seen for average normalized sliding distances (sliding normalized to applied displacement and then averaged across the surface and time). Normalized sliding distances over regions adjacent to “closed” defects, 0.31 ± 0.06 , were significantly greater ($p < 0.05$) than controls, 0.05 ± 0.03 , while normalized sliding near “open” defects, 0.16 ± 0.06 , showed no significant increase over controls ($p = 0.37$).

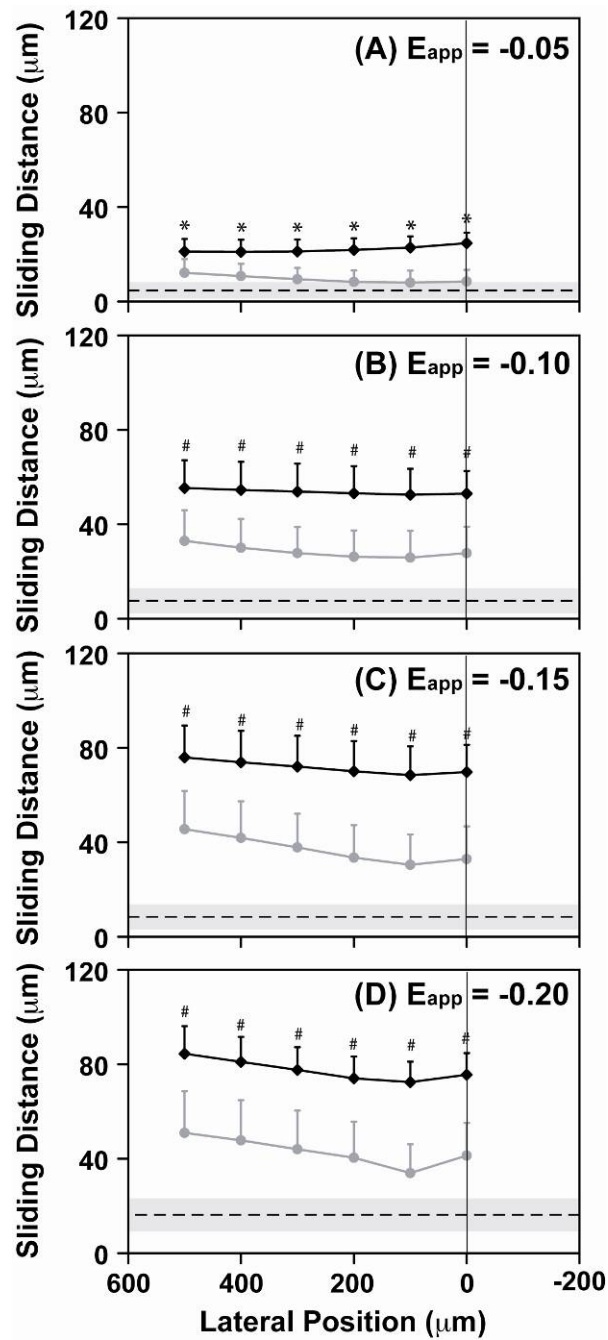


Figure 4.8: Sliding distance profiles over surfaces of open defect (gray line) and closed defect (black line) samples compared to the average sliding over intact surfaces (mean: dotted line ; SEM: shaded region) at several levels of applied compression (-0.05, -0.10, -0.15, and -0.20). (*p<0.05; #p<0.01 compared to control at same time-point) n=4.

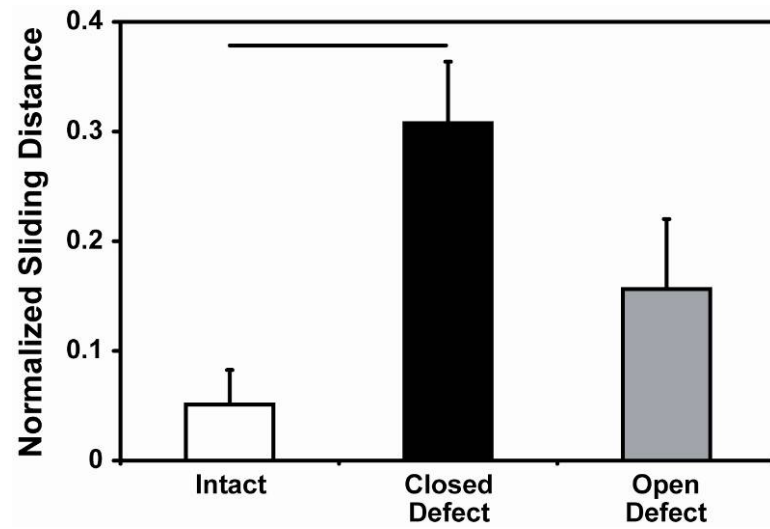


Figure 4.9: Average normalized sliding distance over intact, closed defect, and open defect samples. Sliding distances were averaged over 500 μm surface regions at applied axial compressions of -0.05, -0.10, -0.15, and -0.20, normalized to the applied axial displacement, and averaged for each sample type. (bar: $p < 0.05$) Data are expressed as mean \pm SEM. $n=4$.

4.5 Discussion

This study quantified the changes in dynamic cartilage deformation and sliding in regions near a focal chondral defect (Figure 4.10). The results confirm that defect presence has dramatic effects on dynamic cartilage deformation and suggests that the presence and edge characteristics of defects are likely to influence the sliding between surfaces. During contact between intact surfaces, the superficial region compresses first, with axial strains spreading into deeper tissue regions at higher levels of compression. As a peak displacement is reached and the tissue is allowed to stress relax, magnitudes of strain in the deep regions of the tissue are reduced and redistributed to the middle and superficial tissue regions. Tissue adjacent to a defect experiences increased magnitudes of compressive axial strain, as well as increased lateral and shear strains. During stress relaxation, axial strain distributions return to normal (similar to intact), but elevated shear and lateral tensile strains are maintained. Slightly elevated shear strains and regions of lateral compression are observed in the tissue opposing the defect rim, while strains dissipate in tissue regions over the empty defect area. Increased sliding was seen between surfaces near defects with “closed” orientations, but there was no effect on sliding of defects with “open” orientations. The observed increases in local strain magnitudes and sliding may be relevant to mechanical wear and fatigue processes.

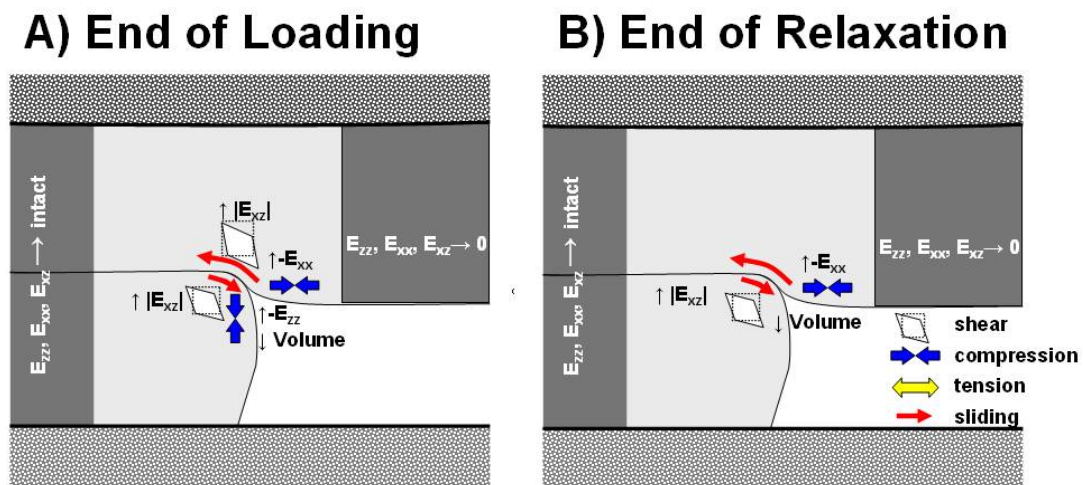


Figure 4.10: Summary of the effects of defects on cartilage mechanics.

The current study optically tracked 2-D intra-tissue strains along the cross-section of opposing surfaces, using methods similar to those employed previously to measure intra-tissue cartilage strains in a variety of loading configurations [3, 21, 35, 36, 38]. It is possible that this 2-D configuration could affect some of the measured strain values. The dissection of cartilage blocks may eliminate some of the residual tangential stresses that could help distribute loads. Furthermore, the geometry of defects in this model does not allow the development of a circumferential hoop stress at the defect rim that might have helped resist deformation.

Samples were loaded in an unconfined geometry, with cartilage depressurization possible through the top and edges of the blocks. This choice is likely to have significant effects on the time-courses of strain development and relaxation measured in both intact and defect-containing samples. While, the *in vivo* boundary conditions are complex, being neither fully confined nor unconfined, the use of an unconfined geometry may be a good approximation of defects where depressurization is allowed because 1) defect size or surface incongruities prevent the opposing surface from sealing along the defect rim, or 2) the subchondral bone is compromised.

The choice of loading protocol may also influence the observed results. In the current study, loading consisted of uniaxial compression, applied in displacement control at a constant strain rate, and with intact and defect-containing samples compressed to the same total bone-to-bone strain. This loading is simplified compared to the *in vivo* environment, which would include both lateral and axial components and where strain and strain rates would depend upon the joint loading during articulation. Samples were experimentally compressed to a common total tissue strain,

to provide a conservative estimate of the effects of defect presence on strain distributions. *In vivo*, significant increases in both total strain and strain rate are also likely. Given this, it is then notable that significant local strain elevations and areas of increased sliding still occurred. The applied strain rate ($1\% \cdot s^{-1}$) was chosen to fall below the threshold known to induce tissue damage, but still provide measurements that are representative of an instantaneous loading response [14, 29]. Since relaxation of the tissue took place quickly, with the majority of changes in strain distributions occurring within the first 6 minutes post-loading, significantly slower strain rates may obscure the dynamic tissue response. It is possible that increased strain rates may accentuate differences between defect and intact cases.

The accuracy of image analysis techniques used here was comparable (in performance on theoretically generated image sets) to that reported previously. Image analysis was performed using a hybrid approach of previous direct point tracking [35, 36] and digital image correlation [3, 38] techniques, developed and implemented in earlier chapters of this dissertation. Here, translations of a subset of cell nuclei, acting as fiducial markers, were tracked by maximizing normalized cross-correlation. Unlike digital image correlation approaches, where correlation is maximized for both translation and deformation of a region and gradient calculations are computed from those deformations, the current approach maximizes only for point displacement and calculates gradients from the relative movement of markers. This allows the results of the correlation steps to be easily verified by manual inspection, but avoids the labor intensive process of directly matching each point.

Depth-dependent distributions of axial compressive strains in intact control samples were similar to previous reports [3, 35, 36, 38], showing significant decreases in strain with increasing tissue depth. The time-course of strain distributions also confirmed differences between the observations reported in Chapter 2 and previous studies: that stress relaxation results in increased strains in the superficial regions and decreased strains in the deep regions. As was the case in Chapter 2, differences in test parameters (e.g. presence or absence of underlying bone, unconfined vs. confined compression, relaxation time, and tissue source) prohibit direct comparison with previous studies. Strain data are reported in the axial and lateral directions, aligned with the physiological orientation of the tissue. At lateral positions away from the defect edge, principal axes were ~aligned with these axes.

The behavior of defect samples in this study was also in general agreement with previous observations. Macroscopic tissue deformation near defects was similar to that described by Braman et al [6], while the slightly lower compression in the tissue opposing the defect rim is consistent with contact stress measurements that peak near, but not at, the defect rim [8]. Intra-tissue strain distributions found here at the post-loading time-point are similar to those observed in Chapter 2.

Increased sliding was experienced at the defect rim of defects with “closed” orientations at all analyzed time-points. Large variability in sliding measurements between individual samples suggest that other factors, such as the surface curvatures may also interact with the defect geometry to control this behavior. Defects with “open” orientations result in little or no increased sliding, but in those configurations the radial edge of the defect may be subject to some amount of sliding; that region of

tissue does not normally experience contact and may be less resistant to wear than tissue along the articular surface. It remains unclear if either of the geometries is physiologically preferable. It is also worth noting, that since sliding distance was related to the applied axial strains, increases in total strain that may be present *in vivo* would also produce increased sliding.

The high level of strain and volume loss present at the defect rim may play a crucial role in the continued progression of a defect. Even under a conservative (equal applied displacement and strain rate) loading protocol, the time-courses of strain development in different regions were affected and local strains exceeded magnitudes previously shown to cause cartilage damage [13, 23, 26, 30, 32 , 37]. It is also possible that persistent mechanical overload could contribute to accelerated rates of wear and fatigue over long-term loading [1], even without eliciting acute tissue damage. Investigation of the changes to defect mechanics under more physiological loading protocols and the physiological changes related to the measured mechanical differences could provide insights into disease progression and identify targets for clinical interventions.

4.6 Acknowledgments

.This chapter will be submitted, in part, for publication in the *Journal of Orthopaedic Research*. The dissertation author is the primary investigator and thanks co-authors Ben Wong and Drs. Won Bae and Robert Sah. This work was supported in part by the National Institutes of Health and the National Science Foundation, and by a grant to the University of California, San Diego, in support of Dr. Robert Sah, from the Howard Hughes Medical Institute through the Professors Program.

4.7 References

1. Ateshian GA, Mow VC: Friction, lubrication, and wear of articular cartilage and diarthrodial joints. In: *Basic Orthopaedic Biomechanics and Mechano-Biology*, ed. by VC Mow, Huiskes R, Lippincott Williams & Wilkins, Philadelphia, 2005, 447-94.
2. Ateshian GA, Wang H: A theoretical solution for the frictionless rolling contact of cylindrical biphasic articular cartilage layers. *J Biomech* 28:1341-55, 1995.
3. Bae WC, Lewis CW, Levenston ME, Sah RL: Indentation testing of human articular cartilage: effects of probe tip geometry and indentation depth on intra-tissue strain. *J Biomech* 39:1039-47, 2006.
4. Bae WC, Schumacher BL, Sah RL: Indentation probing of human articular cartilage: effect on chondrocyte viability. *Osteoarthritis Cartilage* 15:9-18, 2007.
5. Bellucci G, Seedhom BB: Mechanical behaviour of articular cartilage under tensile cyclic load. *Rheumatology (Oxford)* 40:1337-45, 2001.
6. Braman JP, Bruckner JD, Clark JM, Norman AG, Chansky HA: Articular cartilage adjacent to experimental defects is subject to atypical strains. *Clin Orthop Relat Res* 430:202-7, 2005.
7. Brown TD, Anderson DD, Nepola JV, Singerman RJ, Pedersen DR, Brand RA: Contact stress aberrations following imprecise reduction of simple tibial plateau fractures. *J Orthop Res* 6:851-62, 1988.
8. Brown TD, Pope DF, Hale JE, Buckwalter JA, Brand RA: Effects of osteochondral defect size on cartilage contact stress. *J Orthop Res* 9:559-67, 1991.
9. Cicuttini F, Ding C, Wluka A, Davis S, Ebeling PR, Jones G: Association of cartilage defects with loss of knee cartilage in healthy, middle-age adults: a prospective study. *Arthritis Rheum* 52:2033-9, 2005.
10. Clements KM, Bee ZC, Crossingham GV, Adams MA, Sharif M: How severe must repetitive loading be to kill chondrocytes in articular cartilage? *Osteoarthritis Cartilage* 9:499-507, 2001.
11. Curl WW, Krome J, Gordon ES, Rushing J, Smith BP, Poehling GG: Cartilage injuries: a review of 31,516 knee arthroscopies. *Arthroscopy* 13:456-60, 1997.
12. D'Lima DD, Hashimoto S, Chen PC, Colwell CW, Jr., Lotz MK: Human chondrocyte apoptosis in response to mechanical injury. *Osteoarthritis Cartilage* 9:712-9, 2001.
13. D'Lima DD, Hashimoto S, Chen PC, Lotz MK, Colwell CW, Jr.: Cartilage injury induces chondrocyte apoptosis. *J Bone Joint Surg Am* 83-A Suppl 2:19-21, 2001.

14. Frank EH, Grodzinsky AJ: Cartilage electromechanics-I. Electrokinetic transduction and the effects of electrolyte pH and ionic strength. *J Biomech* 20:615-27, 1987.
15. Frank EH, Grodzinsky AJ, Koob TJ, Eyre DR: Streaming potentials: a sensitive index of enzymatic degradation in articular cartilage. *J Orthop Res* 5:497-508, 1987.
16. Guettler JH, Demetropoulos CK, Yang KH, Jurist KA: Osteochondral defects in the human knee: influence of defect size on cartilage rim stress and load redistribution to surrounding cartilage. *Am J Sports Med* 32:1451-8, 2004.
17. Guilak F, Sah RL, Setton LA: Physical regulation of cartilage metabolism. In: *Basic Orthopaedic Biomechanics*, ed. by VC Mow, Hayes WC, Raven Press, New York, 1997, 179-207.
18. Hjelle K, Solheim E, Strand T, Muri R, Brittberg M: Articular cartilage defects in 1,000 knee arthroscopies. *Arthroscopy* 18:730-4, 2002.
19. Jackson DW, Lalor PA, Aberman HM, Simon TM: Spontaneous repair of full-thickness defects of articular cartilage in a goat model. A preliminary study. *J Bone Joint Surg Am* 83-A:53-64, 2001.
20. Jeffrey JE, Gregory DW, Aspden RM: Matrix damage and chondrocyte viability following a single impact load on articular cartilage. *Arch Biochem Biophys* 322:87-96, 1995.
21. Klein TJ, Chaudhry M, Bae WC, Sah RL: Depth-dependent biomechanical and biochemical properties of fetal, newborn, and tissue-engineered articular cartilage. *J Biomech* 40:182-90, 2007.
22. Koh JL, Wirsing K, Lautenschlager E, Zhang LO: The effect of graft height mismatch on contact pressure following osteochondral grafting. A biomechanical study. *Am J Sports Med* 32:317-20, 2004.
23. Kurz B, Jin M, Patwari P, Cheng DM, Lark MW, Grodzinsky AJ: Biosynthetic response and mechanical properties of articular cartilage after injurious compression. *J Orthop Res* 19:1140-6, 2001.
24. Lefkoe TP, Trafton PG, Ehrlich MG, Walsh WR, Dennehy DT, Barrach HJ, Akelman E: An experimental model of femoral condylar defect leading to osteoarthritis. *J Orthop Trauma* 7:458-67, 1993.
25. Lipshitz H, Glimcher MJ: In vitro studies of the wear of articular cartilage. II. characteristics of the wear of articular cartilage when worn against stainless steel plates having characterized surfaces. *Wear* 52:297-339, 1979.
26. Loening A, Levenston M, James I, Nuttal M, Hung H, Gowen M, Grodzinsky A, Lark M: Injurious mechanical compression of bovine articular cartilage induces chondrocyte apoptosis. *Arch Biochem Biophys* 381:205-12, 2000.

27. McKinley TO, McKinley T, Rudert MJ, Koos DC, Pedersen DR, Baer TE, Tochigi Y, Brown TD: Stance-phase aggregate contact stress and contact stress gradient changes resulting from articular surface stepoffs in human cadaveric ankles. *Osteoarthritis Cartilage*, 2005.
28. McKinley TO, Rudert MJ, Koos DC, Pedersen DR, Baer TE, Tochigi Y, Brown TD: Contact stress transients during functional loading of ankle stepoff incongruities. *J Biomech*, 2005.
29. Mow VC, Kuei SC, Lai WM, Armstrong CG: Biphasic creep and stress relaxation of articular cartilage in compression: theory and experiment. *J Biomech Eng* 102:73-84, 1980.
30. Patwari P, Gaschen V, James IE, Berger E, Blake SM, Lark MW, Grodzinsky AJ, Hunziker EB: Ultrastructural quantification of cell death after injurious compression of bovine calf articular cartilage. *Osteoarthritis Cartilage* 12:245-52, 2004.
31. Pena E, Calvo B, Martinez MA, Doblare M: Effect of the size and location of osteochondral defects in degenerative arthritis. A finite element simulation. *Comput Biol Med* 37:376-87, 2007.
32. Quinn TM, Allen RG, Schalet BJ, Perumbuli P, Hunziker EB: Matrix and cell injury due to sub-impact loading of adult bovine articular cartilage explants: effects of strain rate and peak stress. *J Orthop Res* 19:242-9, 2001.
33. Radin EL, Burr DB, Caterson B, Fyhrie D, Brown TD, Boyd RD: Mechanical determinants of osteoarthritis. *Sem Arthritis Rheum* 21:12-21, 1991.
34. Sah RL, Kim YJ, Doong JH, Grodzinsky AJ, Plaas AHK, Sandy JD: Biosynthetic response of cartilage explants to dynamic compression. *J Orthop Res* 7:619-36, 1989.
35. Schinagl RM, Gurskis D, Chen AC, Sah RL: Depth-dependent confined compression modulus of full-thickness bovine articular cartilage. *J Orthop Res* 15:499-506, 1997.
36. Schinagl RM, Ting MK, Price JH, Sah RL: Video microscopy to quantitate the inhomogeneous equilibrium strain within articular cartilage during confined compression. *Ann Biomed Eng* 24:500-12, 1996.
37. Thibault M, Poole AR, Buschmann MD: Cyclic compression of cartilage/bone explants in vitro leads to physical weakening, mechanical breakdown of collagen and release of matrix fragments. *J Orthop Res* 20:1265-73, 2002.
38. Wang CC, Deng JM, Ateshian GA, Hung CT: An automated approach for direct measurement of two-dimensional strain distributions within articular cartilage under unconfined compression. *J Biomech Eng* 124:557-67, 2002.

39. Wang Y, Ding C, Wluka AE, Davis S, Ebeling PR, Jones G, Cicuttini FM: Factors affecting progression of knee cartilage defects in normal subjects over 2 years. *Rheumatology (Oxford)* 45:79-84, 2006.
40. Weightman B: Tensile fatigue of human articular cartilage. *J Biomech* 9:193-200, 1976.
41. Weightman B, Chappell DJ, Jenkins EA: A second study of tensile fatigue properties of human articular cartilage. *Ann Rheum Dis* 37:58-63, 1978.
42. Wilson W, van Burken C, van Donkelaar C, Buma P, van Rietbergen B, Huiskes R: Causes of mechanically induced collagen damage in articular cartilage. *J Orthop Res* 24:220-8, 2006.
43. Wluka AE, Ding C, Jones G, Cicuttini FM: The clinical correlates of articular cartilage defects in symptomatic knee osteoarthritis: a prospective study. *Rheumatology (Oxford)* 44:1311-6, 2005.

CHAPTER 5

BIOMECHANICAL ASSESSMENT OF RETRIEVED TISSUE AFTER IN VIVO CARTILAGE DEFECT REPAIR: TENSILE MODULUS OF REPAIR TISSUE AND INTEGRATION WITH HOST CARTILAGE

5.1 Abstract

Failure to restore the mechanical properties of tissue at the repair site and its interface with host cartilage is a common problem in tissue engineering procedures to repair cartilage defects. Quantitative *in vitro* studies have helped elucidate mechanisms underlying processes leading to functional biomechanical changes. However, biomechanical assessment of tissue retrieved from *in vivo* studies of cartilage defect repair has been limited to compressive tests. Analysis of integration following *in vivo* repair has relied on qualitative histological methods. The objectives of this study were to develop a quantitative biomechanical method to assess 1) the tensile modulus of repair tissue and 2) its integration *in vivo*, as well as determine whether supplementation of transplanted chondrocytes with IGF-I affected these

mechanical properties. Osteochondral blocks were obtained from a previous 8 month study on the effects of IGF-I on chondrocyte transplantation in the equine model. Tapered test specimens were prepared from osteochondral blocks containing the repair/native tissue interface and adjacently-located blocks of intact native tissue. Specimens were then tested in uniaxial tension. The tensile modulus of repair tissue averaged 0.65 MPa, compared to the average of 5.2 MPa measured in intact control samples. Integration strength averaged 1.2 MPa, nearly half the failure strength of intact cartilage samples, 2.7 MPa. IGF-I treatment had no detectable effects on these mechanical properties. This represents the first quantitative biomechanical investigation of the tensile properties of repair tissue and its integration strength in an *in vivo* joint defect environment.

5.2 Introduction

Cartilage normally functions as a low-friction, load-bearing material at the ends of long-bones. When damaged, articular cartilage shows a loss of function and a low intrinsic capability for repair [38]. This problem has motivated a great deal of research into methods of enhancing the repair response [52]. In general, repair of a cartilage defect includes two main processes: 1) filling of the defect with a functional repair tissue and 2) integration of this repair tissue with the surrounding host cartilage and bone.

In vivo studies have assessed the quality of repair tissue resulting from many of the current strategies for cartilage defect repair, including microfracture [9, 58], use of allogenic and autogenic grafts [10, 39, 69], implantation of tissue-engineered constructs [13, 63], and transplantation of cells [11]. Such studies routinely evaluate the quality of repair tissue with quantitative assays of biochemical composition in conjunction with qualitative or semi-quantitative assays of tissue structure (gross observations, histology, and immunohistochemistry). The biomechanical properties of repair tissue can also be characterized, and such properties are dependent on both the composition and structure of the tissue. Compressive properties of *in vivo* repair tissue have been determined through indentation testing [42] or confined compression of retrieved tissue [13]. Although tensile properties of cartilage are more sensitive to growth [65, 66] and aging [2-4, 29] than are compressive properties, no previous studies have characterized the tensile properties of repair tissue retrieved from an *in*

vivo model of defect repair. Determination of these properties in repair tissue may be a sensitive indicator of the efficacy of cartilage defect repair.

The integrative repair between an implant and host cartilage is problematic in a range of orthopaedic treatments. Experimentally created lacerations in the articular surfaces of mature cartilage do not exhibit integrative repair [38], and integration, manifest as collagen fibers crossing the interface, is also absent between surfaces of repair tissue and native cartilage following intrinsic repair of full-thickness defects, even when these surfaces appear well apposed [56]. This lack of integrative repair may eventually lead to degeneration [23, 56]. Most commonly, *in vivo* studies have rated integration using histological scoring systems based on maintained cellularity and continuity of tissue at the interface [20, 44, 55, 62]. Alternatively, *in vitro* studies have been developed to allow quantitative measurement of the integration strength arising at an interface [43, 46, 48]. These tests provide a controlled environment in which to investigate the effects of individual factors on integration, but do not fully simulate the defect environment. To date, no quantitative biomechanical analysis of integrative repair has been performed on tissue retrieved from an *in vivo* model of defect repair.

The continued evaluation and validation of treatment alternatives will rely heavily on analyses of their performance *in vivo*. Repair methods involving chondrocyte transplantation have shown promise and are being adopted for the treatment of full-thickness cartilage defects [11]. This repair strategy may be enhanced through the use of one or more growth factors [14]. Fortier et al. (2002) recently described the effects of insulin-like growth factor-I (IGF-I) on chondrocyte

transplantation in the equine model. Supplementation of transplanted chondrocytes with IGF-I, which is known to stimulate production of proteoglycans and type II collagen *in vitro* [19], was shown to significantly improve the repair response. IGF-I treated defects showed improved filling and chondrogenesis, with more hyaline-like repair tissue and increased levels of type II collagen. The presence of IGF-I also resulted in improved histological scores of integration with host cartilage.

The objectives of the current study were to further analyze the tissue retrieved from this equine study, focusing on biomechanical properties. The specific aims were to develop a quantitative biomechanical method to assess 1) the tensile modulus of the repair tissue and 2) its integration *in vivo* with native host tissue, and also to determine whether supplementation of transplanted chondrocytes with IGF-I affected these mechanical properties.

5.3 Materials and Methods

Cartilage Defect Repair

Test samples were obtained from a previous study investigating the effects of IGF-I on the *in vivo* repair of cartilage defects. A complete description of this study is in [20]. Briefly, the study was conducted on 8 young adult (3-5 yr old) horses using procedures approved by the IACUC (Cornell and UCSD). Each horse underwent bilateral arthroscopic procedures to repair single 15 mm diameter, cylindrical defects, created on the lateral trochlear ridge of each patellofemoral joint. The defects were full thickness and included removal of most, but not all, of the calcified cartilage layer. One joint in each animal, serving as a control, was repaired by transplantation of 20 million allogenic chondrocytes, cryopreserved from 3-9 month foals and suspended in 1 ml of equine fibrinogen solution (200 mg/ml). The contralateral joint was repaired similarly, but with the addition of 25 μ g rhIGF-I to the fibrinogen solution. Animals were sacrificed at 8 months. Two osteochondral blocks (~15 mm long x 3 mm wide) were harvested from each knee, wrapped in plastic wrap, immersed in phosphate buffered saline (PBS), and stored at -80°C until testing. One was an “integration” block, containing the repair/native tissue interface. The other was an adjacently-located block of native tissue.

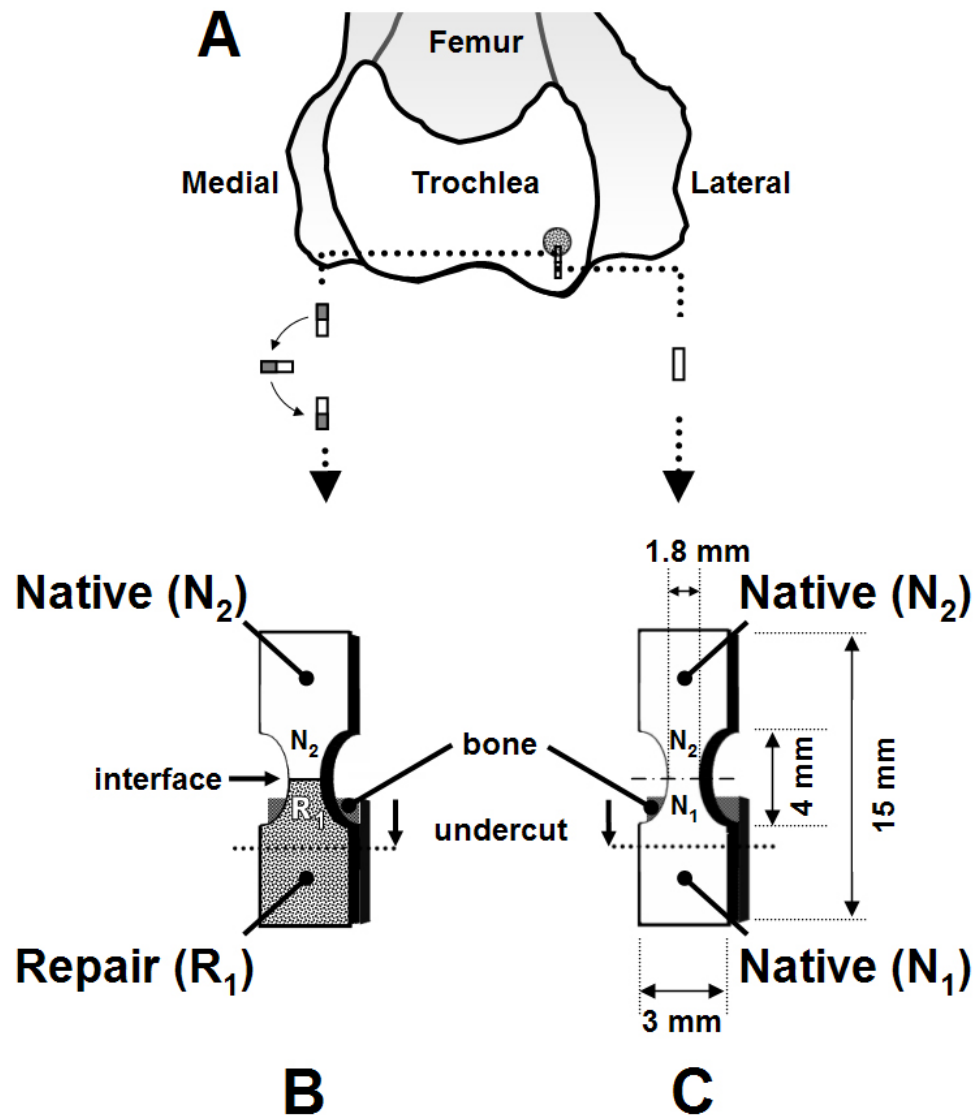


Figure 5.1: Diagram of harvest locations and specimen geometry. (A) Defects were located on the lateral trochlear ridge of each patellofemoral joint. Two osteochondral blocks were harvested from each joint: a block containing the repair/native tissue interface and an adjacent block of native cartilage. Blocks were prepared to create “integration” samples (B), with regions of repair (R₁) and native (N₂) tissue, and “intact control” (N₁-N₂) samples (C), each with a tapered gage region.

Biomechanical Testing

Sample preparation

One tensile sample was prepared from each osteochondral block immediately before testing (Figure 5.1). For integration (R_1 - N_2) samples, the interface marked the border between regions 1 (repair tissue, R_1) and 2 (native cartilage, N_2). For intact controls (N_1 - N_2), regions 1 (N_1) and 2 (N_2) were randomly assigned to the two halves of the block, each consisting of native cartilage. Blocks were thawed by immersion in PBS + proteinase inhibitors (PI; 1 mM phenylmethanesulfonyl fluoride, 2 mM disodium ethylenediamine tetraacetate, 5 mM benzamidine-HCl, and 10 mM N-ethylmaleimide) [22]. The interface region (center) of each integration (intact control) sample was grossly visualized, and a tapered tensile specimen with a 1.8 mm wide, 4 mm long gage region, manually centered at this point, was punched into the cartilage [31]. The N_2 and gage regions were undercut in the cartilage and/or repair tissue just above the bone, using a scalpel. The bone lying beneath these regions was removed and discarded. The region 1 tissue lying outside of the gage region remained attached to a layer of bone, which was trimmed to a thickness of 0.5-1.0 mm. Parallel bands were marked at ~1 mm intervals on the articular surface of the gage region [31, 50] using Trypan Blue. The stain was applied using a custom stamp, consisting of 5 parallel threads (0.1 mm diameter) held at 1 mm intervals. A total of 13 integration samples and 12 intact control samples were prepared and tested.

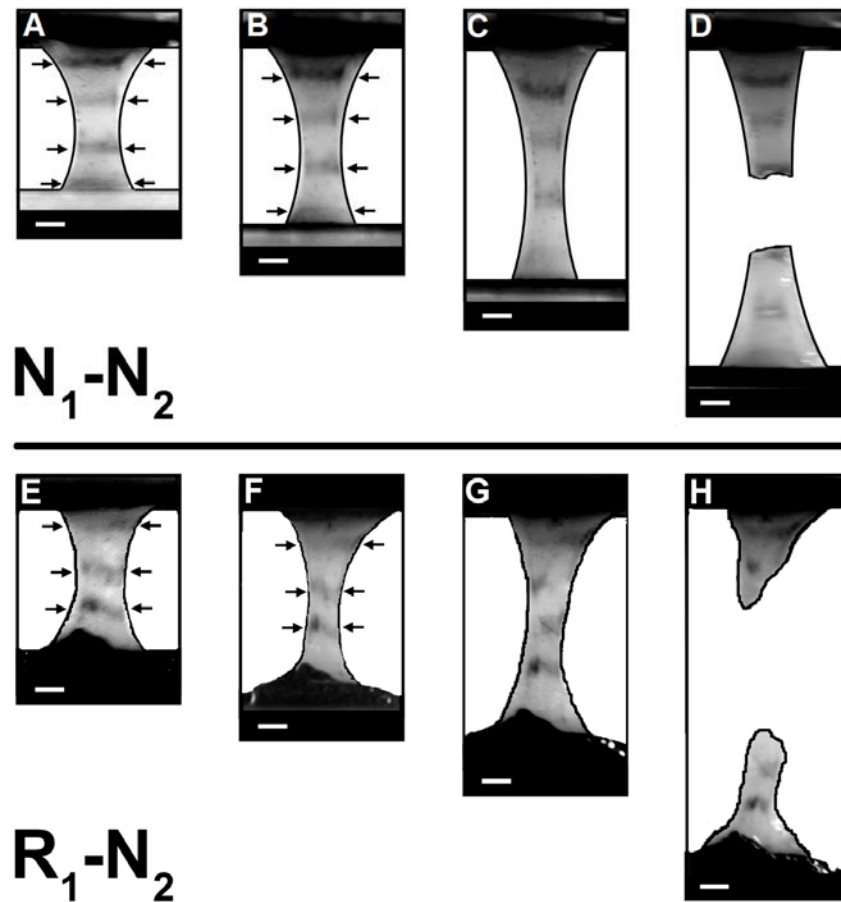


Figure 5.2: Sequential images of representative intact control (N_1 - N_2) and integration (R_1 - N_2) samples during tensile testing. Each sample is shown (A,E) at tare load, (B,F) after relaxation at 20% elongation, (C,G) during constant-rate extension, and (D,H) after failure. Regions of the articular surface were stained with Trypan Blue and used to track sample deformation. Vertical positions of stained bands in analyzed images (A,B,E,F) are identified on both sides by arrows. The interface of R_1 - N_2 , visualized grossly, was located within the center band; during constant rate extension the interface began to pull apart, resulting in the splitting of this band (G). Strains were computed for regions above and below the interface (or the center of intact controls), but away from the grips. Bar = 1 mm.

Tensile Testing

Following preparation, each specimen was tested in tension. The thickness of the gage region was measured on each side of the center/interface using a contact sensing micrometer; individual thickness measurements on a sample varied $< 10\%$, and an average value was used for all subsequent calculations. The sample was then clamped into a computer-controlled, uniaxial test instrument with an initial clamp-to-clamp distance of 5 mm. Spacers measuring $\sim 50\%$ of the sample thickness were placed into each clamp to limit tissue compression. The sample was run through a standard test cycle, and load and displacement were recorded. Sample hydration was maintained during testing by continuous circulation of PBS + PI. The sample was extended at 0.5 mm/min until reaching a tare load (0.08 N for R_1 - N_2 , 0.20 N for N_1 - N_2), extended at a strain rate of 0.25%/s to first 10% and then 20% elongation (~ 0.5 mm and 1 mm respectively) and allowed, at each position, to stress relax to equilibrium (900 s), and finally, pulled to failure at a constant rate of 5 mm/min [31, 65]. Failure was defined as the point of maximum load and generally corresponded to the initiation of a visible tear in the cartilage. Digital images of the sample were taken prior to testing, at tare, following the stress relaxations at 10% and 20% elongation, and at several points during the pull to failure (Figure 5.2).

Image Analysis

Sequential images were analyzed to determine strain development in different regions of the sample (Figure 5.3). Image pairs (at tare load and following relaxation at 20% elongation) were analyzed with a custom program using the image processing toolbox in Matlab Release 13 (The Mathworks, Inc., Natick, MA). Unique regions of

interest (ROI's), comprised of the stained bands on the articular surface, were chosen manually in the reference image and matched with corresponding regions in the deformed image. A series of 2-D correlations between each ROI and equally-sized regions in the deformed image was performed. The coordinates of the region that resulted in the highest correlation were determined. The coordinate change from the reference image represented the translation of the ROI. Next, each ROI was subjected to incremental, known deformations and correlated to the deformed image at the previously determined coordinates. The deformations resulting in the highest correlation were determined. This process of translation and deformation was repeated until maximum correlation was achieved. Correlation coefficients for ROI's of well-focused image pairs were typically ~ 0.9 (on a scale of 0-1). In certain cases, problems with image acquisition (described below) resulted in much lower correlation coefficients (< 0.5), and these cases were excluded from the analysis (discussed below). The results of each analysis were viewed manually and checked for errors. The distances between centerlines of adjacent ROI's were calculated in the reference and deformed images, and strains were calculated as change in length over initial length. Strains were determined for portions of regions 1 (ϵ_1) and 2 (ϵ_2) not directly adjacent (~ 0.5 mm away from the clamps at tare) to the clamps, where strains within a given tissue region (i.e. native or repair) were relatively uniform (standard deviation of strain between regions being $< 3\%$ for intact controls, data not shown).

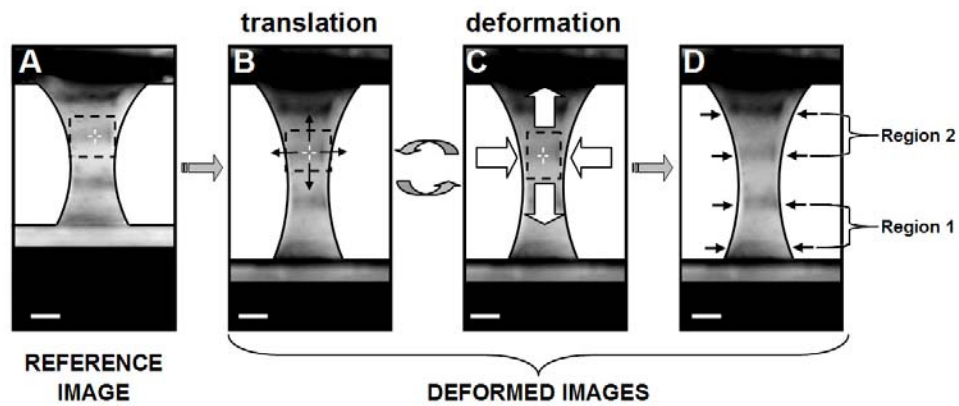


Figure 5.3: Correlation analysis of digital strain images. Regions of interest (ROI) were selected from the reference image (**A**). 2-D correlation of each ROI with the deformed image was performed and the coordinates of highest correlation recorded (**B**). Each ROI was then deformed incrementally and correlated with the deformed image at the determined coordinates (**C**). Translation and deformation were repeated until maximum correlation was achieved. Strains were computed for regions 1 and 2 of the sample, using relative translations of stained regions (**D**). Bar = 1 mm.

Data Analysis

Load and displacement data were used to calculate tensile properties. Stress was calculated as the load over the initial cross-sectional area in the center of the gage region. Sample elongation (for description of the point of failure) was calculated as displacement over the between-clamp distance at tare load (since images were taken at selected time points and did not include the point of failure). The strength and elongation at failure were taken at the point of maximum load. The stress following the relaxation phase at 20% elongation was computed as an index of the overall tensile modulus of the sample. Equilibrium tensile modulus was calculated in different regions by dividing the stress at 20% elongation by the strains determined from image analysis. While the width of the sample changes slightly along its length, the average stress in areas where strain was calculated was within 5-10% of the stress in the gage center.

Statistics

Data are presented as mean \pm SEM. The mean, SEM, and statistical analysis of strain ratios were calculated using log-transformed data (to improve normality). For display purposes, the geometric mean (inverse of the mean of log-transformed values) and the equivalent SEM are reported (Figure 5.5A). Results were analyzed by one-way or two-way ANOVA ($\alpha=0.05$), using Systat 10.2 (Systat Software, Inc., Richmond, CA).

5.4 Results

The repair tissue in all samples appeared to have fully filled the defect. The interface between native and repair tissues was visible from both the top and sides of the osteochondral block; however, the tissue thickness was relatively uniform throughout the gage region. These qualitative observations were confirmed by thickness measurements taken in the gage regions of test samples, which showed no significant differences between sample groups (Figure 5.4A).

Differences between groups were present in indices of tensile modulus. Grossly, the repair tissue appeared “softer” and was more easily deformed than the native cartilage, in agreement with tensile measurements. Tensile stress at 20% elongation, an indicator of total sample modulus, was significantly lower in integration samples than in intact controls (Figure 5.4B, $p < 0.005$). The average value of stress in integration samples at 20% elongation was 0.11 ± 0.02 MPa, approximately half that of intact controls, which averaged 0.23 ± 0.03 MPa. There was not, however, a discernable difference in modulus between samples retrieved from joints with or without IGF-I supplementation ($p = 0.28$), nor was there an interaction effect between sample type and IGF-I treatment ($p = 0.52$).

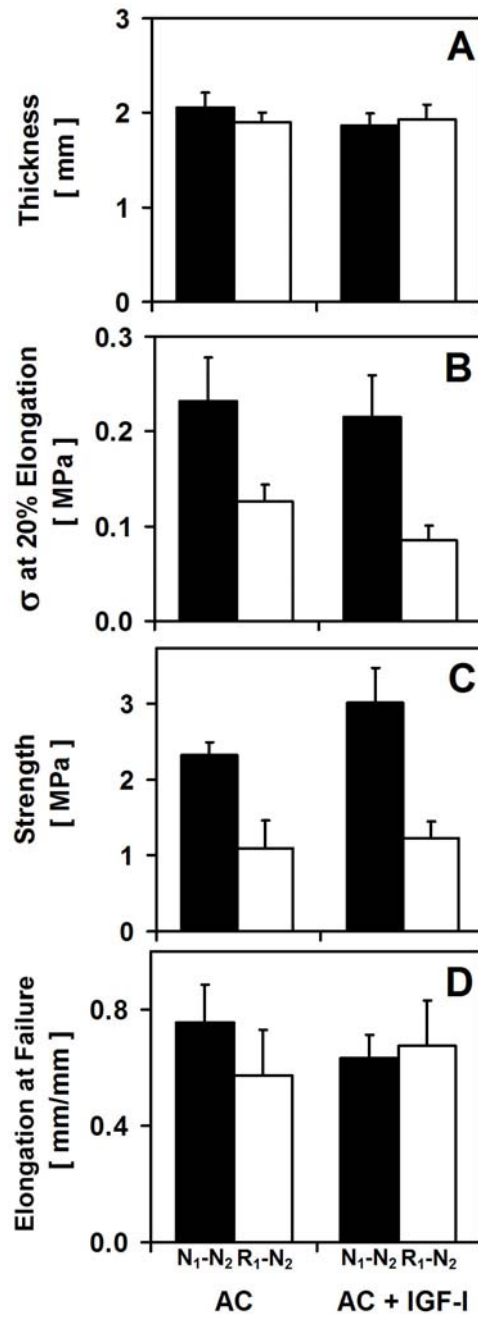


Figure 5.4: Properties of intact control (Native-Native, N₁-N₂) and integration (Repair-Native, R₁-N₂) samples in joints repaired with allogenic chondrocytes alone (AC) or supplemented with IGF-I (AC + IGF-I). Mean ± SEM, n=5-7.

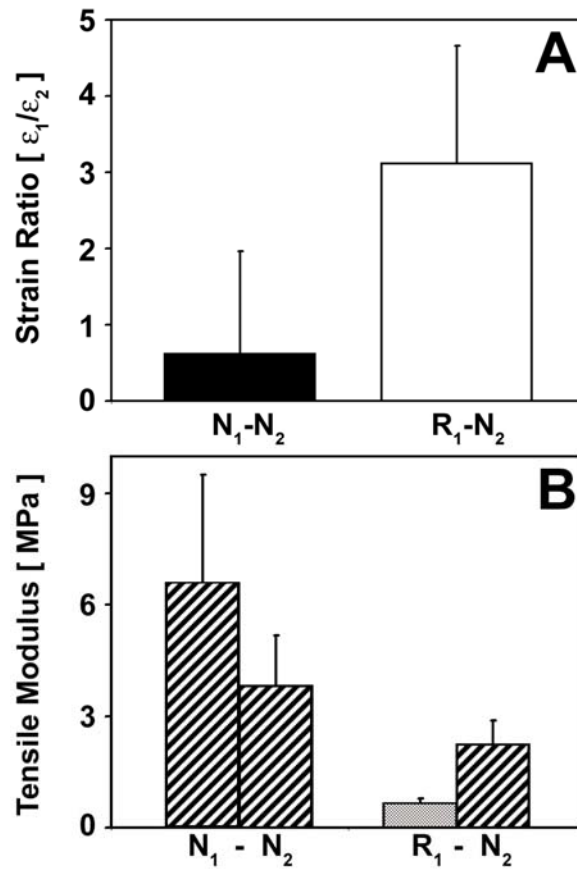


Figure 5.5: Analysis of strain distribution (A) and tensile moduli (B) for intact control (Native-Native, N1-N2) and integration (Repair-Native, R1-N2) samples. For (B), bars represent moduli of individual, repair (R1) or native tissue (N1, N2), regions of samples. Mean \pm SEM, n=5-6.

The difference in moduli between integration and native samples was further described by analysis of strains in individual regions of tensile specimens. Because of faint staining and/or out-of-focus photos, images were not well-correlated for some samples, and strains could only be calculated for approximately half of the tested samples (6/13 integration samples and 5/12 intact controls). This affected only image analysis, and all other analyses (Figure 5.4) include data from every integration and control sample. The results of strain image analysis were separated based on sample type only and included defects treated with or without IGF-I. Strain analysis showed that regions of repair tissue experienced approximately three times the strain of the adjoining native cartilage in integration samples. At 20% total sample elongation, the average strain in repair regions of integration samples was $19 \pm 3\%$, compared to $8 \pm 3\%$ in the adjoining native cartilage and $6 \pm 1\%$ and $9 \pm 2\%$ for native cartilage in regions 1 and 2 of intact control samples, respectively. The ratio of strain between the repair (R_1) and native (N_2) regions of integration samples, 3.1 ± 1.6 , was significantly greater than that of equivalent regions (N_1 , N_2) of intact controls, 0.6 ± 1.3 (Figure 5.5A, $p < 0.05$). This difference between repair and native tissues was even greater when comparing the tensile moduli of the regions (Figure 5.5B). Analysis showed significantly lower moduli in R_1 - N_2 samples ($p < 0.05$) and a significant interaction between region and sample type ($p < 0.05$), but no effect of IGF-I treatment ($p = 0.32$). The tensile modulus of repair tissue, 0.64 ± 0.14 MPa, was ~30% that of the adjoining native cartilage in integration samples, 2.2 ± 0.7 MPa, and less than 20% that of intact control cartilage, 5.2 ± 1.6 MPa.

The differences between integration and intact control samples were also evident in the failure properties. The interface strengths of integration samples, 1.2 ± 0.2 MPa, were significantly lower (by ~60%) than the tensile strengths of intact controls, 2.6 ± 0.3 MPa (Figure 5.4C, $p < 0.001$). The sample strengths, however, were not affected by the presence of IGF-I ($p = 0.14$), and there was no significant interaction between sample type and IGF-I treatment ($p = 0.37$). The value of elongation at failure, $66 \pm 5\%$, was not significantly affected by any factor or interaction of factors (Figure 5.4D, $p > 0.32$). All integration samples failed at the repair/native tissue interface and most (10/12) intact control samples failed in the gage region. Failure of intact control samples typically started in the superficial zone and extended to the deeper cartilage.

5.5 Discussion

A quantitative biomechanical test capable of measuring the tensile modulus and integration strength of repair tissue generated *in vivo* was developed. This represents the first investigation of these properties in tissue retrieved from an *in vivo* joint defect model. The equilibrium tensile modulus (Figure 5.5B) of repair tissue averaged 0.64 MPa, compared to 5.2 MPa for intact controls. The values of integration strength (Figure 5.4C) averaged 1.2 MPa, or roughly half the tensile strength of intact cartilage samples. IGF-I supplementation had no detectable effect on the tensile properties of the repair tissue or on its integration with the native cartilage at the 8 month post-operative time point.

Mechanical testing was performed using a sample geometry (Figure 5.1) based on that used traditionally in tensile tests of cartilage [31]. While this orientation may not represent physiological loading conditions, several studies have demonstrated the importance of tensile properties in the function of cartilage. Mathematical models have illustrated the significance of the “trampoline effect” of tensile stresses in the superficial zone in resistance of compressive loads [16]. Following compressive fatigue loading, a weakening of cartilage tensile properties precedes visible surface damage [40], and it has been suggested that failure of cartilage under high indentation loads is due to the induced tensile strains (and tensile tissue properties) near the surface, rather than the induced compressive strains (and compressive tissue properties) [18]. The tensile geometry also uses just a portion of the interface, preserving a large amount of tissue for other analyses. However, as in histological analyses, attention must be paid in selection of a sample that is representative of the overall integration along the defect perimeter.

Unlike traditional tensile tests of articular cartilage [31], the samples in this study were full-thickness, having a combination of superficial-deep zones. The use of full-thickness samples was necessary because the samples tested were not flat enough to allow sequential sections to be easily taken. This “thick” sample provided a larger interfacial area than traditional tensile test samples and presumably gave a more representative value of overall integration strength. The use of such a thick, short specimen is not ideal from a mechanical testing standpoint and increases the likelihood that stress concentrations from the clamps will extend into parts of the gage region. However, limitations in joint and defect size make the creation of longer

samples impractical. The use of full-thickness samples probably also accounts for the failure behavior of the intact control samples, which initiated in the superficial region. This finding is consistent with the superficial cartilage typically having a lower strain to failure than cartilage from deeper zones [31]. The inclusion of bone beneath the repair tissue, to facilitate sample gripping, may also serve to limit disturbance of the interface during sample preparation.

Strain was tracked in digital images of samples to improve the accuracy of tensile modulus calculations and allow for strain and modulus to be determined for individual regions of a sample. The values of total sample elongation calculated using the change in clamp-to-clamp distance were typically higher than the strains in the center of the sample calculated by image analysis. A “straightening” of slightly curved samples or slipping at the clamps during the initial loading period likely contributed to this difference. This presumably resulted in lower values of stress at 20% elongation (Figure 5.4B) than would be recorded for samples experiencing 20% strain in center of the gage region. Although a direct comparison of the two methods for strain determination could not be made at failure, the reported values of elongation at failure may also overestimate the strains present in the gage region at failure.

The results of the digital image analysis are presented with pooled data from groups with and without IGF-I supplementation. Several practical issues, concerning both staining procedure and image acquisition, resulted in fewer samples being used for strain analysis. Precise staining of the sample proved difficult. Trypan Blue was selected for its permanence, but the uneven surface of the repair tissue and interface, coupled with the fluid’s low viscosity, often led to “running” of the stain. In these

cases, the surface lacked the discrete marks needed for tracking. In other cases, the staining, while grossly visible, was too faint to accurately track in images. Complications also arose during image acquisition. Inexact auto-focusing of the camera, leading to slightly out-of-focus images, and surface glare (from the lighting) disrupted correlation of some images. Sample exclusion appeared to be due to practical issues of sample staining and image acquisition and was independent of the relative strength/weakness of the sample ($p=0.858$). Despite these difficulties, acceptable image pairs were obtained for 6/13 integration samples and 5/12 intact controls. Pooling of data from groups with/without IGF-I was performed because there were no differences observed between the load-displacement relationships of these groups (Figure 5.4). This arrangement allowed for a large enough sample size to perform meaningful statistical analysis.

The tensile properties measured in intact control samples compare well with those obtained from traditional tensile tests of thin (300 μm) slices of normal equine cartilage (including the intact articular surface) and helped validate the experimental setup. The values of equilibrium tensile modulus and ultimate tensile strength measured here (5.2 MPa and 2.7 MPa, respectively) were lower than those of superficial samples (7.7 MPa and 10.7 MPa, respectively) [37], but on the same order of magnitude. These lower values appear largely attributable to the difference in sample thicknesses, because the superficial region is known to have higher strength and stiffness than deeper zones of cartilage in skeletally mature animals [31, 50]. These deeper zones make up 80-90% of the full thickness samples used in this study. Since elongation at failure is typically lowest in the superficial region of mature

cartilage [31, 50], where stress develops more quickly due to the higher stiffness, no difference is apparent between values of elongation at failure recorded in the current, 0.70, and previous, 0.71 [21], studies. Animal age, exercise regimen, split-line orientation, and harvest site differences may have also contributed to the variation. Both of these studies were performed on cartilage samples following frozen storage. Freezing has been suggested to have negligible effects on the mechanical properties of both human and bovine articular cartilage [8, 32, 33, 60].

The presence of IGF-I during repair appears to have had no effect on the development of integration strength or tensile modulus, despite its ability to generate repair tissue closer in composition to native cartilage and improve histological scores of integration [20]. While the composition of repair tissue is an important contributor to its mechanical properties, structural properties, such as surface continuity and collagen orientation, also influence certain mechanical properties, including tensile strength (described here) and indentation stiffness near an interface [6]. Histological examinations are useful in the analysis of integration, as surfaces that are separate cannot be bound together, but the results of the present study suggest that the appearance of the interface alone may not be sufficient to predict integration strength. It is possible that histological methods are more sensitive to levels of repair tissue formation and defect filling, rather than the mechanical integration between apposing surfaces.

This is the first biomechanical investigation of the tensile modulus of repair tissue and its integration strength with host cartilage *in vivo*. Determination of these mechanical properties is important because inadequate strength at the defect site or its

interface is likely to contribute to the degeneration seen at later time points of repair[33]. The values of integration strength seen here were still less than half the tensile strength of normal articular cartilage but were significantly higher than those measured in shorter-term *in vitro* studies [43, 46, 48]. The methods introduced here can be used to assess and compare alternative treatments for cartilage repair.

5.6 Acknowledgments

This chapter is published, in full, in the *Journal of Biomechanics*, volume 39, issue 1, January 2006. The dissertation author is the primary investigator and thanks co-authors Van Wong and Drs. Albert Chen, Lisa Fortier, Alan Nixon, and Robert Sah. This work was supported by the Arthritis Foundation, Harry M Zweig Foundation, Institute for Sports Medicine Research, NASA, NIH, NSF, and the Office for Naval Research (NDSEG Fellowship to KRG).

5.7 References

1. Akizuki S, Mow VC, Muller F, Pita JC, Howell DS, Manicourt DH: Tensile properties of human knee joint cartilage: I. influence of ionic conditions, weight bearing, and fibrillation on the tensile modulus. *Journal of Orthopaedic Research* 4:379-92, 1986.
2. Akizuki S, Mow VC, Muller F, Pita JC, Howell DS, Manicourt DH: Tensile properties of human knee joint cartilage: II. correlations between weight bearing and tissue pathology and the kinetics of swelling. *Journal of Orthopaedic Research* 5:173-86, 1987.
3. Armstrong CG, Mow VC: Variations in the intrinsic mechanical properties of human articular cartilage with age, degeneration, and water content. *Journal of Bone and Joint Surgery (Am)* 64-A:88-94, 1982.
4. Bae WC, Law AW, Amiel D, Sah RL: Sensitivity of indentation testing to step-off edges and interface integrity in cartilage repair. *Ann Biomed Eng* 32:360-9, 2004.
5. Black J, Shadle CA, Parsons JR, Brighton CT: Articular cartilage preservation and storage. II. mechanical indentation testing of viable, stored articular cartilage. *Arthritis Rheum* 22:1102-8, 1979.
6. Blevins FT, Steadman JR, Rodrigo JJ, Silliman J: Treatment of articular cartilage defects in athletes: an analysis of functional outcome and lesion appearance. *Orthopedics* 21:761-8, 1998.
7. Bobic V: Arthroscopic osteochondral autograft transplantation in anterior cruciate ligament reconstruction: a preliminary clinical study. *Knee Surgery, Sports Traumatology, Arthroscopy* 3:262-4, 1996.
8. Brittberg M, Lindahl A, Nilsson A, Ohlsson C, Isaksson O, Peterson L: Treatment of deep cartilage defects in the knee with autologous chondrocyte transplantation. *New England Journal of Medicine* 331:889-95, 1994.
9. Chu CR, Douchis JS, Yoshioka M, Sah RL, Coutts RD, Amiel D: Osteochondral repair using perichondrial cells: a one year study in rabbits. *Clinical Orthopaedics* 340:220-9, 1997.
10. Coutts RD, Sah RL, Amiel D: Effect of growth factors on cartilage repair. *Instructional Course Lectures* 46:487-94, 1997.

11. Donzelli PS, Spilker RL, Ateshian GA, Mow VC: Contact analysis of biphasic transversely isotropic cartilage layers and correlations with tissue failure. *J Biomech* 32:1037-47, 1999.
12. Flachsman R, Broom ND, Hardy AE: Deformation and rupture of the articular surface under dynamic and static compression. *J Orthop Res* 19:1131-9, 2001.
13. Fortier LA, Lust G, Mohammed HO, Nixon AJ: Coordinate upregulation of cartilage matrix synthesis in fibrin cultures supplemented with exogenous insulin-like growth factor-I. *Journal of Orthopaedic Research* 17:467-74, 1999.
14. Fortier LA, Mohammed HO, Lust G, Nixon AJ: Insulin-like growth factor-I enhances cell-based repair of articular cartilage. *The Journal of Bone and Joint Surgery (BR)* 84:276-88, 2002.
15. Frank EH, Grodzinsky AJ, Koob TJ, Eyre DR: Streaming potentials: a sensitive index of enzymatic degradation in articular cartilage. *Journal of Orthopaedic Research* 5:497-508, 1987.
16. Ghadially FN, Thomas I, Oryszak AF, LaLonde J-MA: Long term results of superficial defects in articular cartilage. A scanning electron microscope study. *Journal of Pathology* 121:213-7, 1977.
17. Kempson GE: Relationship between the tensile properties of articular cartilage from the human knee and age. *Annals of the Rheumatic Diseases* 41:508-11, 1982.
18. Kempson GE, Muir H, Pollard C, Tuke M: The tensile properties of the cartilage of human femoral condyles related to the content of collagen and glycosaminoglycans. *Biochimica et Biophysica Acta* 297:456-72, 1973.
19. Kempson GE, Spivey CJ, Swanson SA, Freeman MA: Patterns of cartilage stiffness on normal and degenerate human femoral heads. *J Biomech* 4:597-609, 1971.
20. Kiefer GN, Sunbdy K, McAllister D, Shrive NG, Frank CB, Lam T, Schachar NS: The effect of cryopreservation on the biomechanical behavior of bovine articular cartilage. *J Orthop Res* 7:494-501, 1989.
21. Lewis CW, Williamson AK, Chen AC, Bae WC, Temple MM, Wong VW, Nugent GE, Harmel JL, Walker JE, James SP, Wheeler DL, Sah RL, Kawcak CE: Relationship between functional demand, subchondral bone mineral density, and articular cartilage structural and integrity. *Trans Orthop Res Soc* 30:1550, 2005.
22. Mankin HJ: The response of articular cartilage to mechanical injury. *The Journal of Bone and Joint Surgery (Am)* 64-A:460-6, 1982.

23. Matsusue Y, Yamamuro T, Hama H: Arthroscopic multiple osteochondral transplantation to the chondral defect in the knee associated with anterior cruciate ligament disruption. *Arthroscopy* 9:318-21, 1993.
24. McCormack T, Mansour JM: Reduction in tensile strength of cartilage precedes surface damage under repeated compressive loading in vitro. *J Biomech* 31:55-61, 1998.
25. Mow VC, Ratcliffe A, Rosenwasser MP, Buckwalter JA: Experimental studies on repair of large osteochondral defects at a high weight bearing area of the knee joint: a tissue engineering study. *Journal of Biomechanical Engineering* 113:198-207, 1991.
26. Obradovic B, Martin I, Padera RF, Treppo S, Freed LE, Vunjak-Novakovic G: Integration of engineered cartilage. *Journal of Orthopaedic Research* 19:1089-97, 2001.
27. O'Driscoll SW, Keeley FW, Salter RB: The chondrogenic potential of free autogenous periosteal grafts for biological resurfacing of major full-thickness defects in joint surfaces under the influence of continuous passive motion. An experimental investigation in the rabbit. *The Journal of Bone and Joint Surgery (Am)* 68:1017-35, 1986.
28. Peretti GM, Bonassar LJ, Caruso EM, Randolph MA, Trahan CA, Zaleske DJ: Biomechanical analysis of a chondrocyte-based repair model of articular cartilage. *Tissue Engineering* 5:317-26, 1999.
29. Reindel ES, Ayroso AM, Chen AC, Chun DM, Schinagl RM, Sah RL: Integrative repair of articular cartilage *in vitro*: adhesive strength of the interface region. *Journal of Orthopaedic Research* 13:751-60, 1995.
30. Roth V, Mow VC: The intrinsic tensile behavior of the matrix of bovine articular cartilage and its variation with age. *The Journal of Bone and Joint Surgery (Am)* 62-A:1102-17, 1980.
31. Sah RL, Klein TJ, Schmidt TA, Albrecht DR, Bae WC, Nugent GE, McGowan KB, Temple MM, Jadin KD, Schumacher BL, Chen AC, Sandy JD: Articular cartilage repair, regeneration, and replacement. In: *Arthritis and Allied Conditions: A Textbook of Rheumatology*, ed. by WJ Koopman, Lippincott Williams & Wilkins, Philadelphia, 2005, 2277-301.
32. Sellers RS, Peluso D, Morris EA: The effect of recombinant human bone morphogenetic protein-2 (rhBMP-2) on the healing of full-thickness defects of articular cartilage. *The Journal of Bone and Joint Surgery (Am)* 79-A:1452-63, 1997.

33. Shapiro F, Koide S, Glimcher M: Cell Origin and Differentiation in the Repair of Full-Thickness Defects of Articular Cartilage. *The Journal of Bone and Joint Surgery (Am)* 75-A:532-53, 1993.
34. Steadman JR, Rodkey WG, Briggs KK, Rodrigo JJ: Die technik der mikrofrakturierung zur behandlung von kompletten knorpeldefekten im kniegelenk. *Der Orthopade* 28:26-32, 1999.
35. Swann AC, Seedhom BB: The stiffness of normal articular cartilage and the predominant acting stress levels: implications for the aetiology of osteoarthritis. *Br J Rheum* 32:16-25, 1993.
36. Wakitani S, Goto T, Pineda SJ, Young RG, Mansour JM, Caplan AI, Goldberg VM: Mesenchymal cell-based repair of large, full-thickness defects of articular cartilage. *The Journal of Bone and Joint Surgery (Am)* 76-A:579-92, 1994.
37. Wakitani S, Kimura T, Hirooka A, Ochi T, Yoneda M, Yasui N, Owaki H, Ono K: Repair of rabbit articular surfaces with allograft chondrocytes embedded in collagen gel. *The Journal of Bone and Joint Surgery (Br)* 71-B:74-80, 1989.
38. Williamson AK, Chen AC, Masuda K, Thonar EJ-MA, Sah RL: Tensile mechanical properties of bovine articular cartilage: variations with growth and relationships to collagen network components. *Journal of Orthopaedic Research* 21:872-80, 2003.
39. Williamson AK, Chen AC, Sah RL: Compressive properties and function-composition relationships of developing bovine articular cartilage. *Journal of Orthopaedic Research* 19:1113-21, 2001.
40. Yamashita F, Sakakida K, Suzu F, Takai S: The transplantation of an autogeneic osteochondral fragment for osteochondritis dissecans of the knee. *Clinical Orthopaedics* 201:43-50, 1985.

CHAPTER 6

CONCLUSIONS

6.1 Summary and Significance of Findings

The work in this dissertation contributed to the understanding of normal cartilage contact and its changes near areas of focal damage. During uniaxial compression of opposing, intact cartilage slabs, strain builds up first in the superficial most layers of cartilage. As compression is continued, axial compressive strains extend into the middle and deep zones of cartilage while strain magnitudes continue to increase in the superficial region. When loading is stopped and held in the compressed position, magnitudes of strain in the deeper regions decrease as more strain is distributed to the superficial and middle regions. For relatively flat surfaces, little sliding occurs during loading, with the majority of sliding that does take place occurring during the initial phase of loading as the surfaces are coming into contact.

Cartilage surfaces adjacent to and opposing a focal defect experience higher magnitudes of strain than intact surfaces under the same applied displacements. Cartilage in the superficial and middle regions of the adjacent surface experienced increases in local compressive axial strain magnitudes of more than 0.10 and magnitudes of lateral tensile strains and shear at > 2-fold those of intact controls. The

opposing, intact cartilage surface experienced sharp increases in shear strain (~6-fold over intact controls) in the region directly opposing the defect rim and alternating regions of tension and compression in the lateral (parallel to the articular surface) direction. Axial strain distributions were approximately normal in regions contacting the cartilage adjacent to the defect, but eventually dissipated in areas over the empty defect.

Similar strain distributions were measured in both human and bovine tissue samples. Most changes occurred in the superficial or upper-middle zones of the tissue, with changes near the bone uncommon. It is noteworthy that significant increases in local strain magnitudes were measured even with the use of a conservative loading protocol, where total applied displacement was equal in intact and defect-containing groups. Application of more physiological loading protocols (i.e. including a component of motion in the lateral direction) may produce more widespread effects of defect presence.

Sliding between the opposing surfaces was also increased in the presence of a focal defect. In all cases, the adjacent cartilage surface moved toward the defect with respect to the opposing surface during loading, as the tissue expanded laterally into the empty defect region. Following loading, there was a slight reversal of sliding as the adjacent cartilage recovered slightly, drawing back from the defect. The total sliding distance was at least partially mediated by the angle of the defect edge, with open angles tending to inhibit sliding and closed angles encouraging sliding.

Although the sliding distance induced by compressive loading of a defect is significantly shorter than the total contact length during a cycle of joint articulation, it

may still be a significant portion of the sliding path length experienced at any single point. Normal joint articulation exposes the articular surfaces to a mixture of sliding and rolling, with the contact point traveling along both articulating surfaces; this means that the magnitude of sliding experienced at a given point on the surface could be considerably less than the total path length. Here, lateral sliding of $\sim 100\ \mu\text{m}$ (in human samples) was induced by a conservative loading protocol. The point of maximum contact translates along the surface of the condyle during articulation, while the contact point moves significantly less on the tibial plateau. Thus, typical points on tibial plateau might experience sliding equal to nearly the entire sliding path length, which could be estimated at $\sim 5\ \text{cm}$. A typical point in a weight-bearing region of the condyle would be expected to experience, at most, a sliding length approximately equal to the diameter of the contact area, or $\sim 1\ \text{cm}$. This indicates that defect presence might conservatively be expected to increase sliding distances for contacting points by 1-10%, depending on the region, perhaps contributing to accelerated tissue wear.

The work included in this dissertation also provides information on the extent to which biomechanical properties are restored following *in vivo* repair using current cell-based therapies. Testing of the retrieved *in vivo* samples (Chapter 5) revealed that cell-based therapies can result in substantial integration strengths *in vivo*, significantly greater than those observed in *in vitro* systems [44, 47, 50], but still lower than 50% of native tissue strengths. The bulk mechanical properties of repair tissue at that time-point were still significantly inferior to those of native cartilage; it's currently unclear what level of mechanical properties are necessary for a graft to survive and prevent further damage to the native tissue. In this study, growth factor treatments appeared to

enhance the quality of repair tissue but did not significantly improve its integration with the surrounding host tissue.

Several experimental and analytical methods were developed in order to carry out the experiments described above. An experimental model system was developed to study the behavior of contacting osteochondral surfaces loaded in uniaxial compression. Using this test setup, it was possible to investigate both normal and defect conditions under static and dynamic loading. Test methods were also developed for the characterization of adhesive strength and tensile properties of tissue retrieved following *in vivo* repair. This included preparation of tensile samples containing both repair and native tissue regions, application of surface staining to allow deformation to be optically tracked, and mechanical testing and image acquisition protocols.

Image analysis methods were developed to quantify sample displacements and deformations using the movement of tracked tissue markers in sequential digital images. Surface markers were tracked using image correlation techniques, and their relative displacements were used to describe tissue deformations. Analogous techniques were used to measure both macroscopic (Chapter 5: 1-D strain measurements in adjoining tissues) and microscopic deformations (Chapter 2-4: 2-D strain fields in opposing cartilage surfaces), using either static image pairs or dynamic image sequences. In addition to the current studies, these image analysis methods have also been adapted for studies of dynamic cartilage strain between opposing cartilage surfaces with applied lateral loading [58] and cartilage samples subject to mechanical bending [56].

A mathematical framework was developed to describe the dynamic contact between surfaces undergoing large deformations and slips using discretely-sampled experimental data. These methods were implemented to describe the dynamic contact between experimentally-tracked cartilage surfaces (Chapter 3 and 4). The developed approach was used for the analysis of 2-D data in the current studies, but it is also compatible with 3-D datasets.

6.2 Discussion and Future Directions

Physiological Implications of Mechanical Changes at a Defect

The results of the current studies demonstrate that the presence of a focal defect leads to increased axial compression, tissue volume loss, and shear at the defect rim and that these deformations develop more rapidly than in intact surfaces, suggesting less fluid support in this region. On the opposing, intact cartilage surface, shear strains in the regions directly opposite the defect rim are increased throughout the tissue depth. These changes may bring about significant physiological responses. It has been shown that excessive mechanical loading can result in macroscopic [32, 48] and microscopic [49, 52, 57] matrix damage and cell death [14, 16, 17, 32, 35, 39, 45, 48, 52], with increases in both magnitudes and rates of strain being implicated with greater damage. Although the exact relationship between intra-tissue strains and tissue damage has not been elucidated, it does not appear to be solely a function of the maximum compressive strain [12].

Changes in the mechanical environment could also significantly affect the cellular response of the tissue. Not only may a reduction in the cell population, due to mechanical damage, compromise the overall biosynthetic response of the tissue [31], but the remaining viable cells may have reduced metabolic function [35, 48]. Furthermore, changes in the static and dynamic strain state of the tissue may regulate the processes of tissue repair and remodeling [25, 27].

In addition to changes in the internal strain states of the cartilage surfaces, increased sliding over the surfaces adjacent to some defects was observed. Increased sliding could contribute to tissue wear over long-term loading. While the magnitudes of sliding distances measured here are an order of magnitude lower than the total sliding path during articulation, the contribution of this sliding could be significant. Much of this sliding is taking place at regions of high compression where normal forces, and hence friction, are at their highest. As discussed previously in this thesis, these effects may be even more pronounced *in vivo*, where the loss of contact area at a defect will result in higher contact stresses and total cartilage strains (which were shown here to be proportional to sliding distances). It is also possible that the presence of a defect accelerates the loss of fluid support, also adding to the friction between the contacting surfaces. Over time, even moderate increases in the contact stresses and sliding distances may be expected to accelerate tissue wear [6, 38].

Theoretical Models of Cartilage Contact

Numerous studies have attempted to mathematically model the mechanics of contacting cartilage surfaces. However, these approaches face several challenges due to the complex material properties of articular cartilage, a biphasic, anisotropic, inhomogeneous tissue that exhibits tension-compression nonlinearity, strain dependent changes in permeability, and multiple modes of surface lubrication [42]. To further complicate matters, cartilage surfaces undergo large deformations and sliding distances during joint articulation. Theoretical models of cartilage contact incorporate assumptions about the material properties, surface geometries, and boundary conditions to allow solutions to be calculated, but the validity and limitations of these assumptions are not always known.

Many early studies modeled cartilage as an elastic solid. This assumption may provide a reasonable estimate of the immediate response (loading rate \gg gel diffusion rate [4]) by assuming the material is incompressible [2-4, 9], or the equilibrium response, assuming that it is compressible [3]. However, these models cannot capture the dynamic tissue response to loading, which displays a time-dependent viscoelastic response related to fluid exudation from the tissue.

Other studies have incorporated the biphasic model [43] into solutions of cartilage contact. Hou et al developed boundary conditions relevant for the interface of a viscous fluid and a biphasic medium [29] and implemented them [30] in a numerical solution of dynamic contact between a rigid indenter and a cartilage surface separated by a thin fluid film. Those boundary conditions have been adapted to determine an asymptotic solution of the frictionless contact between two linearly

elastic, biphasic cartilage layers [7], and have been widely implemented in finite element models of contacting biphasic cartilage surfaces.

Finite element formulations have been developed that not only model the biphasic properties of cartilage, but also capture several of the other complexities of cartilage material properties. Solutions have been developed that incorporate tissue inhomogeneity [20, 55], anisotropy (modeled as transverse isotropy [18, 20]), tension-compression nonlinearities [4], or nonlinearities due to large deformations [13, 21, 53, 54] and sliding distances [13]. However, no one model has yet incorporated all of these properties and implemented them in a model of contact; each approach includes assumptions and simplifications that limit their applicability to certain conditions.

While, the general increase in model sophistication has contributed to greater confidence in tissue stress and strain predictions under simplified loading conditions, the treatment of sliding between surfaces has not received as much attention. Currently, no study has reported the local sliding between cartilage surfaces during loading, and the formulations of many of the models prohibit these calculations from being performed. Models assuming contact between symmetric surfaces will result in zero sliding due to equal expansion of the contacting sides [5, 7], while models based on penetration analysis ignore lateral deformation of the surfaces entirely [19, 53, 54]. Other modeling approaches may be capable of calculating sliding distances, but include assumptions (i.e. small sliding distances [21]) that may limit their applicability. Also, contact between cartilage surfaces is commonly assumed to be frictionless, which may lead to over-estimation of sliding distances. The assumption of frictionless contact may be especially problematic in situations where surface

lubrication may be compromised. Cartilage lubrication is likely to result from multiple modes of lubrication, with the dominant mode changing depending on the situation. Near sites of cartilage damage, compromised surface integrity or accelerated fluid depressurization may alter the form of lubrication and, in turn, the contributions of friction. Without experimental verification, it would be difficult to model these surface conditions accurately.

Many of the models also employ assumptions that are incompatible with evaluation of surface incongruities that would be present at sites of damage, such as focal defects or intra-articular step-offs. Solutions that require symmetry between the contacting surfaces, symmetry about the axis of loading, or have restrictions on the relative curvatures of the contacting surfaces, would not be appropriate for these situations [5, 7, 28, 30].

To date, little experimental validation of theoretical contact solutions has been performed, although indirect evidence of model reliability is available. Theoretical predictions of high shear stress in the deep regions of cartilage under impact loading [3, 5], correspond well to experimental observations of damage near the cartilage-bone interface following impact. Also, predictions of contact stresses in joint-scale models, and the changes in these stresses occurring near a focal defect, have shown good agreement with *ex vivo* contact pressure measurements [46]. These results are encouraging, but direct verification of intra-tissue stress and strain predictions are still desirable. Current theoretical models have provided insights into biomechanics of cartilage contact, but still contain simplifications to sample geometries, material properties, and boundary conditions, which may affect their accuracy under certain

circumstances. Experimental quantification of cartilage contact parameters could help to validate and refine the assumptions used in current theoretical models.

Choices of Experimental Parameters

The experimental model of cartilage contact was designed to isolate the effects of a defect under controlled conditions. To accomplish this, several simplifications were made compared to the *in vivo* environment. Here, contacting surfaces were loaded in uniaxial compression. *In vivo*, cartilage is subject to dynamic loading that is a mixture of compression and a complex rolling and sliding motion. Sliding between intact surfaces results in depth-varying shear strains in both surfaces [58]. In the defect case, the macroscopic protrusion of the intact surface into the empty area is likely to provide considerable resistance to any lateral motion. The effects of a defect in this case will likely be even more pronounced than in our model of compression alone. As the protruding surface pushes against the defect edge and slides over the rim, a moment will be applied at the defect base and may produce markedly elevated shear strains where the tissue is anchored to the subchondral bone. Furthermore, sliding will occur between the surface and the radial defect edge, a region of tissue that doesn't normally experience sliding and may be less resistant to wear than the articular surface.

A conservative loading protocol was chosen to establish a baseline of the effects that would be expected to result due to defect creation. Samples were tested in displacement control, with the same total strain applied to both intact and defect-containing samples. Under these conditions, strain distributions are likely to underestimate the effects of a defect. Alternative loading protocols could also be used,

but none are clearly closer to physiological conditions. Samples could be loaded to the same total stress, but since significant increases in contact stress have been shown in the regions surrounding a defect [11, 26], application of a constant stress would also tend to underestimate the effects of a defect. Conversely, equal loads could be applied to both intact and defect groups; however this choice is likely to overestimate the effects of defects because the flat, finite-sized samples used in the model are incapable of distributing load to the surrounding tissue, in the manner that occurs *in vivo*. Other loading protocols, of intermediate levels of conservativeness, could be arrived at by adjusting the applied displacement or load based on contact stress measurements or from finite element predictions.

In the future, studies should investigate the effects and interactions of joint, tissue, and defect parameters to determine their significance in focal defect contact. These include more physiological loading protocols, the curvatures of the contacting surfaces, thicknesses and material properties of the cartilage layers, and the size and edge characteristics of the defect. Some of these studies could be accomplished using the current experimental setup, by varying the locations from which samples are harvested to isolate samples with the desired characteristics. However, it would also be possible to study these factors using larger samples including a significant portion of the joint curvature and loading them against their physiologically mating surfaces. In this case, samples could be loaded to a common force and allowed to distribute the load as would occur *in vivo*. This system might provide information into physiological function, as well as higher order interactions of the various parameters.

Further, this setup may simplify investigation of effects that are not readily studied in the current configuration, such as the effects of defect size.

Mechanical Thresholds of Defect Size

One topic that is of considerable interest is the investigation of defect size thresholds that may impact clinical outcomes. Studies of cartilage defect repair often make reference to a “critical size” for defects, where those below the threshold exhibit good repair and those above it continue to progress in size and severity. Clinical algorithms use size thresholds, along with the containment and shouldering state of the defect, to determine appropriate treatments [40]. However, an objective and quantitative definition of the critical defect size and the underlying mechanisms which lead to divergent clinical outcomes have not been elucidated.

Although a single critical size for defects is typically referred to, it is more likely that several distinct threshold sizes exist, where significant changes in the defect environment occur. Large defects may be troublesome for various reasons, not the least of which is a greater volume that needs to be filled with repair tissue. Physiologically relevant critical sizes may exist that determine when **1) Continued Degeneration** is expected at an untreated defect or **2) Spontaneous Repair** will be successful and are likely to be functions of geometry, loading, and material properties. Careful design of *in vivo* studies may eventually help to elucidate these relationships. On the other hand, thresholds of mechanical behaviors may be more readily defined from geometric and experimental data and may relate to physiological outcomes.

The region of the opposing cartilage surface near the defect rim transitions from axial compression similar to that experienced by intact surfaces, to an

uncompressed state over the empty defect. The distance from the defect rim to the uncompressed region can be measured and used to define the defect size allowing a **3) Complete Transition**. The critical defect radius where this occurs, R_{trans} , was experimentally estimated to be $R_{trans}=2h\epsilon_c$, using data from Chapter 2 (Figure 6.1A), where h is cartilage thickness (same on both sides), and ϵ_c is the total (bone-to-bone) compressive strain. This results in $R_{trans}=0.8$ mm for physiologic values of thickness and compression ($h=2$ mm, and $\epsilon_c=20\%$ compression) in human femoral condyle, a very small defect size when compared to defects typically found in symptomatic patients or those normally considered physiologically critical.

The point at which the opposing surface may begin to contact the exposed bone at the defect base may be particularly important to physiological results. This is already considered in clinical algorithms in its relation to “shouldering” of the defect. More generally, **4) Bone Contact** can be predicted from the size and relative curvatures of the two contacting surfaces. This has implications for friction and wear of the opposing cartilage surface contacting the rough bony base, and also for an implant that will be forced to support excessive loads. For surfaces where both principal radii of curvature are equal, the radius at which this will occur, R_{bone} , can be estimated from the joint geometry and predicted tissue deformation using (Figure 6.1C):

$$R_{bone} = \frac{h_{eff}}{\tan\left(0.5 \cos^{-1}\left(\frac{\rho_{eff} - h_{eff}}{\rho_{eff}}\right)\right)}, \text{ where } \rho_{eff} = \frac{\rho_1 \rho_2}{\rho_1 + \rho_2} \text{ and } h_{eff} = (1 - 2\epsilon_c)h$$

where ρ_1 and ρ_2 are the curvatures of the two opposing surfaces, ρ_{eff} is the effective curvature [6] (Figure 6.1B), and h_{eff} is the effective thickness after compression of the contacting sides.

With typical values for the human knee ($h = 2$ mm, $\rho_{\text{eff}} = 20$ mm [6], and $\varepsilon_c = 20\%$ compression) the critical radius is estimated to be 7.8 mm (area of 1.9 cm²), which is close to the 2 cm² threshold used in many clinical algorithms [40]. In cases where the principal radii of curvature differ significantly, one can estimate the 2 critical defect radii: the lower value determines the point at which the shouldering is lost in that direction, the higher radius predicts the onset of bone contact. Since loss of support in one direction would increase the burden on the edges remaining in contact, it is probable that compression on these surfaces would be significantly increased, meaning h_{eff} should be lowered accordingly; calibration of this parameter could be gathered from experimental data. It is possible that other significant mechanical criteria also exist, such as the percent loss of original contact area; however, their significance would have to be determined experimentally.

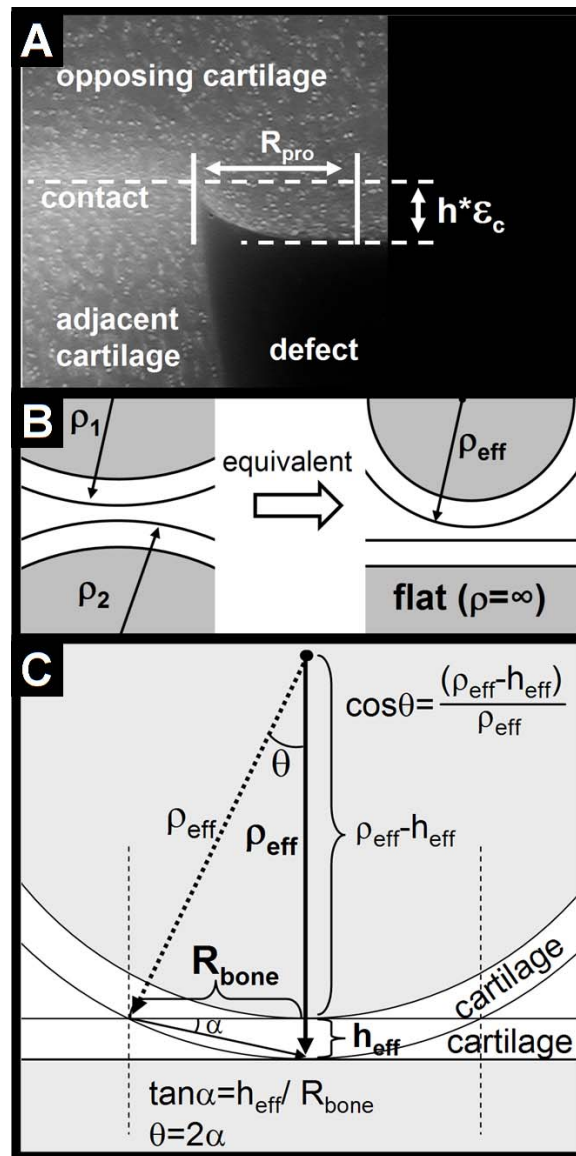


Figure 6.1: Potential size thresholds of defect mechanical behavior. A) Diameter required for full protrusion of the opposing surface into the defect C) Diameter at which the opposing surface will be able to contact the boney defect base, based on B) an estimate of effective radius of two contacting curved surfaces.

Identification of Mechanisms of Integrative Cartilage Repair

As discussed in Chapter 5, treatments for focal cartilage defects result in interfaces with the native articular cartilage that exhibit poor integration. The inability to restore sufficient strength at an interface may prevent restoration of normal tissue mechanical function and possibly lead to graft failure and continued degeneration of the surrounding tissue.

Currently, the molecular mechanisms responsible for normal integrative repair, and the changes resulting from treatments that enhance repair, remain unclear. Previous experiments have identified factors that influence the development of adhesive strength at an interface [1, 10, 15, 50], but do not provide the details of how that strength develops. The mechanisms of action for treatments that enhance adhesive strength development are also unknown.

Part of the uncertainty surrounding the process by which integration occurs, comes from a fundamental lack of knowledge of the behavior of collagen type II, the state of the collagen network in mature cartilage, and the ability for existing fibrils to interact with each other or with newly synthesized collagen. It is also unclear whether the collagen network at a defect edge comprises interior cross-sections of broken or lacerated fibrils, or intact fibril ends that have been pulled-out of the opposing side [37, 51]. Understanding the ways in which collagen normally acts at an interface may provide insights into how the process may be improved.

There are three potential mechanisms by which the collagen network may act to repair itself during integration: 1) fusion of existing fibrils, 2) extension of existing fibrils by deposition of new collagen, and 3) formation of new fibrils. Exposed fibril

ends could fuse with neighboring fibril ends on the opposite side of the interface. If widespread (and of sufficient strength) this process could quickly result in a structure approaching that of uninjured cartilage. Since the process involves interactions between existing fibrils, many of the characteristics of normal cartilage would already be present. The fibril diameters, spacing, orientation, density, and interfibrillar interactions would be preserved. Fusion of type II collagen fibrils has not been demonstrated directly, but it is likely to occur, given the paucity of fibril tips in mature articular cartilage. Studies on collagen I fibril fusion have suggested that fusion will occur only at the tapered fibril tips [24], with fusion along remainder of the fibril inhibited by the presence of small proteoglycans, such as decorin, at the fibril surface [8, 24]; this potentially suggests that any broken fibrils at an edge may be incapable of fusing. It is also possible that the fusion process requires a specific fibril terminal (in collagen I, the C- terminal) [24], further reducing potential fusion sites and representing a possible fusion limit that may be reached during maturation [24]. Given these restrictions, it seems unlikely that the few sites capable of fusion would be positioned in close enough proximity to contribute significantly to integration. The extent to which these observations can be translated to predict the behavior of type II collagen fibrils is unclear. The collagen I and II molecules are highly homologous but differ in several respects, including their *in vitro* and *in vivo* [22, 23] self-assembly processes. It is also unclear how the strength of sites of fusion compares to the normal fibril tensile strength.

2) **Fibril Extension:** Potentially, newly synthesized collagen could be deposited on, and crosslinked to, the existing collagen network. In this case, existing

fibrils might be lengthened by the addition of collagen to the exposed end. These lengthening fibrils would be anchored to the existing collagen network on one side, but would need to extend significantly into the opposing surface in order to restore normal collagen organization. It is unclear whether this can occur in normal mature articular cartilage. It is known that collagen fibrils grow in both diameter and length during growth and maturation and that these changes occur by a combination of collagen deposition and fusion of existing fibrils. There is evidence that small proteoglycans or minor collagens located on the surface of fibrils may limit fibril diameter; these same molecules may inhibit interactions between the collagen fibrils and newly synthesized collagen. As is the case with fusion behaviors, it is possible that the fibril polarity or the state of the fibril end could affect this process.

3) Fibril Formation: Newly synthesized collagen can diffuse to the interface and self-assemble into new collagen fibrils. Among the mechanisms discussed here, this would probably result in the slowest restoration of normal network structure and lowest levels of strength. New fibrils tend to be thinner and shorter than those of the existing network; development of the fibrils into a mature state (with normal diameter and length) would require time. Also, direction of the growth in the preferred orientation, penetration of the fibrils into the existing matrix on both sides of the interface, and formation of typical interactions with other fibrils would be necessary.

Integrative repair may result from some combination of these mechanisms working interactively or in parallel. Previous results suggest that the primary mechanism of integration may be the formation of new fibrils at the interface [41], while the interactions of newly synthesized collagen with the pre-existing network are

still unclear. The relatively poor intrinsic repair at an interface may result from the inability to better utilize the existing collagen fibrils. The ability of enzymatic treatments to improve adhesive strength development at an interface may be explained by more than one of the proposed mechanisms. Treatments could function by removing molecules blocking access to the surface of collagen fibrils (i.e. decorin), thereby allowing interactions with newly synthesized collagen [24]. On the other hand, enzymatic treatments could affect integration by just creating space for increased transport of collagen [36] and assembly of new fibrils [33, 34]. Elucidating the mechanisms by which integration normally occurs and the effects on these mechanisms of treatments shown to increase adhesive strength may provide insight into methods of enhancing integrative repair.

Link between Mechanics and Physiological Response and Assessment of Repair

The current studies provided evidence for a possible mechanical contribution to progressive cartilage degeneration (Figure 6.2). Strain elevations have been shown previously to cause cell death [17, 35, 39, 45, 48] and solid matrix damage [48, 52] under certain conditions. Cartilage, like traditional materials, can reasonably be expected to show accelerated fatigue and wear when subjected to greater amounts of loading and contact [6]. It remains to be seen whether the effects of defects are physiologically significant. *In vitro* investigation of viable cartilage blocks under physiological loading may be able to determine whether the presence of a defect will induce acute or chronic tissue damage.

Similar methods could also be used to assess the efficacy of repair strategies. The effects of graft properties or integration at the interface may be studied and used

to gauge the effectiveness of treatments. Using experimental protocols analogous to those used in this dissertation, it would be possible to measure the changes in defect mechanics due to different grafts. Then, as has been suggested for the empty defect studies, the ability for different graft types to prevent adverse physiological consequences under physiological loading could also be assessed. Establishment of this link may make it possible to identify methods of repair that, at the very least, are capable of arresting the degenerative process at the defect site.

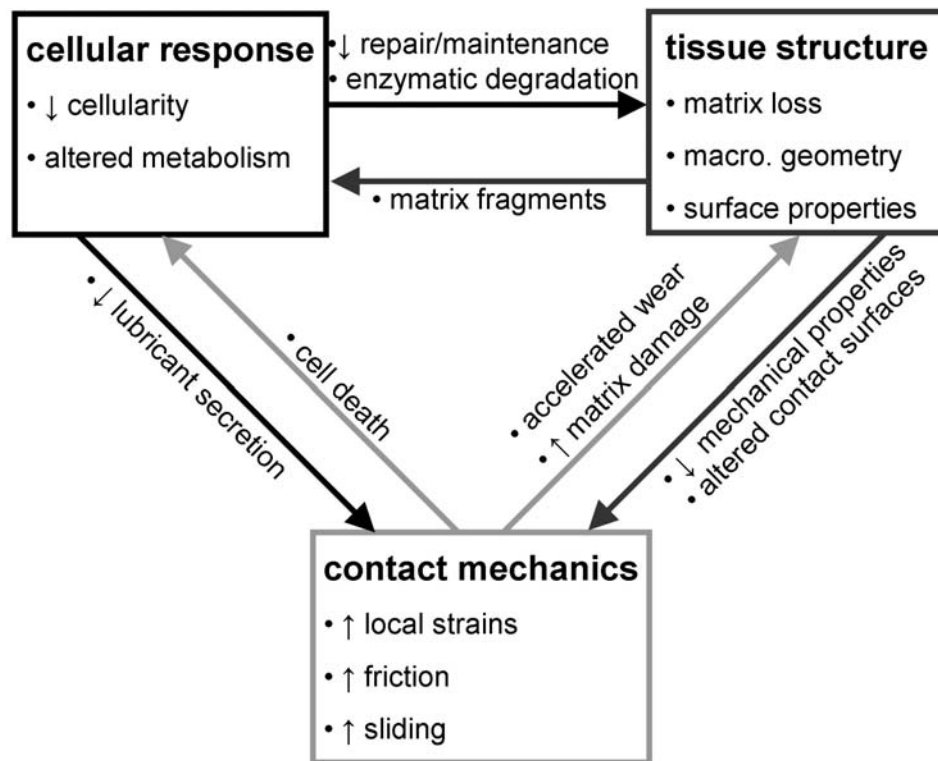


Figure 6.2: Hypothesized mechanisms of defect progression.

6.4 References

1. Ahsan T, Lottman LM, Harwood FL, Amiel D, Sah RL: Integrative cartilage repair: inhibition by beta-aminopropionitrile. *J Orthop Res* 17:850-7, 1999.
2. Anderson DD, Brown TD, Radin EL: Stress wave effects in a finite element analysis of an impulsively loaded articular joint. *Proc Inst Mech Eng [H]* 205:27-34, 1991.
3. Armstrong CG: An analysis of the stresses in a thin layer of articular cartilage in a synovial joint. *Eng Med* 15:55-61, 1986.
4. Ateshian GA, Ellis BJ, Weiss JA: Equivalence between short-time biphasic and incompressible elastic material responses. *J Biomech Eng* 129:405-12, 2007.
5. Ateshian GA, Lai WM, Zhu WB, Mow VC: An asymptotic solution for the contact of two biphasic cartilage layers. *J Biomech* 27:1347-60, 1994.
6. Ateshian GA, Mow VC: Friction, lubrication, and wear of articular cartilage and diarthrodial joints. In: *Basic Orthopaedic Biomechanics and Mechano-Biology*, ed. by VC Mow, Huiskes R, Lippincott Williams & Wilkins, Philadelphia, 2005, 447-94.
7. Ateshian GA, Wang H: A theoretical solution for the frictionless rolling contact of cylindrical biphasic articular cartilage layers. *J Biomech* 28:1341-55, 1995.
8. Birk DE, Nurminskaya MV, Zycband EI: Collagen fibrillogenesis in situ: fibril segments undergo post-depositional modifications resulting in linear and lateral growth during matrix development. *Dev Dynamics* 202:229-43, 1995.
9. Blankevoort L, Kuiper JH, Huiskes R, Grootenboer HJ: Articular contact in a three-dimensional model of the knee. *J Biomech* 24:1019-31, 1991.
10. Bos PK, DeGroot J, Budde M, Verhaar JA, van Osch GJ: Specific enzymatic treatment of bovine and human articular cartilage: implications for integrative cartilage repair. *Arthritis Rheum* 46:976-85, 2002.
11. Brown TD, Pope DF, Hale JE, Buckwalter JA, Brand RA: Effects of osteochondral defect size on cartilage contact stress. *J Orthop Res* 9:559-67, 1991.
12. Chahine NO, Ateshian GA, Hung CT: The effect of finite compressive strain on chondrocyte viability in statically loaded bovine articular cartilage. *Biomech Model Mechanobiol* 6:103-11, 2007.
13. Chen X, Chen Y, Hisada T: Development of a finite element procedure of contact analysis for articular cartilage with large deformation based on the biphasic theory. *Jsme International Journal Series C-Mechanical Systems Machine Elements and Manufacturing* 48:537-46, 2005.

14. Clements KM, Bee ZC, Crossingham GV, Adams MA, Sharif M: How severe must repetitive loading be to kill chondrocytes in articular cartilage? *Osteoarthritis Cartilage* 9:499-507, 2001.
15. DiMicco MA, Sah RL: Integrative cartilage repair: adhesive strength correlates with collagen deposition. *J Orthop Res* 19:1105-12, 2001.
16. D'Lima DD, Hashimoto S, Chen PC, Colwell CW, Jr., Lotz MK: Human chondrocyte apoptosis in response to mechanical injury. *Osteoarthritis Cartilage* 9:712-9, 2001.
17. D'Lima DD, Hashimoto S, Chen PC, Lotz MK, Colwell CW, Jr.: Cartilage injury induces chondrocyte apoptosis. *J Bone Joint Surg Am* 83-A Suppl 2:19-21, 2001.
18. Donzelli PS, Spilker RL, Ateshian GA, Mow VC: Contact analysis of biphasic transversely isotropic cartilage layers and correlations with tissue failure. *J Biomech* 32:1037-47, 1999.
19. Dunbar WL, Jr., Un K, Donzelli PS, Spilker RL: An evaluation of three-dimensional diarthrodial joint contact using penetration data and the finite element method. *J Biomech Eng* 123:333-40, 2001.
20. Federico S, Grillo A, La Rosa G, Giaquinta G, Herzog W: A transversely isotropic, transversely homogeneous microstructural-statistical model of articular cartilage. *J Biomech* 38:2008-18, 2005.
21. Federico S, La Rosa G, Herzog W, Wu JZ: Effect of fluid boundary conditions on joint contact mechanics and applications to the modeling of osteoarthritic joints. *J Biomech Eng* 126:220-5, 2004.
22. Fertala A, Holmes DF, Kadler KE, Sieron AL, Prockop DJ: Assembly in vitro of thin and thick fibrils of collagen II from recombinant procollagen II. The monomers in the tips of thick fibrils have the opposite orientation from monomers in the growin tips of collagen I fibrils. *J Biol Chem* 271:14864-9, 1996.
23. Fertala A, Sieron AL, Ganguly A, Li SW, Ala-Kokko L, Anumula kR, Prockop DJ: Synthesis of recombinant human procollagen II in a stably transfected tumour cell line (HT1080). *Biochem J* 298:31-7, 1994.
24. Graham HK, Holmes DF, Watson RB, Kadler KE: Identification of collagen fibril fusion during vertebrate tendon morphogenesis. The process relies on unipolar fibrils and is regulated by collagen-proteoglycan interaction. *J Mol Biol* 295:891-902, 2000.
25. Grodzinsky AJ, Levenston ME, Jin M, Frank EH: Cartilage tissue remodeling in response to mechanical forces. *Annu Rev Biomed Eng* 2:691-713, 2000.
26. Guettler JH, Demetropoulos CK, Yang KH, Jurist KA: Osteochondral defects in the human knee: influence of defect size on cartilage rim stress and load redistribution to surrounding cartilage. *Am J Sports Med* 32:1451-8, 2004.

27. Guilak F, Sah RL, Setton LA: Physical regulation of cartilage metabolism. In: *Basic Orthopaedic Biomechanics*, ed. by VC Mow, Hayes WC, Raven Press, New York, 1997, 179-207.
28. Hayes WC, Keer LM, Herrmann KG, Mockros LF: A mathematical analysis for indentation tests of articular cartilage. *J Biomech* 5:541-51, 1972.
29. Hou JS, Holmes MH, Lai WM, Mow VC: Boundary conditions at the cartilage-synovial fluid interface for joint lubrication and theoretical variations. *J Biomech Eng* 111:78-87, 1989.
30. Hou JS, Mow VC, Lai WM, Holmes MH: An analysis of the squeeze-film lubrication mechanism for articular cartilage. *J Biomech* 25:247-59, 1992.
31. Hunziker EB, Quinn TM: Surgical removal of articular cartilage leads to loss of chondrocytes from cartilage bordering the wound edge. *J Bone Joint Surg Am* 85-A Suppl 2:85-92, 2003.
32. Jeffrey JE, Gregory DW, Aspden RM: Matrix damage and chondrocyte viability following a single impact load on articular cartilage. *Arch Biochem Biophys* 322:87-96, 1995.
33. Kuijer R, van de Stadt RJ, de Koning MH, van der Korst JK: Influence of constituents of proteoglycans on type II collagen fibrillogenesis. *Coll Relat Res* 5:379-91, 1985.
34. Kuijer R, van de Stadt RJ, de Koning MHMT, van Kampen GPJ, van der Korst JK: Influence of cartilage proteoglycans on type II collagen fibrillogenesis. *Connect Tissue Res* 17:83-97, 1988.
35. Kurz B, Jin M, Patwari P, Cheng DM, Lark MW, Grodzinsky AJ: Biosynthetic response and mechanical properties of articular cartilage after injurious compression. *J Orthop Res* 19:1140-6, 2001.
36. Leddy H: Site-specific molecular diffusion in articular cartilage measured using fluorescence recovery after photobleaching. *Ann Biomed Eng* 31:753-60, 2003.
37. Lewis JL, Johnson SL: Collagen architecture and failure processes in bovine patellar cartilage. *J Anat* 199:483-92, 2001.
38. Lipshitz H, Glimcher MJ: In vitro studies of the wear of articular cartilage. II. characteristics of the wear of articular cartilage when worn against stainless steel plates having characterized surfaces. *Wear* 52:297-339, 1979.
39. Loening A, Levenston M, James I, Nuttal M, Hung H, Gowen M, Grodzinsky A, Lark M: Injurious mechanical compression of bovine articular cartilage induces chondrocyte apoptosis. *Arch Biochem Biophys* 381:205-12, 2000.

40. Mandelbaum BR, Browne JE, Fu F, Micheli L, Mosely JB, Jr., Erggelet C, Minas T, Peterson L: Articular cartilage lesions of the knee. *Am J Sports Med* 26:853-61, 1998.
41. Moretti M, Wendt D, Dickinson SC, Sims TJ, Hollander AP, Kelly DJ, Prendergast PJ, Heberer M, Martin I: Effects of in vitro preculture on in vivo development of human engineered cartilage in an ectopic model. *Tiss Eng* 11:1421-8, 2005.
42. Mow VC, Hayes WC, eds. Basic Orthopaedic Biomechanics. 2nd ed. New York: Raven Press; 1997.
43. Mow VC, Kuei SC, Lai WM, Armstrong CG: Biphasic creep and stress relaxation of articular cartilage in compression: theory and experiment. *J Biomech Eng* 102:73-84, 1980.
44. Obradovic B, Martin I, Padera RF, Treppo S, Freed LE, Vunjak-Novakovic G: Integration of engineered cartilage. *J Orthop Res* 19:1089-97, 2001.
45. Patwari P, Gaschen V, James IE, Berger E, Blake SM, Lark MW, Grodzinsky AJ, Hunziker EB: Ultrastructural quantification of cell death after injurious compression of bovine calf articular cartilage. *Osteoarthritis Cartilage* 12:245-52, 2004.
46. Pena E, Calvo B, Martinez MA, Doblare M: Effect of the size and location of osteochondral defects in degenerative arthritis. A finite element simulation. *Comput Biol Med* 37:376-87, 2007.
47. Peretti GM, Bonassar LJ, Caruso EM, Randolph MA, Trahan CA, Zaleske DJ: Biomechanical analysis of a chondrocyte-based repair model of articular cartilage. *Tissue Eng* 5:317-26, 1999.
48. Quinn TM, Allen RG, Schalet BJ, Perumbuli P, Hunziker EB: Matrix and cell injury due to sub-impact loading of adult bovine articular cartilage explants: effects of strain rate and peak stress. *J Orthop Res* 19:242-9, 2001.
49. Radin EL, Burr DB, Caterson B, Fyhrie D, Brown TD, Boyd RD: Mechanical determinants of osteoarthritis. *Sem Arthritis Rheum* 21:12-21, 1991.
50. Reindel ES, Ayroso AM, Chen AC, Chun DM, Schinagl RM, Sah RL: Integrative repair of articular cartilage *in vitro*: adhesive strength of the interface region. *J Orthop Res* 13:751-60, 1995.
51. Stok K, Oloyede A: A qualitative analysis of crack propagation in articular cartilage at varying rates of tensile loading. *Connect Tissue Res* 44:109-20, 2003.
52. Thibault M, Poole AR, Buschmann MD: Cyclic compression of cartilage/bone explants in vitro leads to physical weakening, mechanical breakdown of collagen and release of matrix fragments. *J Orthop Res* 20:1265-73, 2002.

53. Un K, Spilker RL: A penetration-based finite element method for hyperelastic 3D biphasic tissues in contact. Part II: finite element simulations. *J Biomech Eng* 128:934-42, 2006.
54. Un K, Spilker RL: A penetration-based finite element method for hyperelastic 3D biphasic tissues in contact: Part 1--Derivation of contact boundary conditions. *J Biomech Eng* 128:124-30, 2006.
55. Wang CC-B, Hung CT, Mow VC: An analysis of the effects of depth-dependent aggregate modulus on articular cartilage stress-relaxation behavior in compression. *J Biomech* 34:75-84, 2001.
56. Williams GM, Gratz KR, Sah RL: Asymmetrical strain distribution and neutral axis location in cartilage subjected to bending. *5th International Symposium on Mechanobiology of Cartilage and Chondrocyte, Athens GR*, 2007.
57. Wilson W, van Burken C, van Donkelaar C, Buma P, van Rietbergen B, Huiskes R: Causes of mechanically induced collagen damage in articular cartilage. *J Orthop Res* 24:220-8, 2006.
58. Wong BL, Bae WC, Chun J, Gratz KR, Sah RL: Micro-mechanics of cartilage articulation: effect of degeneration on shear deformation. *Trans Orthop Res Soc* 32:100, 2007.

APPENDIX A

SUPPLEMENTAL MATERIAL FOR CHAPTER 2

A.1 Introduction

Chapter 2 presents and discusses the major findings of this study. In certain cases, choices made in the data analysis may affect the interpretation of the data. This appendix provides greater detail on the reasons the choices were made and also presents results from alternative methods. Supplemental data not included in the chapter is also presented.

A.2 Materials and Methods

Bovine Data

In addition to the data presented in chapter 2, parallel tests were performed using osteochondral blocks from the femoral condyles of mature bovine knees. Sample preparation and test methods were the same, except samples were compressed to 15% (rather than 20%). Analyses were also carried out similarly, with the one difference being the depths defining the middle (M) and deep (D) zones. Since bovine cartilage is $\sim 1/2$ the thickness of human, depths were reduced to correspond to a similar percentage of the total cartilage thickness: M ($z = 300:400 \mu\text{m}$) and D ($z = 900:1000 \mu\text{m}$).

Adjustment of Relative Lateral Displacement Data with Intact Control Values

High inter-sample variability was observed in sliding calculations made on raw data. It was noted that the defect orientation may have been having a significant effect, so that factor would later be studied explicitly in chapter 4. However, it is possible that properties of individual cartilage surfaces may be contributing to the observed variability.

Non-negligible amounts of sliding were observed between opposing intact surfaces, a behavior that appeared to be mediated by differences in the properties individual blocks, including the relative surface curvatures. Sliding distances measured near defects can then be considered as a combination of two separate components of sliding: 1) the inherent sliding between a particular pair of cartilage blocks and 2) the sliding caused by a defect.

In intact cases, the direction of sliding varied depending on the characteristics of the two blocks. On the other hand, the contribution of a defect was always directed in the same direction, with the adjacent cartilage moving towards the defect with respect to the opposing surface. Thus, in cases where significant sliding occurs between the intact surfaces, sliding at a defect will be exaggerated when the two contributions are in the same direction, and sliding magnitudes will be reduced if the two contributions are in opposite directions. In order to better discern the effects of a focal defect, the average relative lateral displacement (RLD) between the surfaces in the intact configuration was subtracted from RLD measurements for the analyzed surfaces in intact and defect samples.

The RLD's over tracked portions of opposing intact surfaces were calculated from the displacements of points on each of the surfaces (described in detail in Chapter 2). For each surface, lateral (x- direction) displacement was fit to a linear function of x- position (Figure A.1). The average RLD for the intact surfaces was then determined as the difference between the lateral displacements calculated from the two equations at $x=0$ (the center of the block width). The average RLD for the intact blocks was then subtracted from the calculated RLD's in regions of interest in both the intact and defect samples. Details on the surface regions that were analyzed in each sample type are included in Chapter 2.

Data Analysis and Statistics

A full description of the statistics employed in this study is given in Chapter 2. Here, a brief explanation of key issues is presented.

Large differences between variances of samples were observed in both strain and RLD data. Generally, variances were proportional to the magnitudes of sample means. All statistics were performed on log-transformed data to minimize differences in variances. For planned comparisons, any remaining differences were accounted for by using t-tests for unequal variances.

For strain and area/volume change data, values from the both sides of each intact control were pooled to provide a single set of control values per sample pair ($n=4$ total control values). Initially, each control side had been treated as an independent sample, resulting $n = 8$ ($4 \text{ pairs} \times 2 \text{ blocks/pair}$) control measurements. However, contacting samples were found to not be independent, using a test of correlation between the two sides [1].

A.3 Results

A summary and discussion of the major results of this study are given in chapter 2. Here a summary of the results from bovine samples is included. A brief summary of how adjustment of the sliding data affected the results is given below. Additional strain and deformation data are also provided here in the form of figures.

Bovine Strain and Sliding Results

Deformation of bovine samples was qualitatively similar to that of human samples. Intact samples showed typical, depth-varying magnitudes of axial strain. Defect samples had increased axial, and shear strains in the adjacent surface and increased shear in the region opposing the defect rim. The main difference was a tendency for increases in axial strain to take place in the M region, rather than the S, as was seen in human samples.

Sliding behavior was also similar, however variability was even higher than in human samples and no statistically significant increases were measured. Greater detail on these outcomes is provided below, in the discussion of the sliding analyses.

For easier comparison, all graphs of bovine data in this appendix also repeat the corresponding results from human samples that were included in chapter 2.

Adjustment of Relative Lateral Displacement Data with Intact Control Values

The measured relative lateral displacements for both bovine and human samples in chapter 2 were adjusted using the methods described above and re-analyzed. There was little effect on the resulting trends or inter-sample variability in either bovine or human samples (Figures A.2 and A.3). As would be expected, adjustment of the intact RLD's by the average sample RLD resulted in a mean very close to zero and relatively low variances.

For human samples, the average profile of lateral displacement near a defect was similar to that of the raw data, and the magnitudes of these displacements were slightly reduced compared to the raw data at all surface points (Figure 2). The variances of displacement measures were relatively unchanged by adjustment. No surface points near defects were seen to have significantly greater sliding than the control samples with or without the adjustment of the data. However, adjustment of the sliding data did result in reduced p values at every point, with several points approaching significance. The normalized RLD (the calculation of which is described in Chapter 2) of defect samples, 0.08 ± 0.03 , was significantly higher than that of intact controls, 0.02 ± 0.01 , when calculated using adjusted data, differing from the results using the raw data (Figure A.3; raw data: $p=0.13$; adjusted data $p<0.05$).

Adjustment of sliding data from bovine samples had similar effects to those seen on bovine samples (Figures A.4 and A.5). Mean sliding distances were relatively unchanged, while sample variances actually increased slightly. No measures of sliding were significant using either the raw or adjusted data.

It is likely that significant variations in sliding result from differences in sample or defect properties that were not controlled for in the current study. Specifically, the curvatures of the two opposing surfaces and the orientation of the defect edge may both help determine the sliding behavior. In the later chapters, the effects of edge orientation are looked at in more detail. Also, the current chapter used samples taken from the femoral condyle which, while macroscopically flat, did have some amount of surface curvature. Samples in chapter 4 were taken from the patellofemoral groove in an attempt to minimize the effects of curvature.

A.4 Acknowledgments

This chapter will be submitted, in part, for publication in *Biorheology*. The dissertation author is the primary investigator and thanks co-authors Ben Wong and Drs. Won Bae and Robert Sah. This work was supported in part by the National Institutes of Health and the National Science Foundation, and by a grant to the University of California, San Diego, in support of Dr. Robert Sah, from the Howard Hughes Medical Institute through the Professors Program.

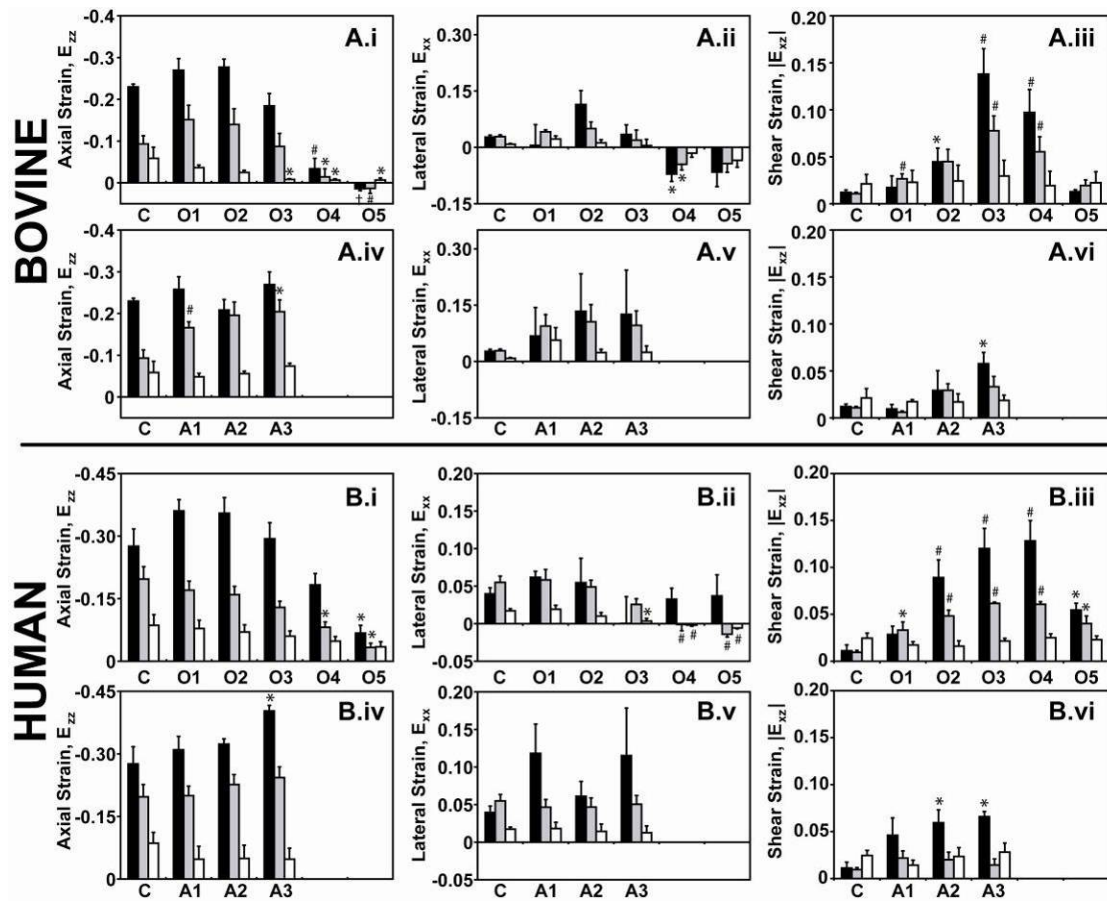


Figure A.1: Strain measurements at selected sub-regions in bovine (A.i-A.vi) and human samples (B.i-B.vi). Strains were calculated in $100 \times 100 \mu\text{m}$ sub-regions at S (■), M (■), and D (□) depths for several lateral positions along the cartilage surfaces adjacent (A1-A3) and opposing (O1-O5) a focal defect. Strain in each sub-region was compared to the value from intact control samples (C) at the corresponding depth (* $p < 0.05$; # $p < 0.01$; † $p < 0.001$). Data are expressed as mean \pm SEM. $n=4$.

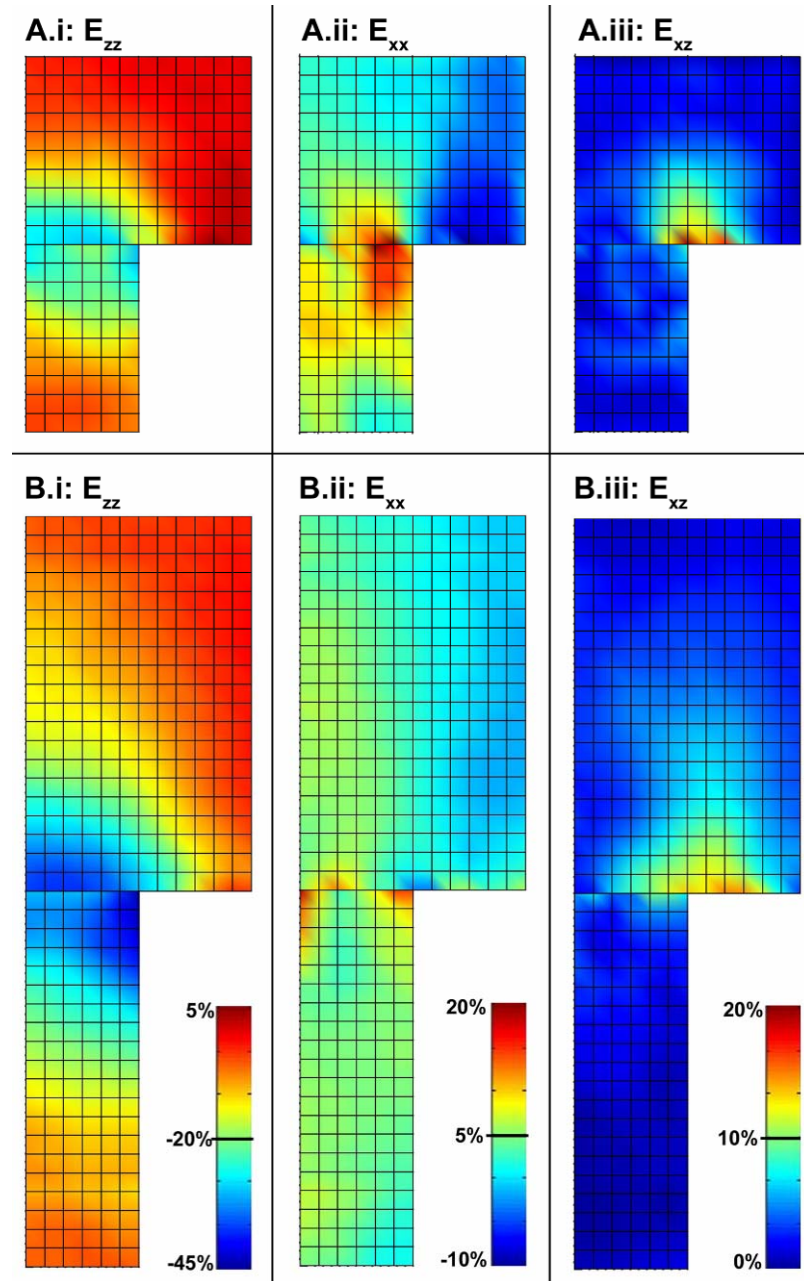


Figure A.2: Composite strain maps of (A) bovine and (B) human defect samples, for regions $\pm 600 \mu\text{m}$ laterally from the defect and 1 mm (bovine) or 2 mm (human) tissue depth.

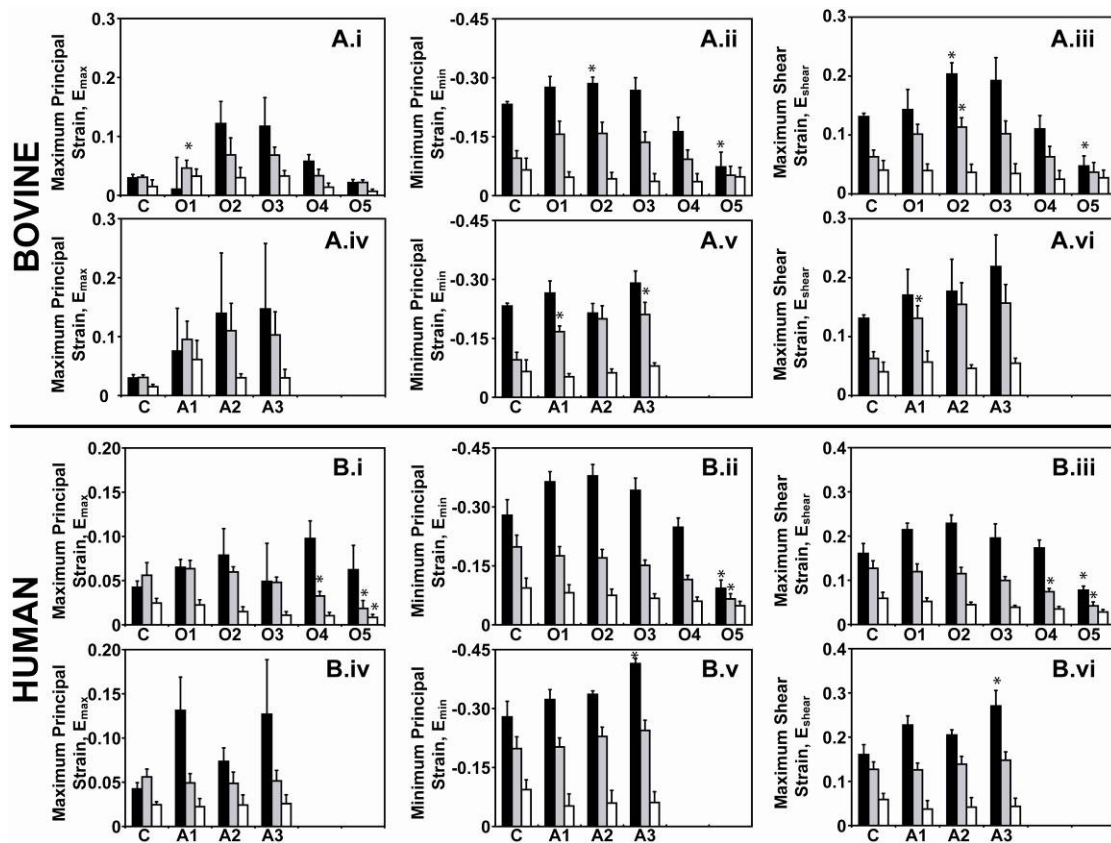


Figure A.3: Principal strain measurements at selected sub-regions in bovine (A.i-A.vi) and human samples (B.i-B.vi). Strains were calculated in $100 \times 100 \mu\text{m}$ sub-regions at S (■), M (■), and D (□) depths for several lateral positions along the cartilage surfaces adjacent (A1-A3) and opposing (O1-O5) a focal defect. Strain in each sub-region was compared to the value from intact control samples (C) at the corresponding depth (* $p < 0.05$; # $p < 0.01$; † $p < 0.001$). Data are expressed as mean \pm SEM. $n=4$.

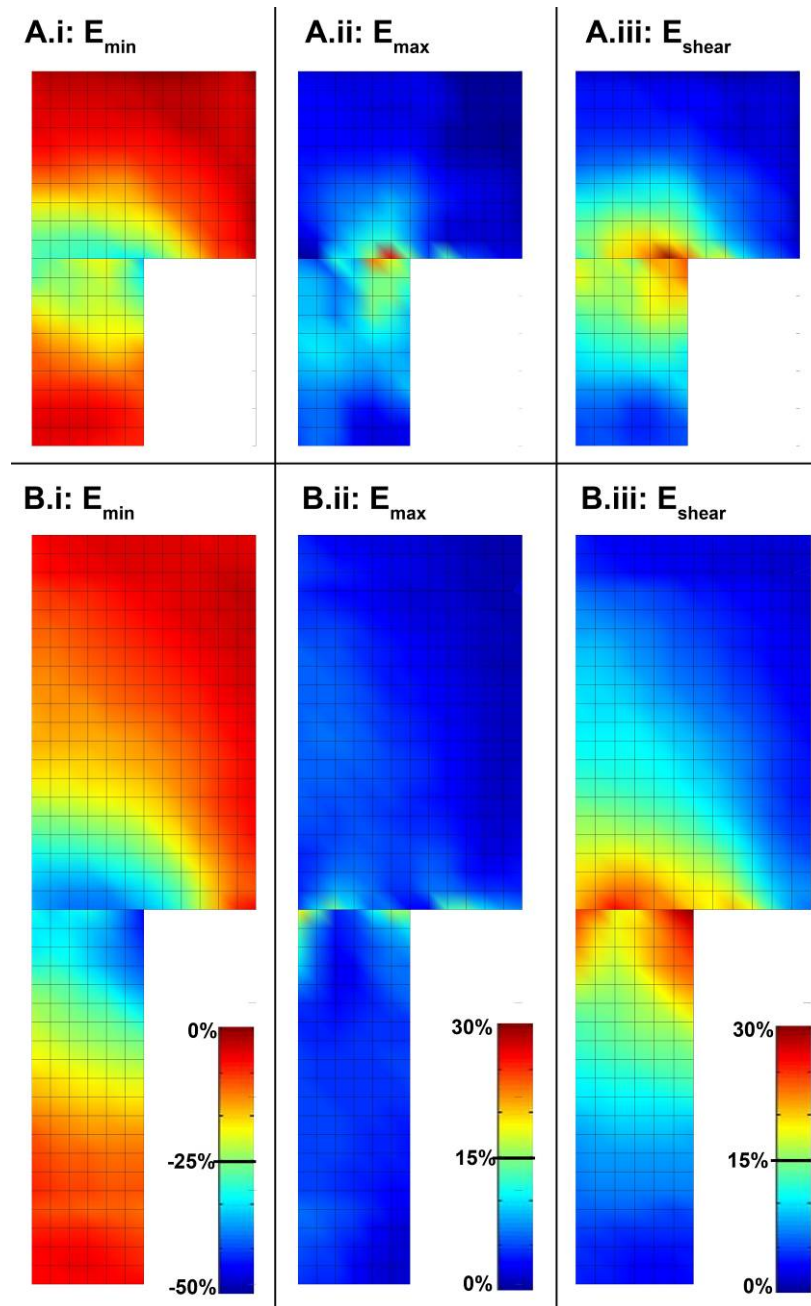


Figure A.4: Composite principal strain maps of (A) bovine and (B) human defect samples, for regions $\pm 600 \mu\text{m}$ laterally from the defect and 1 mm (bovine) or 2 mm (human) tissue depth.

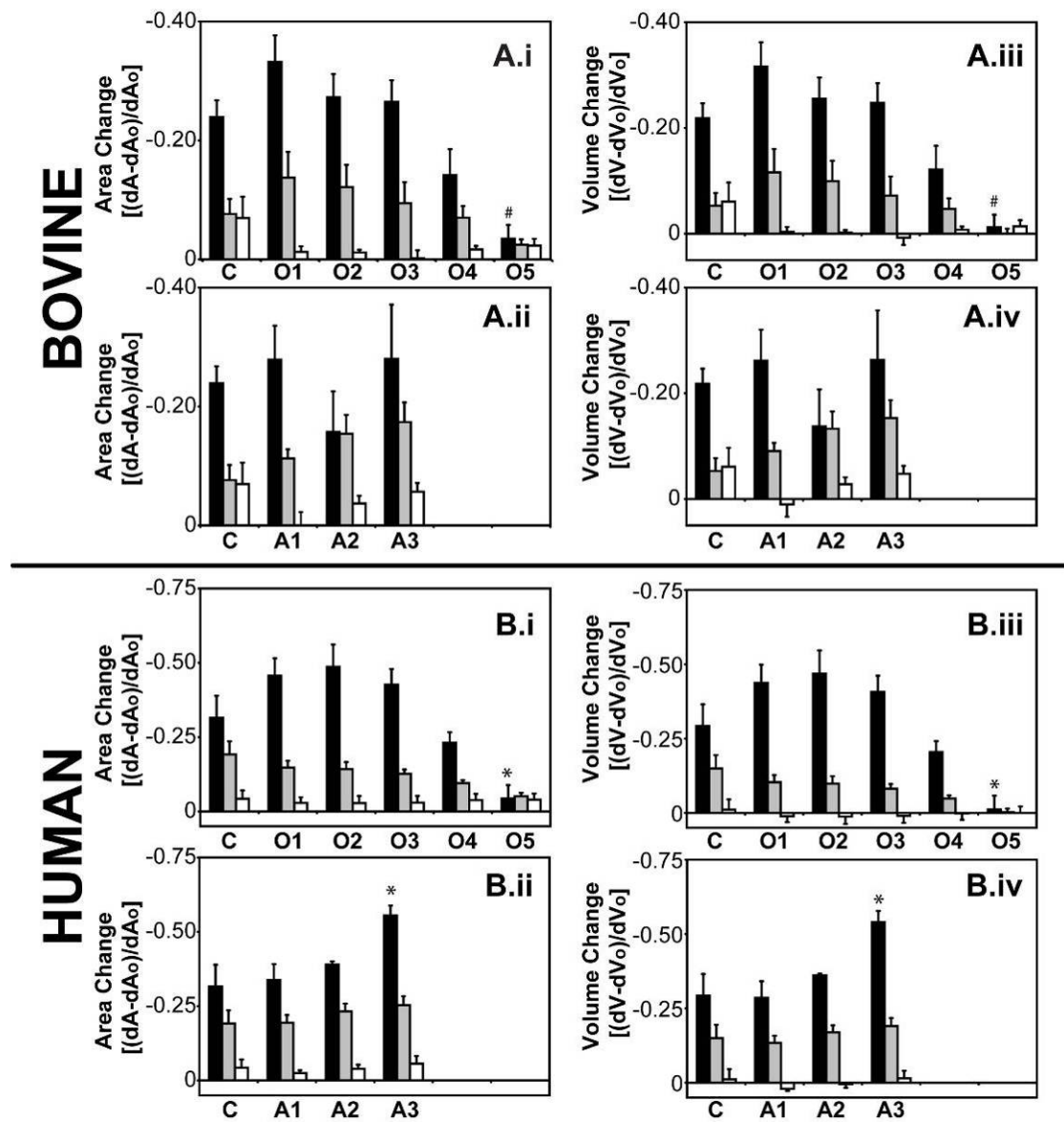


Figure A.5: Area and volume changes at selected sub-regions in bovine (A.i-A.iv) and human samples (B.i-B.iv). Strains were calculated in 100 x 100 μm sub-regions at S (■), M (▒), and D (□) depths for several lateral positions along the cartilage surfaces adjacent (A1-A3) and opposing (O1-O5) a focal defect. Strain in each sub-region was compared to the value from intact control samples (C) at the corresponding depth (*p<0.05; #p<0.01; †p<0.001). Data are expressed as mean \pm SEM. n=4

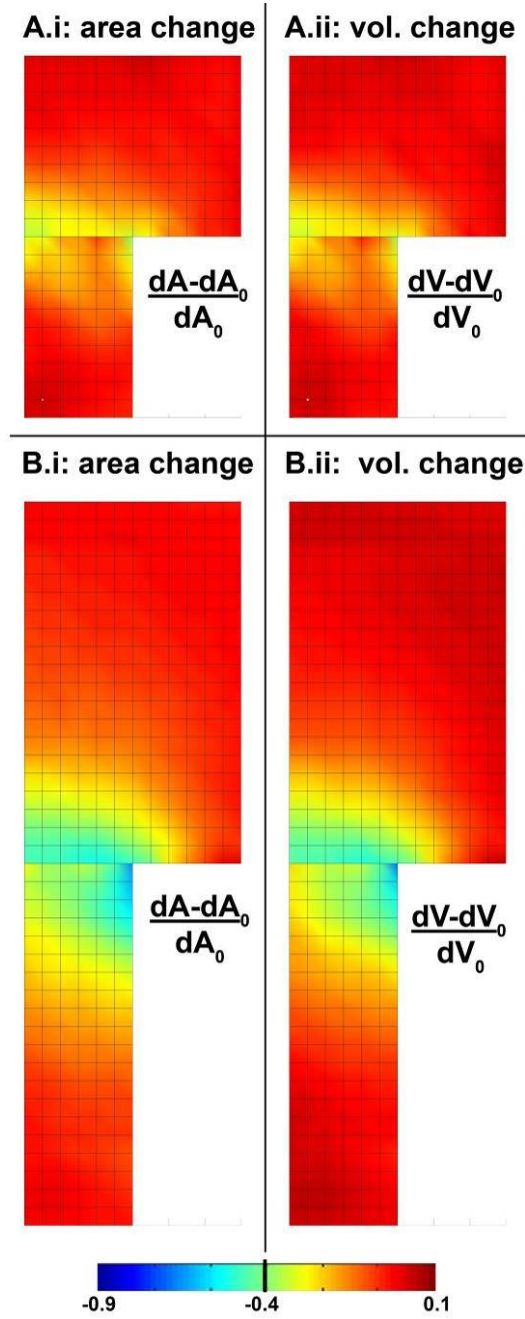
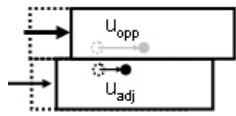


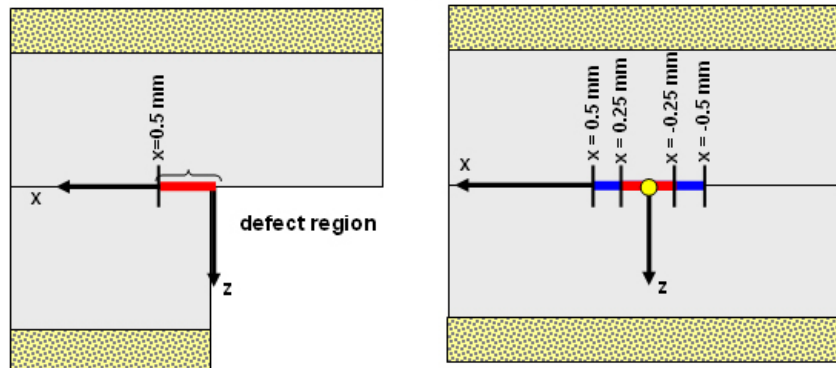
Figure A.6: Composite maps of area and volume changes in (A) bovine and (B) human defect samples, for regions $\pm 600 \mu\text{m}$ laterally from the defect and 1 mm (bovine) or 2 mm (human) tissue depth.

A) 1-D Estimate of Sliding



$$\text{relative lateral displacement (RLD)} = u_{\text{opp}} - u_{\text{adj}}$$

B) Schematic of Sliding Analysis Regions



average control RLD

$$u_{\text{opp}} - u_{\text{adj}} @ x = 0$$

$$u_{\text{opp}} = m_1 \cdot x + b_1$$

$$u_{\text{adj}} = m_2 \cdot x + b_2$$

$$\text{Adjusted RLD} = \text{RLD} - \text{average control RLD}$$

Figure A.7: Schematic of the sliding calculations. A) Since the majority of sliding in the experimental configuration takes place in the lateral (x-) direction, sliding may be estimated as the relative lateral displacement (RLD) of neighboring points on the opposing surfaces. B) Contributions of defects to sliding may be isolated by subtracting the average RLD between the intact surfaces in control samples.

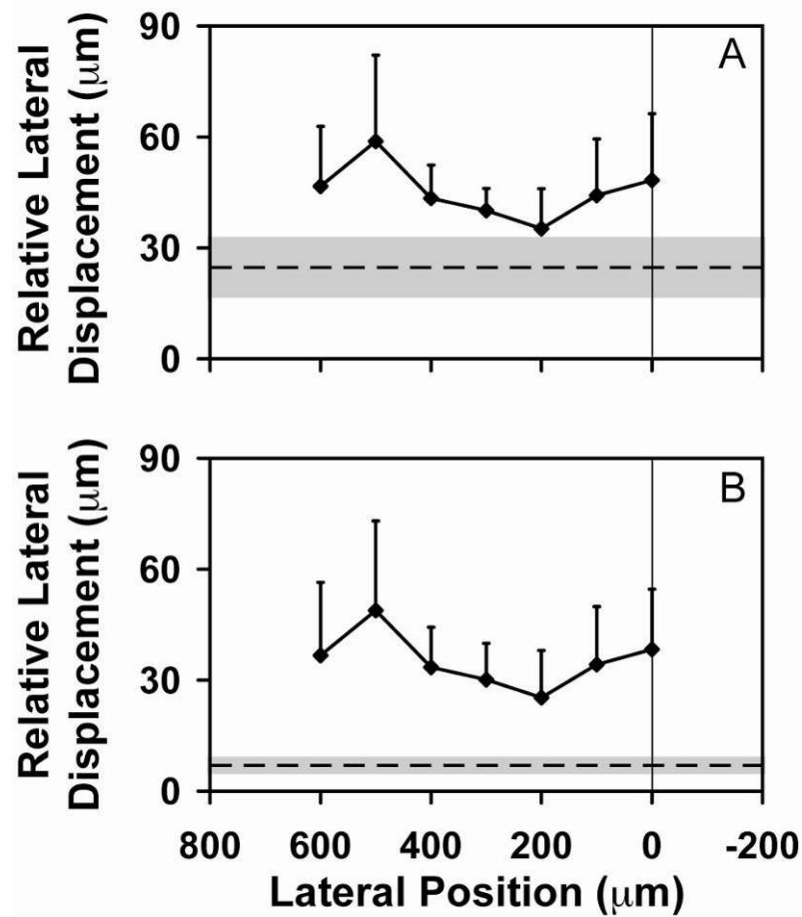


Figure A.8: Relative lateral displacement (RLD) between contacting human cartilage surfaces. Comparison of two methods to determine relative lateral displacements of surfaces adjacent (0-500 μm away) to defects (solid line) compared to the sliding between intact controls (dotted line with gray shading). Results are plotted using raw data (A) or data adjusted by accounting for the average RLD between intact controls (B). Mean \pm SEM. $n=4$.

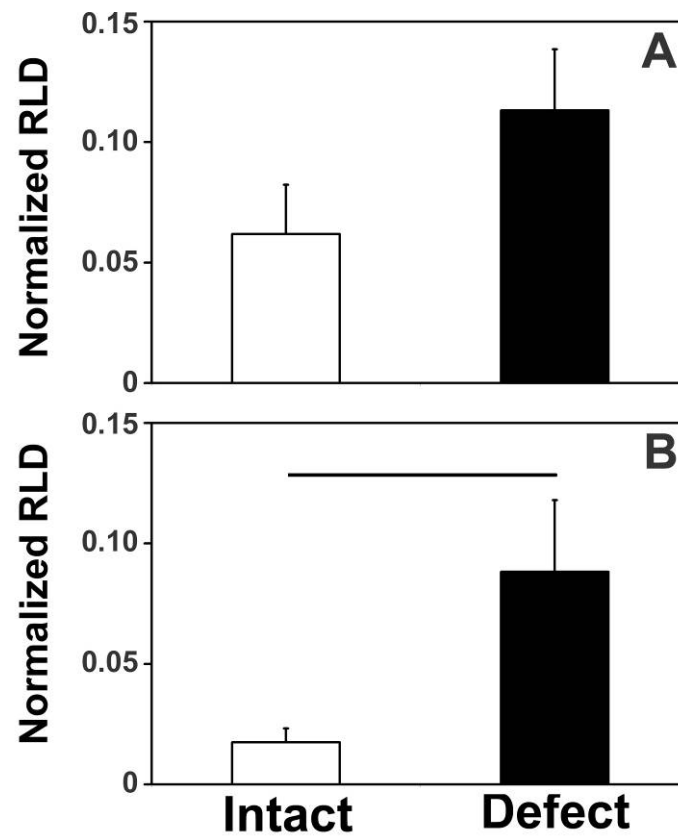


Figure A.9: Normalized Relative Lateral Displacements (RLD) between contacting human intact cartilage surfaces (white), or cartilage surfaces adjacent to focal defects (black). Results are plotted using raw data (A) or data adjusted by subtracting the average RLD between intact controls (B). Mean \pm SEM. n=4. Bar = p < 0.05.

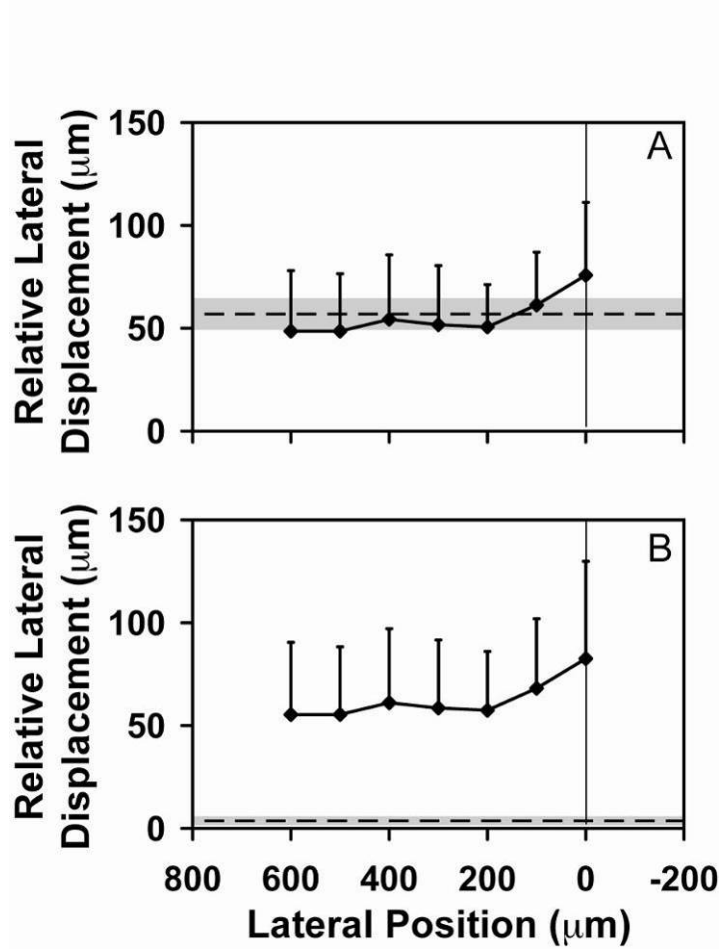


Figure A.10: Relative lateral displacement (RLD) between contacting bovine cartilage surfaces. Comparison of two methods to determine relative lateral displacements of surfaces adjacent (0-500 μm away) to defects (solid line) compared to the sliding between intact controls (dotted line with gray shading). Results are plotted using raw data (A) or data adjusted by accounting for the average RLD between intact controls (B). Mean \pm SEM. $n=4$.

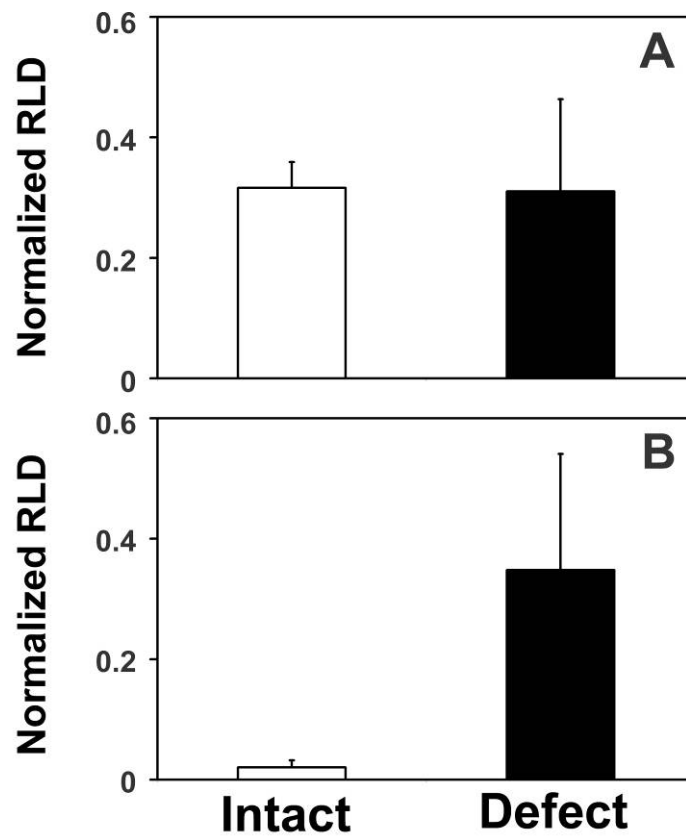


Figure A.11: Normalized Relative Lateral Displacements (RLD) between contacting bovine intact cartilage surfaces (white), or cartilage surfaces adjacent to focal defects (black). Results are plotted using raw data (A) or data adjusted by subtracting the average RLD between intact controls (B). Mean \pm SEM. n=4.

A.5 References

1. Kenny DA, Kashy DA, Bolger N: Data analysis in social psychology. In: *Handbook of social psychology*, ed. by D Gilbert, Fiske S, Lindzey G, McGraw-Hill, Boston, MA, 1998, 233-65.

APPENDIX B

SUPPLEMENTAL MATERIAL FOR CHAPTER 4

B.1 Introduction

Chapter 4 presents and discusses the major findings of this study. In certain cases, choices made in the data analysis may affect the interpretation of the data. This appendix provides greater detail on the reasons the choices were made and also presents results from alternative methods. Supplemental data not included in the chapter is also presented.

B.2 Materials and Methods

Adjustment of Relative Lateral Displacement Data with Intact Control Values

High inter-sample variability was observed in sliding calculations made on raw data. In chapter 2, it was noted that the defect orientation may have been having a significant effect, so that factor was studied explicitly in chapter 4. While attention to that property of defects resulted in more clear and consistent trends in sliding distances, substantial variability was still observed in the magnitudes of sliding. It is possible that properties of individual cartilage surfaces may be contributing to these differences.

Since non-negligible amounts of sliding were observed between opposing intact surfaces, sliding distances measured near defects may be considered as a combination of two separate components: 1) the intrinsic sliding between a particular pair of cartilage blocks and 2) the sliding due to the defect.

In intact cases, the direction of sliding varied depending on the characteristics of the two blocks. On the other hand, the contribution of a defect was always directed in the same direction, with the adjacent cartilage moving towards the defect with respect to the opposing surface. Thus, in cases where significant sliding occurs between two intact surfaces, sliding at a defect may be exaggerated when the two contributions are in the same direction, and reduced if the two contributions are in opposite directions. Two different methods were examined in order to better discern the effects of a focal defect (Figure B.1): 1) subtraction of the relative lateral

displacement (RLD) between the two surfaces in the intact configuration and 2) subtraction of RLD for a remote region away from the defect edge.

Method 1: Adjustment by Sliding between Intact Controls

Sliding distances at each analyzed time-point were first adjusted by subtracting the RLD measured between intact blocks at the same level of applied compression (equivalent to the approach described in Appendix A). Since the majority of sliding took place in the lateral direction (especially in the intact case), the RLD provided a good estimate of the tendency of the surfaces to slide preferentially in a given direction. Briefly, the RLD's over tracked portions of opposing intact surfaces were calculated from the displacements of points on each of the surfaces (as is described in detail in Chapter 2). For each surface, lateral (x- direction) displacement was fit to a linear function of x- position (Figure B.1). The average RLD for the intact surfaces was then determined as the difference between the lateral displacements calculated from the two equations at $x=0$ (the center of the block width). The average RLD for the intact blocks was then subtracted from the total sliding distances calculated for points along surfaces for both intact and defect samples. Details on the surface regions that were analyzed in each sample type and the calculation of 2-D sliding distances are included in Chapters 3 and 4.

Method 2: Adjustment by Sliding at a Remote Surface

Alternatively, sliding data was adjusted by subtracting the RLD of points along remote surfaces (1-2 mm away from the defect); the RLD in these regions were calculated in the fully-compressed state from images taken before loading and after stress relaxation. Briefly, lateral (x- direction) displacement of each surface was fit to a linear function of x- position (Figure B.1). The average RLD for the remote surfaces was then determined as the difference between the lateral displacements calculated from the two equations at $x=1.5$ mm away from the defect edge. This distance is greater than the thicknesses of the cartilage surfaces and but still stays away (~ 2 mm) from the outside edge of the sample. The remote RLD was then subtracted from the total sliding distances calculated for points along the surfaces adjacent to defects.

For intact samples, where no “remote” region exists, sliding distances were adjusted as described in method 1. The value of RLD at $x=0$ in the center of this region was calculated and subtracted from the measured total sliding distance.

Details on the surface regions that were analyzed in each sample type and the calculation of 2-D sliding distances are included in Chapters 3 and 4.

Data Analysis and Statistics

A full description of the statistics employed in this study is given in Chapter 4. Here, a brief explanation of key issues is presented.

Large differences between variances of samples were observed in both strain and RLD data. Generally, variances were proportional to the magnitudes of sample means. All statistics were performed on log-transformed data to minimize differences in variances. For planned comparisons, any remaining differences were accounted for by using t-tests for unequal variances.

For strain and area/volume change data, values from the both sides of each intact control were pooled to provide a single set of control values per sample pair ($n=4$ total control values). Initially, each control side had been treated as an independent sample, resulting $n = 8$ ($4 \text{ pairs} \times 2 \text{ blocks/pair}$) control measurements. However, contacting samples were found to not be independent, using a test of correlation between the two sides [1].

B.3 Results

A summary and discussion of the major results of this study are given in Chapter 4. A brief summary of how adjustment of the sliding data affected the results is given below. Additional strain and deformation data are also provided here in the form of figures.

Adjustment of Relative Lateral Displacement Data with Intact Control Values

Method 1: Adjustment by Sliding between Intact Controls

Sliding results were significantly altered when sliding distances were adjusted by subtracting average RLD of their corresponding controls at the same time-point (Figure B.3E-H, B.4C). As would be expected, the sliding distances over control surfaces were substantially reduced and the variability remained ~constant. Sliding over surfaces near defects with an open orientation remained relatively unchanged in both mean and variance. For surfaces adjacent to closed defects, there was relatively little change in the mean sliding distances, but substantially reduced variances, especially at higher levels of compression. Adjusted sliding distances at all times and surface points were significantly greater than controls. Normalized sliding distance (Figure B.3) was significantly affected by the sample type ($p < 0.05$) and the normalized sliding distance of closed defects was significantly higher than that of intact controls ($p < 0.02$).

Method 2: Adjustment by Sliding at a Remote Surface

Overall, the adjustment of sliding distances using the displacement values at the far-removed surfaces (method 2) tended to increase the variability between samples in all groups (Figure B.3-I, B.4-B). Values of relative displacement over the remote surfaces of “open” defects were ~equal to the values of relative displacements calculated for the corresponding control blocks. However, adjustment of the sliding distances for those samples did not markedly change either the average or standard deviations of those values. For “closed” defects, the values of relative displacement in the far-removed regions were still higher than those of the corresponding intact controls. When sliding displacements measured near “closed” defects were adjusted by the remote values of relative displacement, the variability was ~unchanged and the sliding distances were markedly reduced. Statistical analyses of the sliding distances adjusted using method 2 showed no significant differences between points adjacent to either defect type and controls ($p > 0.15$).

B.6 Acknowledgments

The dissertation author is the primary investigator and thanks co-authors Ben Wong and Drs. Won Bae and Robert Sah. This work was supported in part by the National Institutes of Health and the National Science Foundation, and by a grant to the University of California, San Diego, in support of Dr. Robert Sah, from the Howard Hughes Medical Institute through the Professors Program.

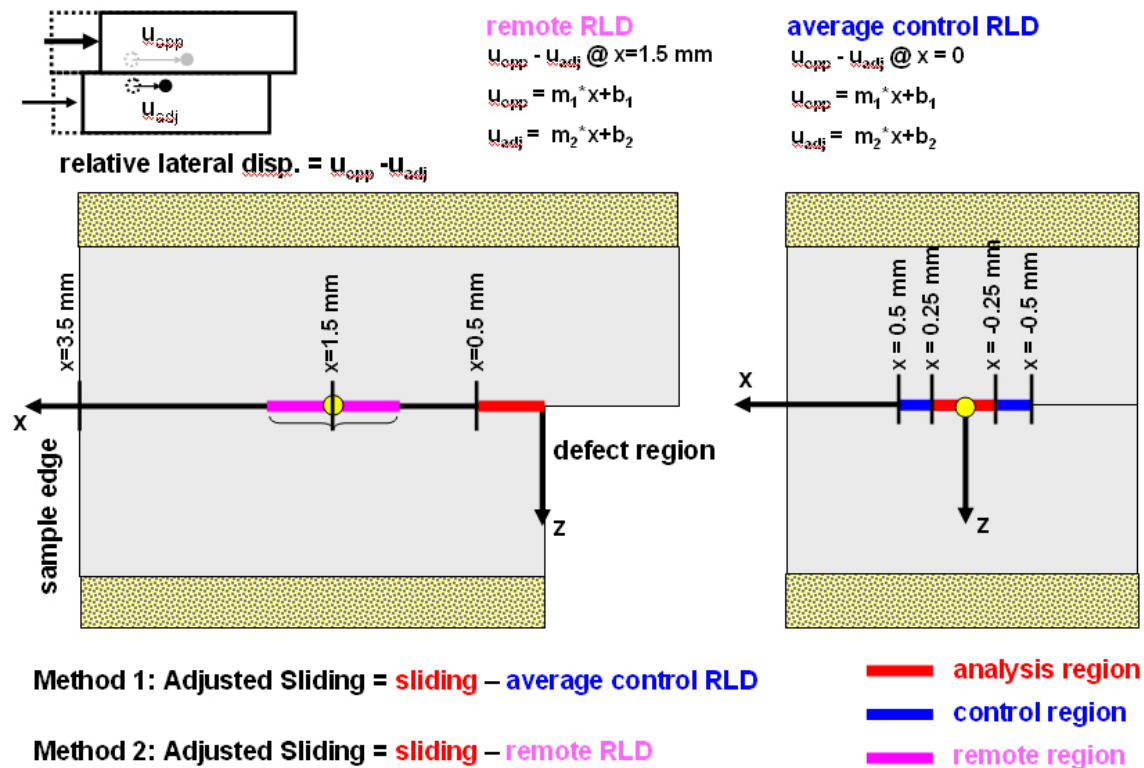


Figure B.1: Schematic of the sliding calculations. Since the majority of sliding in the experimental configuration takes place in the lateral (x-) direction, sliding may be roughly estimated as the relative lateral displacement (RLD) of neighboring points on the opposing surfaces. Contributions of defects to sliding may be isolated by subtracting the intrinsic sliding behavior of a particular pair of blocks from the total measured sliding distance. Two methods were examined: 1) subtracting the RLD measured at a region remote from the defect or 2) subtracting the RLD between the same pair of blocks in the intact configuration.

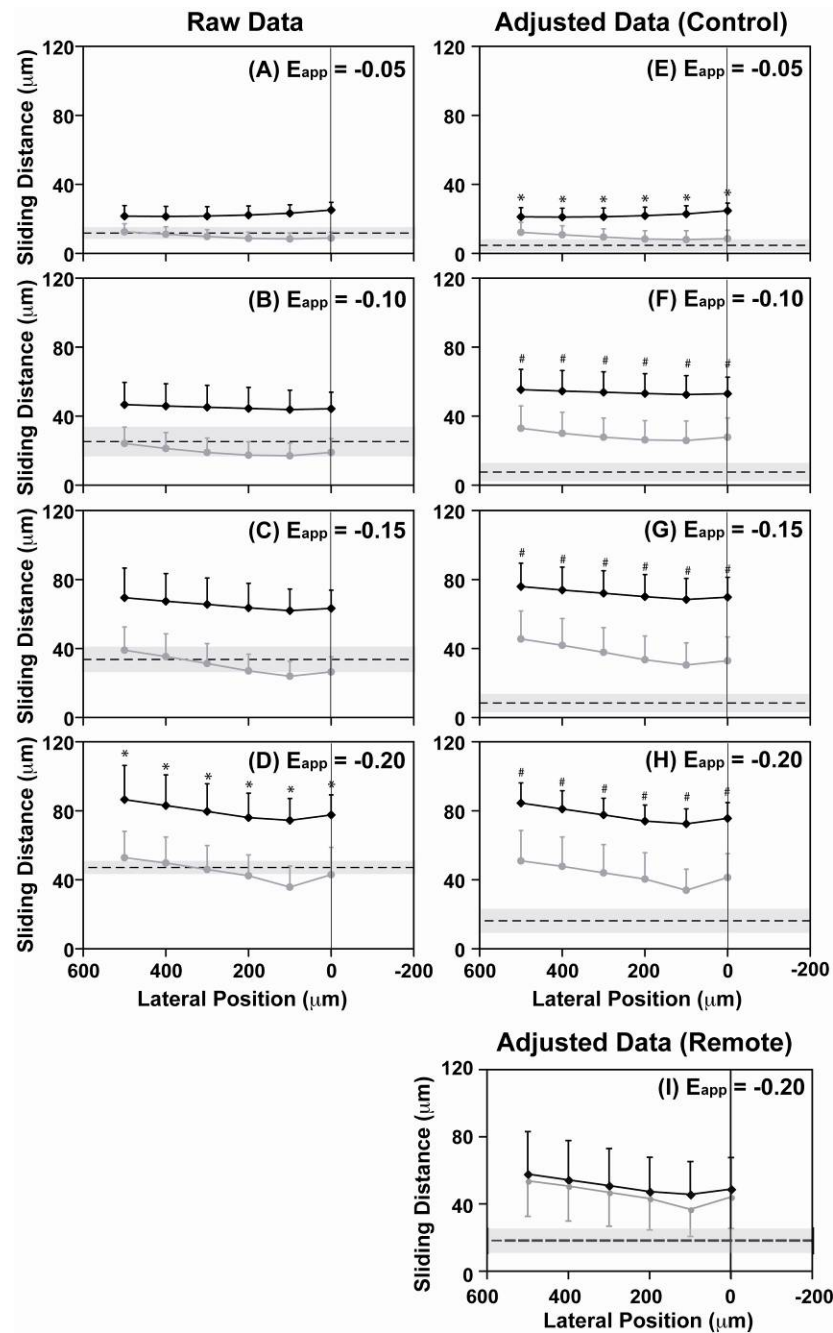


Figure B.2: Figure 3. Sliding distances of surfaces adjacent to defects with open (solid gray line) or closed (solid black line) orientations compared to the sliding between intact controls (dotted line with gray shading). Results are plotted using raw data (A-D) or data adjusted by method 1 (I) or 2 (E-H). (* $p < 0.05$; # $p < 0.01$). Data are expressed as mean \pm SEM. $n=4$.

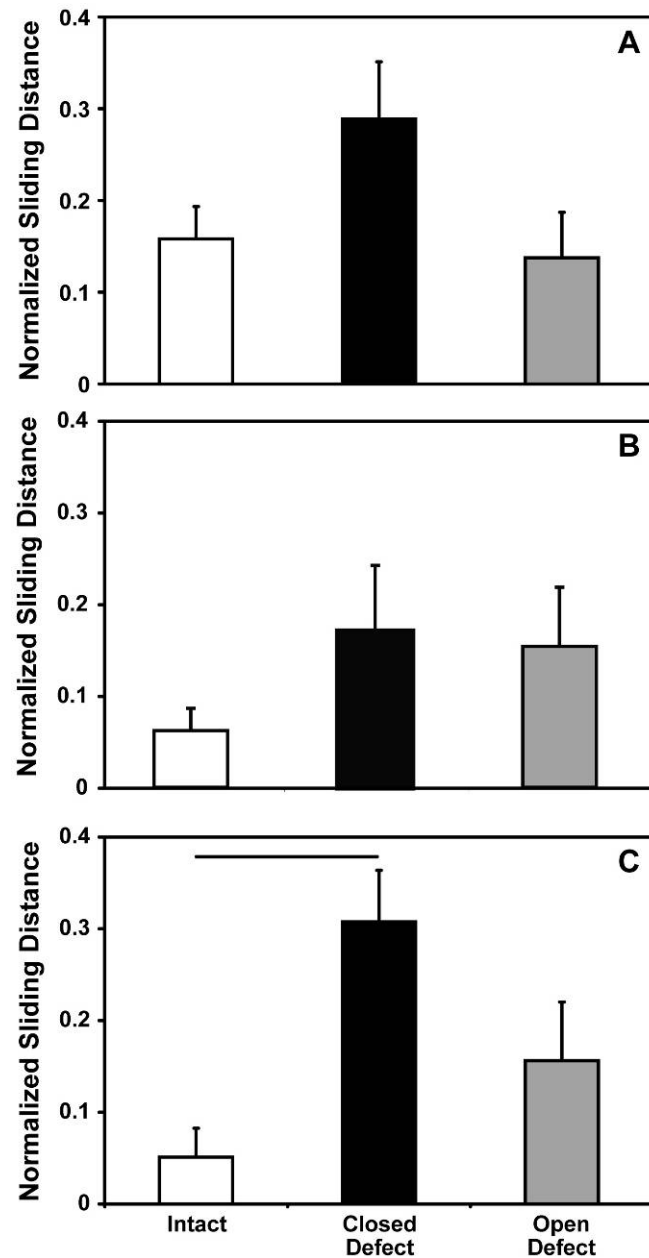


Figure B.3: Normalized sliding distance between contacting intact cartilage surfaces (white), or cartilage surfaces adjacent to focal defects with “closed” (black) or “open” (gray) edge orientations. Results are plotted using raw data (A) or data adjusted by (B) subtracting the relative lateral displacement (RLD) measured at a region away from the defect edge, or (C) subtracting the RLD measured between the same pair of blocks in the intact configuration. (Bar = $p < 0.05$) Data are expressed as mean \pm SEM. $n=4$.

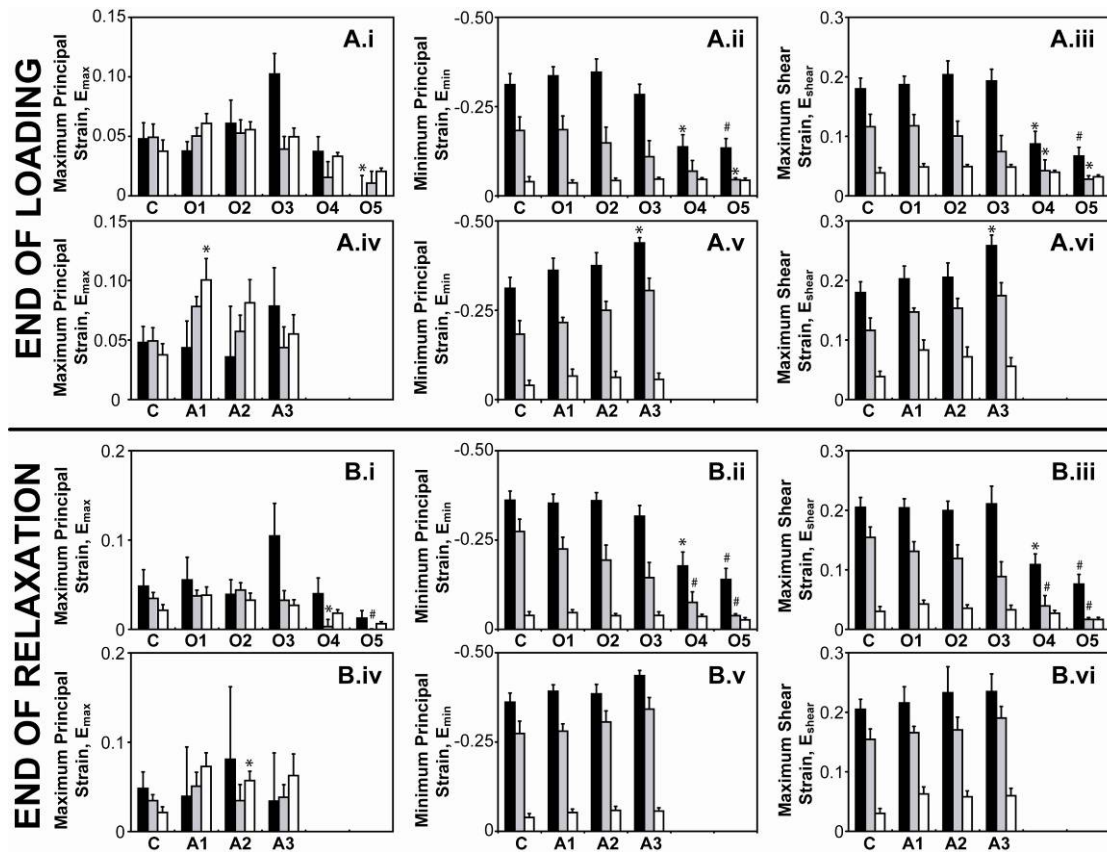


Figure B.6: Principal strain measurements at selected sub-regions in bovine (A.i-A.vi) and human samples (B.i-B.vi). Strains were calculated in $100 \times 100 \mu\text{m}$ sub-regions at S (■), M (■), and D (□) depths for several lateral positions along the cartilage surfaces adjacent (A1-A3) and opposing (O1-O5) a focal defect. Strain in each sub-region was compared to the value from intact control samples (C) at the corresponding depth (* $p < 0.05$; # $p < 0.01$; † $p < 0.001$). Data are expressed as mean \pm SEM. $n=4$.

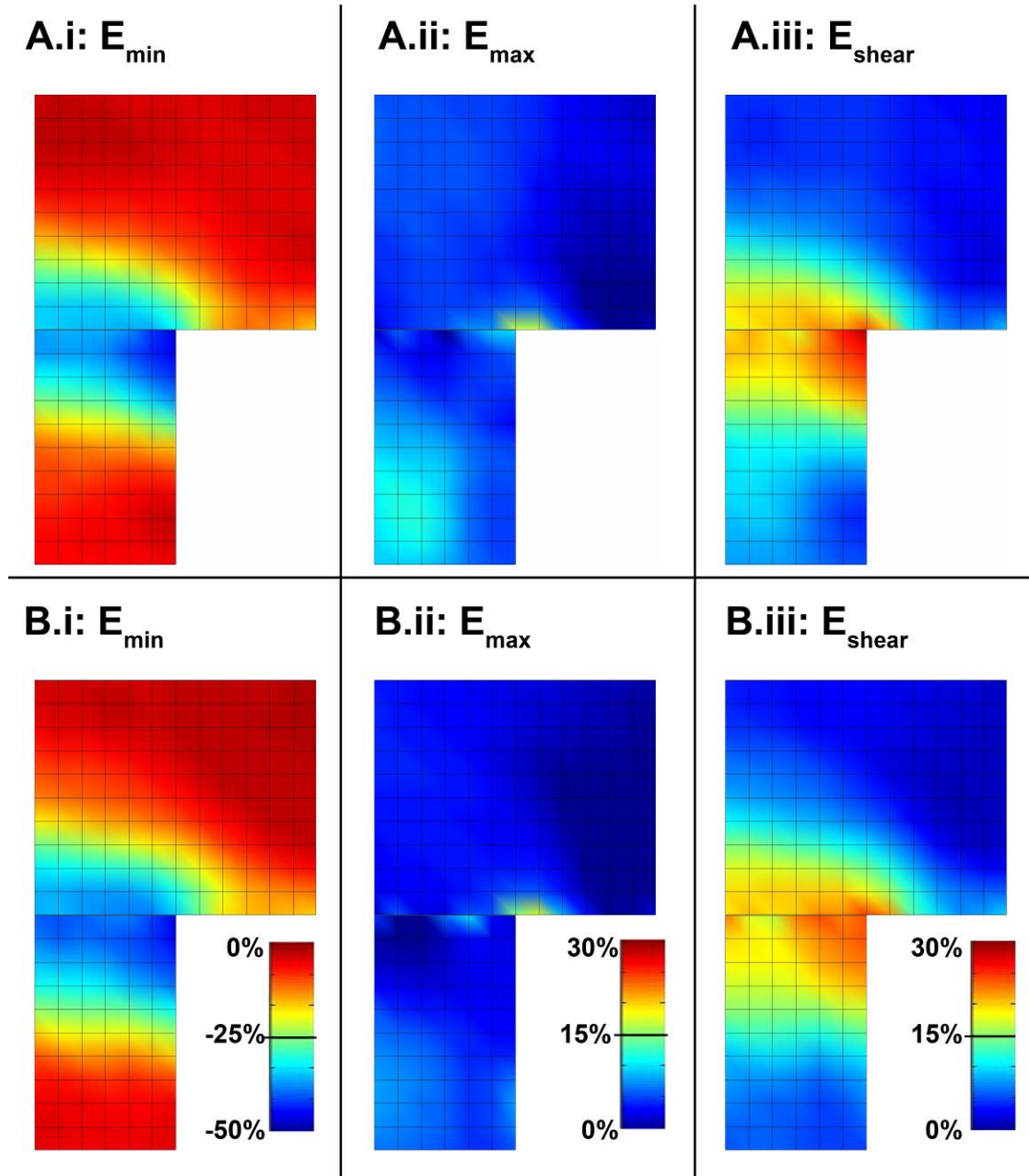


Figure B.7: Composite strain maps in bovine samples (A) directly following loading or (B) after stress relaxation, for regions $\pm 600 \mu\text{m}$ laterally from the defect and 1 mm depth. Boxes = $100 \times 100 \mu\text{m}^2$.

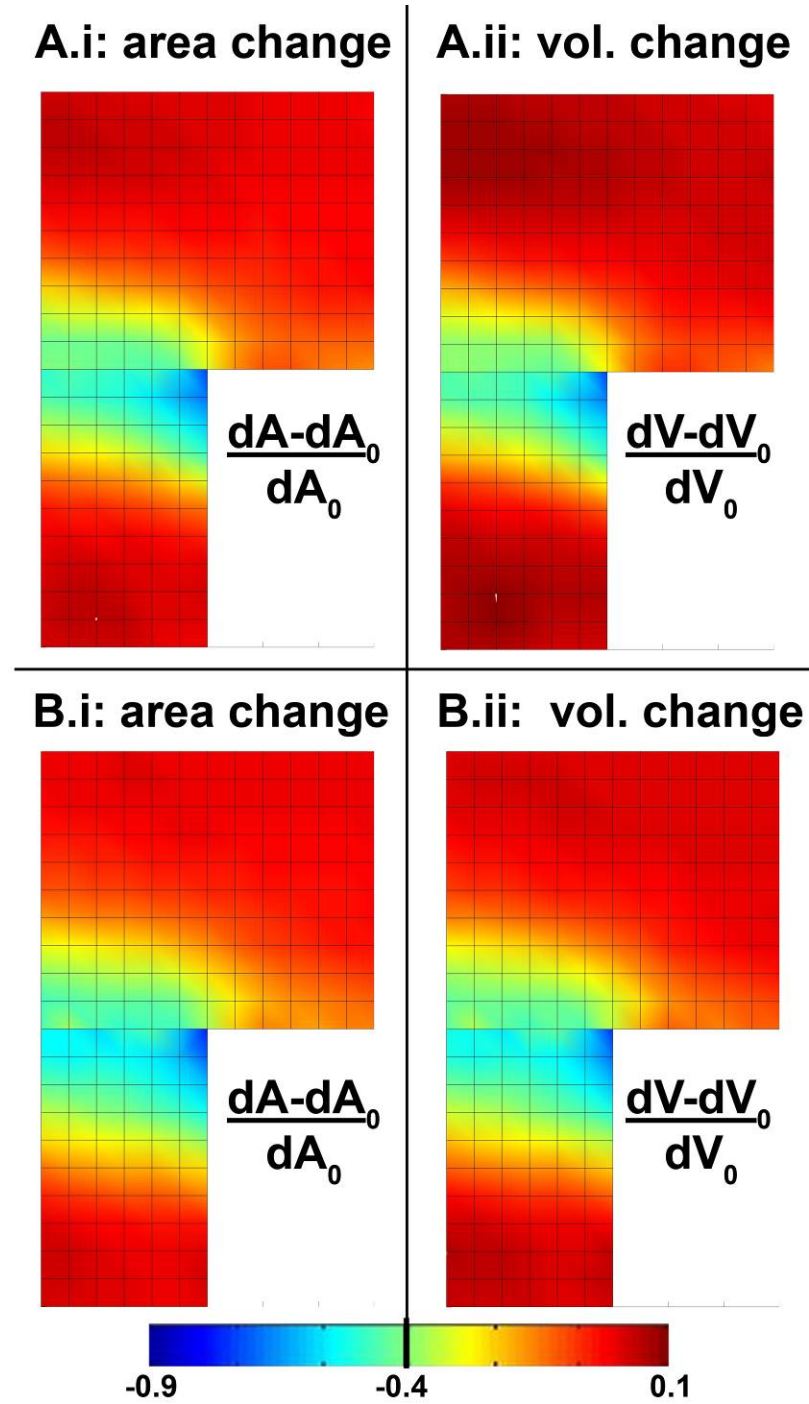


Figure B.8: Composite maps of area and volume changes in bovine samples (A) directly following loading or (B) after stress relaxation, for regions $\pm 600 \mu\text{m}$ laterally from the defect and 1 mm depth. Boxes = $100 \times 100 \mu\text{m}^2$.

B.7 References

1. Kenny DA, Kashy DA, Bolger N: Data analysis in social psychology. In: *Handbook of social psychology*, ed. by D Gilbert, Fiske S, Lindzey G, McGraw-Hill, Boston, MA, 1998, 233-65.